ATOMIC LEVEL COMPUTATIONAL STUDIES OF IONIC DEFECTS AND TRANSPORT PROPERTIES OF SOLID STATE IONIC CONDUCTORS

A Dissertation
Presented to
The Academic Faculty

by

Lei Zhang

In Partial Fulfillment
of the Requirements for the Degree
Doctor of Philosophy in the
School of Materials Science and Engineering

Georgia Institute of Technology
May 2020

ATOMIC LEVEL COMPUTATIONAL STUDIES OF IONIC DEFECTS AND TRANSPORT PROPERTIES OF SOLID STATE IONIC CONDUCTORS

Approved by:

Dr. Meilin Liu, Advisor
School of Materials Science and Engineering
Georgia Institute of Technology

Dr. Ting Zhu, Co-advisor
School of Materials Science and Engineering, School of Mechanical Engineering
Georgia Institute of Technology

Dr. Jean-Luc Brédas, Co-advisor
School of Chemistry and Biochemistry
Georgia Institute of Technology

Dr. Rampi Ramprasad
School of Materials Science and Engineering
Georgia Institute of Technology

Dr. Angus Wilkinson
School of Materials Science and Engineering, School of Chemistry and Biochemistry
Georgia Institute of Technology

Date Approved: [Jan 10, 2020]

To my parents

ACKNOWLEDGEMENTS

I would like to thank Prof. Meilin Liu for being a great Ph.D. advisor. Without his full support, I wouldn't be able to continue my passion for density functional theory calculations, as well as picking up other types of computational methods. His appreciation of my computational/theoretical talent and trust in my capability greatly encourages me to explore the fundamental scientific problems in solid state ionics and surface catalysts. His vision in this field, as well as engineering way of solving problems, teach me how to approach problems pragmatically, and connect fundamental science to real impact.

I would like to thank my committee members for all the helpful comments and suggestions during the thesis preparation.

I would like to thank all Liu group members for their kind support and help in my study and life in Georgia Tech and Atlanta. It is a milestone when I came to Atlanta from State College after finishing my Master's degree. Without their help, I could not easily adapt to a new environment and get on track in Liu group. Specifically, those who collaborate with me on projects and papers, e.g., Dr. Yong Qin, Dr. Bote Zhao, Dr. Yu Chen, Dr. Yan Chen, Dr. Chong Qu, Dr. Xuejiao Li, Dr. Zhongkang Han, Dr. Wenwu Li, Dr. Qiaobao Zhang, Dr. Jianhuang Zeng, Dr. Dai Dang, Dr. Tao Wei, Dr. Haibin Sun. Without your collaboration, I could not be as productive and successful as I am now.

Thanks to a lot of computational colleagues who guided me patiently, Prof. Veronica Ganduglia-Pirovano from Spain, Prof. Yi Gao from Shanghai, Prof. Angelo Bongiorno, Ting Zhu and Jean-Luc Bredas at Georgia Tech, Dr. Panchapakesan Ganesh at ORNL, Prof. Yongman Choi from Taiwan, Dr. Lixin Sun from MIT.

Thank Dr. Xiaxi Li, Dr. Dongchang Chen, Dr. Ikwhang Chang, Dr. Seonyong Yoo, Dr. Kai Pei, Dr. Brain Doyle, Dr. Ben Rainwater for being great friends.

Thank colleagues from Penn State, Prof. Zi-Kui Liu, Prof. Bi-Cheng Zhou, Dr. Zijian Hong, Dr. Pinwen Guan for their kind discussion and support.

Lastly, I would like to show my deep gratitude to my parents. Without their supportive manner and attitude, I could not pursue my Ph.D. degree in the US.

TABLE OF CONTENTS

LIST OF TABLES

LIST OF FIGURES

LIST OF SYMBOLS AND ABBREVIATIONS

DFT	Density Functional Theory
SOFCs	Solid Oxide Fuel Cells
SSIs	Solid State Ionics
OCE	Oxygen ion-Conducting Electrolyte
PCE	Proton-Conducting Electrolyte
MD	Molecular Dynamics
MC	Monte Carlo
BHO/BZO/BCO	$BaHfO_3$/ $BaZrO_3$/ $BaCeO_3$
BHCO/BZCO	$Ba(Hf,Ce)O_3$/ $Ba(Zr,Ce)O_3$
CE	Chemical Expansion
IS	Initial State
TS	Transition State
ZPE	Zero-Point Energy
MIEC	Mixed Ionic Electronic Conductor
STM	Scanning Tunneling Microscopy

SUMMARY

Solid state ionic conductors (or electrolytes) are a vital component for electrochemical devices or systems for chemical and energy transformation. The chemical composition, crystal structure, defects, morphology, and electronic structure of these materials greatly affect their electrochemical properties such as ionic and electronic conductivity.

Similar to barium zirconate ($BaZrO_3$), barium hafnate ($BaHfO_3$) is one of the most promising proton-conducting electrolytes for solid oxide fuel cells (SOFCs) because of their high proton conductivity at 400~700 °C. In this study, I have investigated dopant solubility, proton concentration, mobility, and chemical stability of A/B-site co-doped $BaHfO_3$ using density functional theory calculations coupled with statistical thermodynamics. Specifically, I have calculated defect formation energy in charged supercells, finite temperature vibrational energy *via* phonon calculations in the harmonic approximation, proton migration energy *via* transition state theory, and defect-defect interactions *via* cluster-expansion method. A wide range of relevant properties are predicted, including the degree of hydration governed by hydration Gibbs free energy, proton diffusion coefficient derived from proton migration barrier search, and defect-defect interactions using cluster expansion method. These properties are sensitive to the type and amount of chemical dopants in the lattice, including Li, Na, K, Rb, and Cs on A-site and Sc, Y, La, Gd, Lu, Al, Ga, and In on B-site. The mismatch in the size of the dopant and the host ion induces local strain or elastic interactions. However, the electrostatic interactions between them are much less dependent on the ionic radius of dopant ions. Accordingly, the

dependence of the dopant-proton binding energy on ionic radius of dopant has a “volcano” shape. In addition, the electronegativity of dopant ions also affect the affinity of acceptor-type dopants with donor-type protons. Hydration is promoted by both the A-site and the B-site dopants, although the effect of the latter is less pronounced. In general, a “trade-off” relation between proton concentration and mobility is observed in all cases, regardless of the ionic radius or the lattice site (A- or B-site) of the dopants.

Defects play an important role in ionic transport and in enhancing catalytic activities for chemical and energy transformation processes. Thus, it is crucial to understand how to effectively enhance ionic transport by rationally design preferred defect structures, including 0D (point defects such as vacancies), 1D (dislocation), and 2D (grain boundary) defects. For example, local ion segregation may result in a space charge region, leading to accumulation of mobile charge carriers or improved mobility near those 1D/2D defects. The effect of the space charge layer, strain near 1D/2D defects, as well as collective defect-defect interactions pose an extreme challenge for both experiments and computations. In this study, the effect of an edge dislocation in Y:$BaZrO_3$ on oxygen ion transport is evaluated. To probe the ion mobility, a reactive molecular dynamics simulation based on ReaxFF is utilized to simulate the super-large Y:$BaZrO_3$ supercell with two edge dislocations. Radial distribution functions and thermal/chemical expansion coefficients are used to benchmark the local and global structure properties, and mean-square displacements are used to calculate diffusivity and conductivity. Dislocation is found to lower the activation energy of ionic transport, possibly because of distinct oxygen cage structures locally at the dislocation core. However, optimal Y% for oxygen ion

conductivity is shifted to higher levels with increasing temperature. This could be due to the weakening of Y's electrostatic "trapping effect".

Besides materials chemistry and microstructural features, the mechanical strain is another factor affecting ionic properties. Ceria (or CeO_2) is a prototypical ionic material for catalyst and electrolyte applications. Chemo-mechanical coupling in ceria significantly affect the bulk defect properties of ceria. In this study, the effect of chemo-mechanical coupling is extended from the bulk to the (111) surface of ceria. There have been extensive theoretical and experimental research on the configurations of vacancies and polarons on the (111) surface, the dominantly exposed surface, which is crucial to surface catalytic activity. It was reported that surface oxygen vacancy on ceria's (111) surface is not necessarily the most stable vacancy; however, the sub-surface vacancy could be. Similarly, polarons are not necessarily at the 1_{st}-nearest-neighbor (1NN) of the corresponding vacancy either; they could be at the 2_{nd}-nearest-neighbor (2NN). All those counter-intuitive phenomena were unveiled and validated both theoretically and experimentally. Inspired by previous research, I have identified a unique way of tuning defect configurations by applying tensile and compressive epitaxial strain on (111) slab. Across the magnitude of the applied strain from -5% compression to +5% tension, stability relationships of the surface vs. the sub-surface vacancy, the 1NN vs. the 2NN polaron, and the vacancy monomer vs. the dimer are surprisingly reversed. Elastic, electrostatic and electronic excitation energies are found to be dependent on defect-configuration. This gives us a new perspective to interpret the various vacancy patterns observed on (111) surface of the prepared ceria samples.

CHAPTER 1 INTRODUCTION

1.1 Motivation

To mitigate the environmental impact of fossil fuels and enable sustainable and cost-effective energy consumption, electrochemical devices that can directly convert the chemical energy to electricity are in urgent need. Among all types of energy conversion devices, solid oxide fuel cells (SOFCs) are great prospects for efficient utilization of hydrogen, hydro-carbon fuels, and biomass. SOFCs demonstrate great advantages over conventional combustion engines, because of their well-controlled electrochemical reactions between fuels and oxygen gas. The theoretical efficiency of energy conversion in SOFCs greatly surpasses the limit of the Carnot cycle.

Among the components of the cathode, the anode and the electrolyte, the electrolyte layer contributes the majority of the Ohmic resistance, impeding the progress of lowering the working temperature and maintaining a sufficient power density[1]. Proton-conducting oxides, as the electrolytes of SOFCs, are a good alternative to oxygen ion-conducting oxides (e.g., Y-Stabilized-ZrO_2, Gd-Doped-CeO_2, and $(La,Sr)(Ga,Mg)O_3$). Due to the intrinsically higher mobility of protons compared with oxygen ions in the electrolytes, proton-conducting oxides can potentially improve SOFCs' power density at relatively lower working temperatures (i.e., 500 °C)[2]. This helps the commercialization of economically viable and sustainable SOFCs. SOFCs with proton-conducting electrolytes are also called protonic ceramic fuel cells (PCFCs)[3].

PCFCs have the potential to be the cleanest and most efficient systems for direct conversion of petroleum or other fossil fuels to electricity at ~500 °C[2]. The intermediate operation temperature greatly reduces the cost of the system because much less expensive materials can be used as system components. The power density and durability of the device is closely related with the proton conductivity in the electrolyte and the contaminant tolerance of the material. Yang et al.[4] demonstrated that $BaZr_{0.1}Ce_{0.7}Y_{0.2-x}Yb_xO_{3-\delta}$ (or BZCYYb1711) has high proton conductivity and excellent tolerance to sulfur and coking. Later, Duan et al.[2] fabricated highly durable PCFCs with excellent coking and sulfur tolerance by using $BaZr_{0.8}Y_{0.2}O_{3-\delta}$ (or BZY20), $BaCe_{0.6}Zr_{0.3}Y_{0.1}O_{3-\delta}$ (or BCZY63), and $BaCe_{0.7}Zr_{0.1}Y_{0.1}Yb_{0.1}O_{3-\delta}$ (or BCZYYb7111) as electrolytes. Very recently, Duan et al.[3] fabricated other PCFCs with BZY20 and BCZYYb7111 as electrolytes and demonstrated excellent hydrocarbon fuel flexibility and contaminant tolerance. Choi et al.[5] adopted a slightly different composition $BaCe_{0.4}Zr_{0.4}Y_{0.1}Yb_{0.1}O_{3-\delta}$ (BZCYYb4411) and presented exceptional power density and stability at 500 °C.

To date, however, the development of electrolyte materials for PCFCs has been largely based on trial and error, such as adjusting the type or amount of dopants in the synthesized sample one at a time and then measuring the electrochemical property repetitively until the optimal composition is found. This approach is not only tedious but also inaccurate because sample fabrication and testing could potentially lead to significant uncertainties due to experimental limitations, including composition deficiency from Ba evaporation during sintering[6], variation in density or porosity among different dopants[7], occurrence of secondary phases[8], and inconsistency in microstructures (e.g.,

grain size, pore size, and their distributions)[9]. Therefore, the experimental success of materials optimization has been limited.

$BaHfO_3$ is a proton-conducting oxide that has not been studied much, but has been recently recommended as a good alternative to $BaZrO_3$[10]. Similar material systems, including $BaZrO_3$[11-42], $BaSnO_3$[43-49], and $BaCeO_3$[50-52], have been intensively studied both experimentally and computationally. Specifically, in the area of computation, a variety of relevant properties were computed using atomic-level simulation techniques such as *ab-initio* density function theory (DFT), molecular dynamics (MD) and kinetic Monte-Carlo (kMC), etc. The properties include hydration degree, proton conductivity, and stability. A variety of dopant candidates have been recently tested in this family of materials, including trivalent rare-earth and metalloid elements on the B-site, and, very recently, alkali elements on the A-site. Preliminary efforts have been made to select "optimal" dopants for proton conductivity. Furthermore, complex defect-defect interactions were also taken into account by "quasi-random" supercells. Molecular dynamics simulations also provided a much more convenient way to sample a statistical average of proton diffusivity in the supercells with a complex chemistry.

Besides materials chemistry in single-crystalline perovskite, grain boundaries also have dramatic effects on ionic transport in this type of material. Yamazaki et al.[9] found that large-grain samples of $BaZr_{0.8}Y_{0.2}O_{3-\delta}$ (BZY20) demonstrate lower grain boundary resistance by two to three orders of magnitude. This evidence shows that grain boundaries have a detrimental effect on proton conduction. Corresponding theoretical work[53] suggested that oxygen vacancies segregate near grain boundaries and form the positively-

charged space charge layer might be the reasons. Since the proton is also positively charged, grain boundaries act as charge-blocking layers for inter-granular proton transport. Recent theoretical work of the dislocation effects on the oxygen ion transport near edge dislocations in $SrTiO_3$ and doped-CeO_2[54, 55] demonstrated a similar physical picture. Unlike fast 'pipe-diffusion' of hydrogens in metals, dislocations in solid-state ionic materials have negative effects on oxygen ion transport. This is mainly because the co-segregated dopants and oxygen vacancies have electrostatic "anchoring" effects on each other.

Inspired by the previous work, we designed a similar supercell set-up in Y-doped $BaZrO_3$ to that in [54], by having two edge dislocations with opposite Burgers vectors embedded in it. We zoomed into the dislocation core area and studied the oxygen vacancy transport near the dislocation line. Comparison with the "bulk-like" region was made[56]. Because of the large size of the supercell, only classical/semi-classical force-field molecular dynamics are feasible. Among those, ReaxFF developed by Adri Van Duin[57] is the best choice for this type of system. Further study on analysis of proton transport and dopant swapping/segregation are recommended.

Besides perovskite-based proton conductors, fluorite-based CeO_2 is another prototypical material used in SOFCs. When it is doped with trivalent dopants, e.g., the rare-earth elements Y, Gd, and Sm, extrinsic oxygen vacancies are automatically generated in the fluorite lattice. It can then serve as an oxygen ion-conducting electrolyte in SOFCs with ionic conductivity superior to that of the previous generation ZrO_2-based ones, e.g., Yttrium-doped (YSZ) or Scandium-doped (ScSZ) conductors. When it is exposed to a

reducing atmosphere, it also easily generates intrinsic oxygen vacancies, with electrons from oxygen ions' *2p* orbitals donated back in the lattice. In this scenario, the function of ceria is very similar to that of a typical Mixed Ionic Electronic Conductor (MIEC), e.g., (La,Sr)(Co,Fe)O_3 and (La,Sr)MnO_3. One intrinsic oxygen vacancy typically creates two electron-polarons residing on nearby Ce ions' *4f* orbitals. However, those two polarons don't have to be at the 1st-nearest-neighbor (1NN) of the corresponding vacancy. It can be sensitive to pressure acted on the bulk lattice[58], or epitaxial strain applied on the surface[59]. Following previous DFT calculations[60] and STM images[61] on ceria's (111) surface, the effect of strain on the surface vacancy and polaron configurations is studied.

1.2 Research objectives

The research objectives are divided into two categories: engineering and scientific. Since ionic defects in solid-state ionic materials play a key role in determining the performance of energy conversion devices, it is technologically attractive to design new materials with higher bulk ionic conductivities and surface exchange rates. From the engineering perspective, therefore, rational designs of materials chemistry, microstructure, and external strain are proposed for the next generation of SOFCs and fuel cell catalysts. To achieve the engineering objectives, new scientific knowledge is required. Therefore, we need to use computations to build up the understanding of ionic defects' electronic, atomic, thermodynamic, and kinetic properties through computations. The new knowledge regarding ionic defects and its correlation with macroscopic materials properties and device

performance pushes forward the scientific understanding in this field and serves as a basis for future endeavors by other researchers.

1.2.1 Engineering objectives

1. Deliver a realistic dopant-selection "recipe" by evaluating dopant solubility, proton concentration and mobility, and chemical stability in A/B-site doped $BaHfO_3$. The "recipe" should consider the cost and fabrication feasibility of materials. The computationally designed materials chemistry can be directly tested experimentally.
2. Suggest rational design of the 1D defect, i.e. edge dislocation, to promote ionic conductivity in Y:$BaZrO_3$. Combine microstructure design with materials chemistry optimization to further enhance the ionic conductivity.
3. Recommend appropriate magnitude and direction of the mechanical strain to achieve expected vacancy-polaron patterns on the surface (111) of ceria so that corresponding catalytic activity is controlled. Interface engineering and/or nano-scale morphology could introduce the strain to ceria's surfaces.

1.2.2 Scientific objectives

1. Use ionic radius and electronegativity as descriptors to understand elastic and electrostatic interactions. Evaluate enthalpy and entropy's contributions to defect thermodynamics. Quantify ionic defect thermodynamic stability, kinetic mobility, and chemical stability.

2. Elucidate the advantages of edge dislocation for ionic defect's concentration and mobility. Correlate local structures of edge dislocation with the enhanced ionic transport.
3. Explore the role of strain in ionic defect configurations. Distinguish elastic, electrostatic, and electronic contributions to vacancy formation energy.

1.3 Dissertation structure

CHAPTER 2 lays out an overview of SOFCs and relevant material systems, emphasizing key fundamental quantities and scientific issues to be calculated and solved computationally, including defect thermodynamics, kinetics, and electronic structures.

CHAPTER 3 introduces atomic-level computational methods used to perform the work described in this dissertation, from the electronic structure method to statistical dynamics.

CHAPTER 4 discusses the computationally-designed dopants in the $BaHfO_3$ system for high-temperature proton-conducting electrolytes. From 0K electronic enthalpy to vibrational free energy evaluation, dopant dissolution energy, material hydration energy, dopant-proton binding energy, and chemical reaction energy were computed, so that a rational selection of the optimal dopants among 13 dopant candidates was realized.

CHAPTER 5 discusses the properties of ion transport near edge dislocation in $Y:BaZrO_3$. A reactive molecular dynamics method was introduced to study lattice oxygen transport properties. The trapping effect with the existence of dislocation was discussed. The local structure of the dislocation core was analyzed during the oxygen ion migration.

CHAPTER 6 discusses strain-modulated near-surface defect stabilities on ceria (111). The stability of various vacancy and polaron spatial configurations were controlled by elastic, electrostatic, and electronic factors that are all strain-dependent.

CHAPTER 7 summarizes the significance and impact of the computational result, points out future directions, and lists major assumptions and approximations of the methodology.

CHAPTER 2 BACKGROUND

2.1 Solid oxide fuel cells

Solid oxide fuel cells (SOFCs) are made of three components: the cathode, the anode, and the electrolyte. Instead of homogeneous combustions, reactions of fuels and air are indirectly taken place on the anode and cathode surfaces. Gas molecules are ionized under electrocatalytic processes, with oxygen ions or protons going through a selective membrane (a solid state electrolyte), and deprived electrons flowing through the external circuit. A schematic of electrochemical reactions occurring in SOFCs is shown in Figure 1. There are two types of SOFCs: the one with the oxygen ion-conducting electrolyte is called Oxygen ion-conducting SOFCs, (or O-SOFCs); the one with the proton-conducting electrolyte is called Proton-conducting SOFCs, (or H-SOFCs). H-SOFCs is also called Protonic Ceramic Fuel Cells (PCFCs). Using H_2 as the fuel, the reaction equations are shown below:

$\boldsymbol{H_2 \rightarrow 2H^+ + 2e^-}$ or hydrogen oxidation reaction (HOR), on the anode surface

$\boldsymbol{\frac{1}{2}O_2 + 2e^- \rightarrow O^{2-}}$ or oxygen reduction reaction (ORR), on the cathode surface

$\boldsymbol{2H^+ + O^{2-} \rightarrow H_2O}$ on the cathode side for SOFCs, on the anode side for PCFCs

To ensure high-enough power density, facile HOR and ORR reactions on electrode surfaces, as well as fast oxygen ion or proton transport within the bulk of electrolytes are required. Among those components, the solid electrolyte is the central part governing the ionic transport characteristics of SOFCs. By replacing the oxygen ion-conducting

electrolyte (OCE) with the proton-conducting electrolyte (PCE), sluggish oxygen ions are replaced by fast protons. Therefore, the Ohmic resistance of electrolyte can be greatly diminished. Additionally, the fuel dilution problem is avoided in PCFCs by having the combustion exhaust on the cathode side.

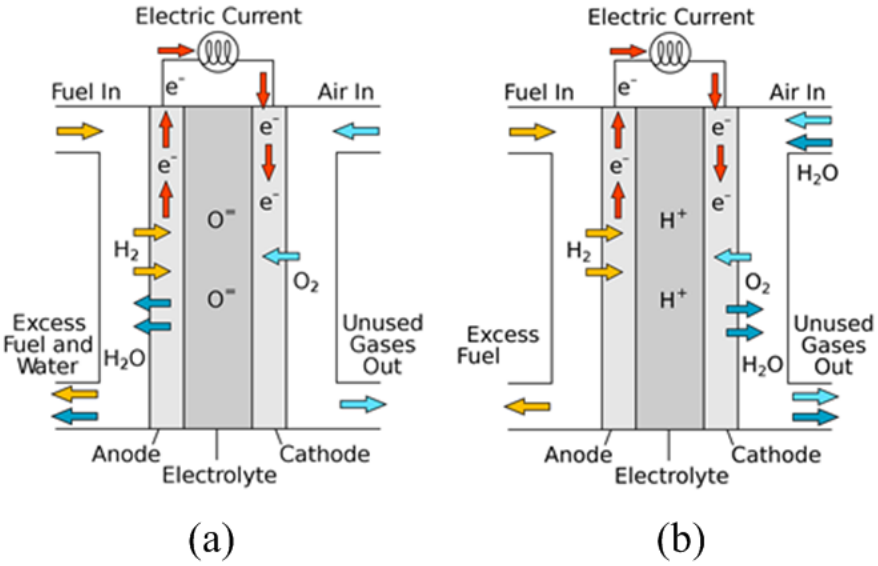

Figure 1 Two types of SOFCs working schematics attributed to two types of ionic conducting electrolytes: (a) oxygen ion-conducting electrolyte, (b) proton-conducting electrolyte.

The materials used in SOFCs are mainly ceramics, or materials in solid state ionics (SSIs). Ionic defects in SSIs play a key role in surface catalytic activity and bulk conductivity. To make this device commercially viable, a few technical challenges need to be overcome: the working temperature needs to be brought down, the cost of raw materials (e.g. rare-earth elements) and fabrication processes need to be reduced. In terms of materials innovation, novel SSIs with higher surface exchange rates and bulk conductivities are needed. Below I will cover the basic properties and phenomena relevant

to proton-conducting electrolytes and ceria catalyst. The effects of composition, microstructure and strain are assessed as complementary tools for designing future SSIs.

2.2 Proton-conducting perovskite

Common proton-conducting perovskites include Sr or Ba-based zirconium ($BaZrO_3$), cerium ($BaCeO_3$), tin ($BaSnO_3$) and hafnium ($BaHfO_3$) oxide. Tantalum oxide ($KTaO_3$)[62-64], however, is less frequently used as an electrolyte due to its relatively low proton conductivity. Perovskites mentioned above have cubic or pseudo-cubic structures at working temperatures. A typical cubic perovskite structure is shown in Figure 2. One B-site ion is coordinated by 6 oxygen ions, forming a so-called oxygen octahedron or cage. One A-site ion, on the other hand, fills in the interstice surrounded by 8 BO_6 cages, making longer and weaker chemical bonds with nearest oxygen ions. Two types of the unit cells are presented: A-site centered one and B-site centered one.

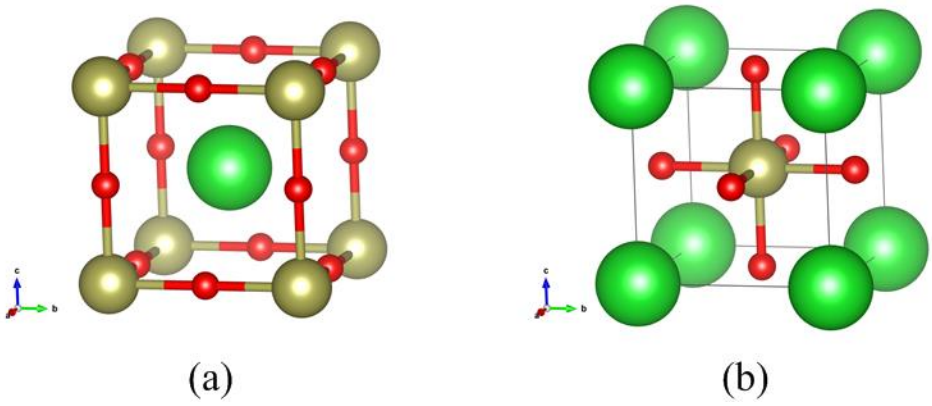

Figure 2 Cubic perovskite prototype: (a) A-site centered unit cell, (b) B-site centered unit cell. Large green balls are A-site ions, i.e. Ba; small bronze balls are B-site ions, i.e. Hf; small red balls are oxygen ions. B-O bonds are connected to show the coordination relations.

Proton-conducting perovskite needs to first incorporate proton species into its lattice through a so-called “hydration process”, before it conducts protons. A common proton source is the water molecule. To incorporate water molecules, perovskites need to be oxygen vacant. This is achieved by doping aliovalent dopants, specifically acceptor dopants. Oxygen vacancies are automatically created upon doping, by following the rule of charge neutrality within the whole lattice. The crystal structures of A and B-site doped perovskite are shown in Figure 3. Per two acceptor dopants are needed to produce one oxygen vacancy. Equations of doping processes with Kröger-Vink notations are shown below (using K on A-site and Y on B-site as examples):

$\boldsymbol{K_2O + 2Ba_{Ba}^{\times} + O_O^{\times} \rightarrow 2K_{Ba}' + V_O^{\cdot\cdot} + 2BaO}$ for A-site doping

$\boldsymbol{Y_2O_3 + 2Hf_{Hf}^{\times} + O_O^{\times} \rightarrow 2Y_{Hf}' + V_O^{\cdot\cdot} + 2HfO_2}$ for B-site doping

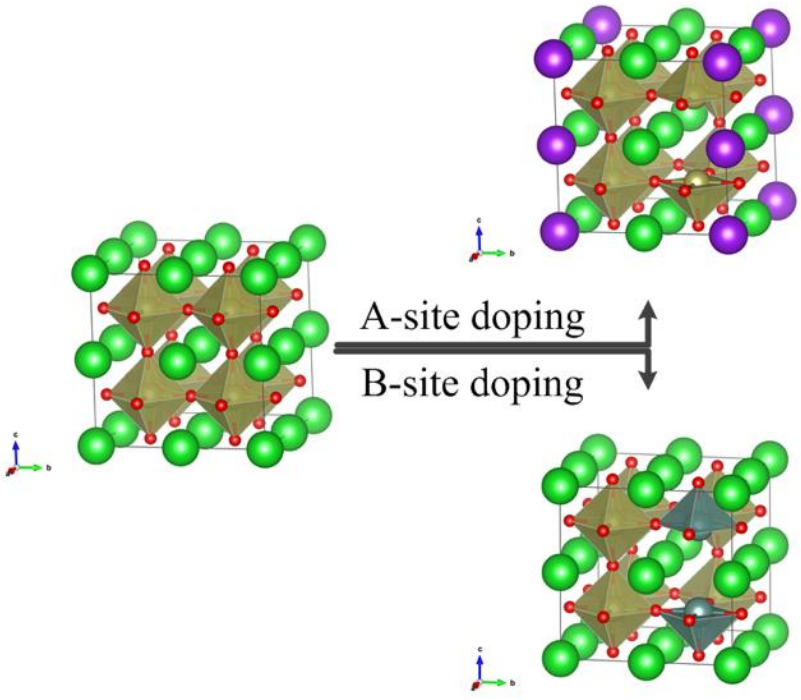

Figure 3 Defect chemistry of A-site and B-site doping in perovskite. A 2*2*2 supercell with oxygen octahedrons is shown on the left side before doping; defective supercells with 2 K ions on A-site or 2 Y ions on B-site and an oxygen vacancy are shown on the right side after doping. The color code is the same as in Figure 2. Purple ions: K; Cyan ions: Y. 12 K ions are shown on the plot because of the periodic boundary condition.

By absorbing water molecules, the perovskite's oxygen vacancies are filled. Simultaneously, protons are also incorporated into the lattice and bonded with lattice oxygen ions, forming a so-called "hydroxyl group", i.e. $OH_O^{\cdot}$. In the cubic perovskite, each oxygen ion has 4 symmetrically equivalent proton binding sites, shown in Figure 4. The proton can either rotate around the centroid oxygen ion or hop to nearby oxygen ions. A long-range proton conduction can be realized through a cooperative proton rotation and hopping processes.

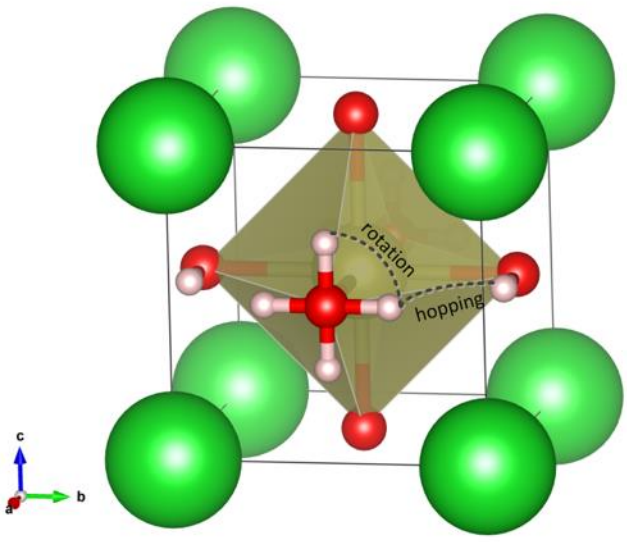

Figure 4 Potential proton binding sites in a cubic perovskite, together with the proton rotation and the hopping mechanisms. Each oxygen ion has 4 potential proton binding sites. The color code is the same as in Figure 2. Pale pink balls are protons.

Obviously, dopants in perovskites could affect their hydration property and proton mobility, including the kind of chemical dopant, dopant concentration, temperature and partial pressure of water in the environment, and even the mechanical strain. Here we show a diagram of ionic radius and electronegativity of A-site (Li, Na, K, Rb, Cs) and B-site (Al, Ga, In, Sc, Y, La, Gd, Lu) dopants, with their substituted host ions serving as the references. From Figure 5, it is seen that, w.r.t host ions, A-site alkali ions have widely-distributed ionic radii, B-site metalloids (Al, Ga, In) have higher electronegativities, and B-site rare-earth ions (Sc, Y, La, Gd, Lu) have larger ionic radii.

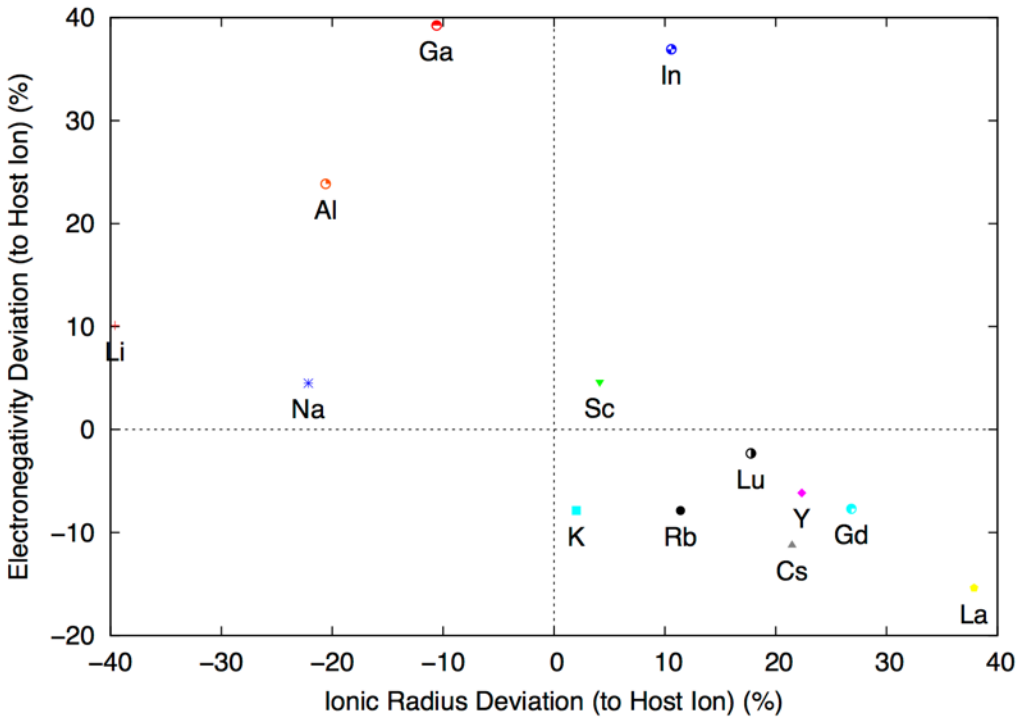

Figure 5 Ionic radii (Shannon's ionic radius in crystal)[65] and electronegativities (Pauling scale)[66] of A-site (Li, Na, K, Rb, Cs) and B-site (Al, Ga, In, Sc, Y, La, Gd, Lu)

dopants with the substituted host ions (Ba for A-site and Hf for B-site) as the reference.

Thermodynamic quantity of the proton-conducting perovskite is a combination of 0K electronic energy and finite temperature vibrational and configurational energies. Based on the thermodynamic quantity, the kinetic property can also be calculated with the information of the transition state, which can be captured from the static transition state theory or molecular dynamics simulations. Those quantities could characterize the hydration, proton binding, proton activation, proton vibration, chemical reactions, defect clustering, diffusion and conduction. Here is a list of each relevant quantity to be computed.

2.2.1 Defect formation energy

The defect formation energy of a defect with nominal charge q at 0K is defined as[67]:

$$\Delta E_{def} = E_{def}^{tot} + E_{corr}^{q} - E_{pef}^{tot} - \sum_{i} \Delta n_i \bar{\mu}_i + q(\epsilon_{VBM} + \mu_e + \Delta v^q)$$

where E_{def}^{tot} and E_{pef}^{tot} are the electronic total energies at 0K for defective and perfect supercells, Δn_i and $\bar{\mu}_i$ are the change of atomic amount and chemical potential (excluding zero-point energy, pure at 0K) of species i in elemental reference state; for defect with nominal charge q, energy correction term E_{corr}^{q} accounts for the electrostatic energy correction between defect and its periodic images from periodic boundary condition, ϵ_{VBM} is the energy of Valence-Band-Maximum, μ_e is the electron chemical potential w.r.t ϵ_{VBM}, Δv^q is the electrostatic-potential shift upon charged defect formation.

There are three versions of energy corrections for a charged defect:

1. Point-charge correction[68]

$$E_{PC}^{iso} = \frac{1}{2}\int_{\Omega}\left(-V_{PC,q}^{iso}\right)q\delta(\vec{r})d\,\vec{r} = \frac{\alpha q^2}{2\varepsilon L}$$

2. Markov-Payne correction[69]

$$E_{MP}^{iso} = E_{PC}^{iso} - \frac{2\pi qQ}{3\varepsilon L^3} + \frac{2\pi p^2}{3\varepsilon L^3} + \mathcal{O}(L^{-5})$$

3. FNV correction[70]

$$E_{FNV}^{iso} = E_{PC}^{iso} - q\Delta V_{PC,q/b}\big|_{far}$$

where q is the nominal charge of the defect, α is the Madelung constant of the defect lattice, ε is the dielectric constant from both electronic and ionic contributions, L is the lattice parameter assuming an equilateral lattice, Q is the second radial moment of the defect charge distribution, ΔV is the electrostatic potential shift caused by the charged defect.

At finite temperatures, the equation becomes:

$$\Delta G_{def} = G_{def}^{tot} + E_{corr}^{q} - G_{pef}^{tot} - \sum_i \Delta n_i \mu_i + q(\epsilon_{VBM} + \mu_e + \Delta v^q)$$

where G_{def}^{tot} and G_{pef}^{tot} are Gibbs free energy of defected and perfect supercells, μ_i is the chemical potential at finite temperatures and pressures and is defined as:

$$\mu_i(\mathrm{T}, p_i) = \bar{\mu}_i + \varepsilon_i^{Z.P.} + h_i^{\circ}(T) - Ts_i^{\circ}(T) + kT\ln\frac{p_i}{p_i^{\circ}}$$

where $\varepsilon_i^{Z.P.}$ is zero-point vibrational energy at 0K of species i, $h_i^\circ(T)$ and $s_i^\circ(T)$ are temperature-dependent enthalpy and entropy at standard partial pressure p_i° and are usually tabulated in NIST JANAF table. The last term accounts for the concentration/partial pressure dependence.

The Gibbs free energy of a solid is computed as:

$$G(T) = E^{tot} + H^{vib}(T) - TS^{vib}(T)$$

where $H^{vib}(T)$ and $S^{vib}(T)$ are the vibrational enthalpy and entropy and are evaluated through the solid's phonon frequencies, implemented in the vibrational partition function:

$$H^{vib}(T) = \sum_{q,s} \left(\frac{1}{2} \hbar w_{q,s} + \frac{\hbar w_{q,s}}{e^{\hbar w_{q,s}/kT} - 1} \right)$$

$$S^{vib}(T) = k \sum_{q,s} \frac{\hbar w_{q,s}/kT}{e^{\hbar w_{q,s}/kT} - 1} - k \ln\left(1 - e^{-\hbar w_{q,s}/kT}\right)$$

2.2.2 Dopant solubility

Dopant solubility is determined by the reaction equation shown below:

A-site doping:

$$2Ba_{Ba}^{\times} + O_O^{\times} + M_2O(s) + 2HfO_2(s) \rightarrow 2M'_{Ba} + V_O^{\cdot\cdot} + 2BaHfO_3(s)$$

$$\Delta_{diss}G = 2G_{M'_{Ba}} + G_{V_O^{\cdot\cdot}} - 3G_{perfect} + 2G_{BaHfO_3} - 2G_{HfO_2} - G_{M_2O}$$

B-site doping:

$$2Hf_{Hf}^{\times} + O_O^{\times} + M_2O_3(s) + 2BaO(s) \rightarrow 2M'_{Hf} + V_O^{\cdot\cdot} + 2BaHfO_3(s)$$

$$\Delta_{diss}G = 2G_{M'_{Hf}} + G_{V_O^{\cdot\cdot}} - 3G_{perfect} + 2G_{BaHfO_3} - 2G_{BaO} - G_{M_2O_3}$$

where $\Delta_{diss}G$ is the dissolution energy, G is the Gibbs free energy including 0K electronic energy and vibrational contribution from DFT calculations.

Based on the law of mass action, through computed dissolution energy, concentration of a dopant can be determined:

$$\exp\left(-\frac{\Delta_{diss}G}{RT}\right) = \left(\frac{[M'_{Ba}]}{[Ba_{Ba}^{\times}]}\right)^2 \frac{[V_O^{\cdot\cdot}]}{[O_O^{\times}]} \frac{a_{BaHfO_3(s)}^2}{a_{M_2O(s)}a_{HfO_2(s)}^2}$$

$$\exp\left(-\frac{\Delta_{diss}G}{RT}\right) = \left(\frac{[M'_{Hf}]}{[Hf_{Hf}^{\times}]}\right)^2 \frac{[V_O^{\cdot\cdot}]}{[O_O^{\times}]} \frac{a_{BaHfO_3(s)}^2}{a_{M_2O_3(s)}a_{BaO(s)}^2}$$

with mass conservations:

$$[M'_{Ba}] + [Ba_{Ba}^{\times}] = 1 \text{ or } [M'_{Hf}] + [Hf_{Hf}^{\times}] = 1$$

$$[V_O^{\cdot\cdot}] + [O_O^{\times}] = 3$$

$$[M'_{Ba}] = 2[V_O^{\cdot\cdot}] \text{ or } [M'_{Hf}] = 2[V_O^{\cdot\cdot}]$$

2.2.3 Hydration enthalpy/entropy and expansion coefficient

Hydration enthalpy/entropy and expansion coefficients are defined as the difference of the system enthalpy/entropy and the lattice parameter or volume before and

after hydration, i.e. absorbing a water molecule and forming two hydroxyl groups, i.e. $OH_O^{\cdot}$. The reaction equation is shown below:

$$H_2O + V_O^{\cdot\cdot} + O_O^{\times} \rightarrow 2OH_O^{\cdot}$$

The hydration enthalpy/entropy and volume/lattice expansion coefficients are then defined as:

$$\Delta_{Hydr}H = 2H_{OH_O^{\cdot}} - H_{V_O^{\cdot\cdot}} - H_{perfect} - H_{H_2O}$$

$$\Delta_{Hydr}S = 2S_{OH_O^{\cdot}} - S_{V_O^{\cdot\cdot}} - S_{perfect} - S_{H_2O}$$

$$\varepsilon_{hydr} = 2\varepsilon_{OH_O^{\cdot}} - \varepsilon_{V_O^{\cdot\cdot}}\ ,\ where\ \varepsilon_i = \frac{V_i}{V_0} - 1\ or\ \frac{a_i}{a_0} - 1$$

where H_i and S_i are the enthalpy/entropy of species or materials i. ε_i is the volume/lattice expansion coefficients of system i, with V_i and a_i the corresponding volume and lattice parameter.

The degree of hydration, i.e. $c[OH_O^{\cdot}]$, can be easily calculated from the Arrhenius relation:

$$K = \frac{c[OH_O^{\cdot}]^2}{c[V_O^{\cdot\cdot}]c[O_O^{\times}]p[H_2O]} = exp\left(\frac{\Delta_{Hydr}S}{R}\right)exp\left(-\frac{\Delta_{Hydr}H}{RT}\right)$$

where K is the equilibrium constant, c and p are the defect concentration and the external partial pressure. The concentration of species have constraints as:

$$c[V_O^{\cdot\cdot}] + c[O_O^{\times}] + c[OH_O^{\cdot}] = 1$$

$$2c[V_O^{\cdot\cdot}] + c[OH_O^{\cdot}] = c[dopant]$$

so that mass and charge balances are satisfied.

2.2.4 Dopant-proton/dopant-oxygen vacancy binding enthalpy

Binding enthalpy is calculated as the enthalpy difference between a cell with a neighboring defect pair and two cells each with one individual defect (assuming no defect-defect interactions). As pairs of dopant-proton and dopant-oxygen vacancy have electrostatic attractions, the binding energies usually show negative values. Binding enthalpy is also called "trapping enthalpy" in our case, which makes dopants trap protons and vacancies nearby. Use A-site doping as an example, the binding enthalpy is defined as:

$$H_{binding} = H_{A'_{Ba}-V_O^{\cdot\cdot}} - H_{A'_{Ba}} - H_{V_O^{\cdot\cdot}}$$

$$H_{binding} = H_{A'_{Ba}-OH_O^{\cdot}} - H_{A'_{Ba}} - H_{OH_O^{\cdot}}$$

2.2.5 Proton/oxygen vacancy migration enthalpy/entropy

The migration enthalpy and entropy constitute the migration energy, which determines the migration rate of a charge carrier by the Arrhenius equation shown below. In classical framework, we have:

$$\nu = \nu_0^{cl} \exp\left(-\frac{\Delta E}{k_B T}\right)$$

with the pre-factor ν_0^{cl} or so-called attempt frequency defined as:

$$\nu_0^{cl} = \frac{1}{2\pi} \frac{\prod_{i=1}^{N} w_i}{\prod_{i=1}^{N-1} w_i^{\ddagger}}$$

where N is the number of vibrational modes, w_i and $w_i^{\ddagger}$ are the frequencies of vibrational mode i for a system in initial and transition states. ‡ stands for the transition state. As we know, the transition state in our case, i.e. 1st order saddle point, has the vibrational degree of freedom of $N-1$. In the direction of the reaction coordinate, the vibrational mode is imaginary and does not contribute to the vibrational energy. ΔE is a classical vibrational energy V_m.

Under the quantum-level framework, however, the zero-point vibrational energy is non-negligible in the case of protons. Therefore, ΔE is calculated by considering the difference in summation of zero-point energy between the initial state (IS) and the transition state (TS):

$$\Delta E = V_m + \frac{1}{2}\sum_{i=1}^{N-1} \hbar w_i^{\ddagger} - \frac{1}{2}\sum_{i=1}^{N} \hbar w_i$$

At the same time, a more applicable description of the pre-factor from the vibrational partition function is:

$$\nu_0^{qm} = \frac{k_B T}{h} \frac{\prod_{i=1}^{N}(1 - e^{-\hbar w_i / k_B T})}{\prod_{i=1}^{N-1}(1 - e^{-\hbar w_i^{\ddagger} / k_B T})}$$

The quantum framework is universal and converges to the classical description at high temperatures. In our case, we do not consider the quantum tunneling and the polaronic

feature of proton transport, as they dominate only at extremely low temperatures below the room temperature.

2.2.6 Diffusivity and conductivity

Diffusivity, or diffusion coefficient under the dilute defect assumption, is calculated using the generic formula shown below[71]:

$$D = \frac{1}{2} f \sum_{k} \zeta_k \lambda_k^2 \Gamma_k^d$$

where f is the correlation-factor, summation is performed over each jump direction k with non-zero projections over the specified diffusion direction in one-dimension, ζ_k is the multiplicity of a direction k, λ_k is the projection length, Γ_k^d is the jump rate or jump frequency of defect d in crystallographic direction k. k determines the number of jump directions as well as jump frequencies.

However, the above model is only applicable for dilute defect species. Defect-defect interactions and configurations are unfortunately not included in the above model, making it insufficient to predict the diffusivity of non-dilute defect species. Statistical methods, e.g., kinetic Monte-Carlo, molecular dynamics, and cluster expansions, are needed to account for non-dilute defect diffusion. Detailed methods are shown in CHAPTER 3.

Conductivity, in the dilute-defect case, can only be estimated analytically. Conduction of ion flux is driven by the potential gradient of charge carriers, including the chemical potential and the electrical potential. In the dilute-defect case, the chemical

potential of charge carrier is solely governed by its concentration. Based on the Fick's first law, an ion flux J is defined as:

$$J = -D\nabla c - Bc\nabla U$$

in which D is the overall chemical diffusion coefficient driven by ∇c, the spatial gradient of carrier concentration, B is the single ion mobility scaling the velocity of the ion drift under the electric force or the electric potential energy gradient, i.e.,

$$v = BE = -B\nabla U$$

When ion velocity v is timed with concentration c, ion drift driven by the electric field is obtained. At equilibrium, $J = 0$, which is the condition of experimental electrochemical-impedance spectroscopy for conductivity measurement. Under this condition, the Einstein relation between mobility and diffusivity holds:

$$0 = -D\nabla c - Bc\nabla U = -D\frac{dc}{dU}\nabla U - Bc\nabla U$$

where the distribution of concentration c is governed by electric potential energy U as $c = Ae^{-\frac{U}{k_BT}}$. Thus, $\frac{dc}{dU} = -\frac{1}{k_BT}c$. The main equation becomes:

$$D\frac{1}{k_BT}c - Bc = 0$$

Namely, $B = \frac{D}{k_BT}$.

Conductivity is defined as the scaling-parameter between ion current density and applied electric potential bias $\phi = zeU$, thus

$$J = -D\frac{dc}{dU}\nabla U - Bc\nabla U = -D\frac{dc}{d\phi}\nabla\phi - zeBc\nabla\phi$$

where z is the nominal charge number of charge carrier, e is the elemental charge.

$$I = zeJ = -zeD\frac{dc}{d\phi}\nabla\phi - z^2e^2Bc\nabla\phi$$

Since the right-hand side of the equation has two terms balancing each other, chemical potential gradient-driven and electrical potential gradient-driven ionic drift equally contribute the ionic conductivity. Thus conductivity is defined as:

$$\sigma = z^2e^2Bc = \frac{z^2e^2Dc}{k_BT}$$

In electrochemical measurements, e.g. electrochemical impedance spectroscopy, the measured quantity is the ionic conductivity. Mobility/conductivity can also be defined as the quotient between ionic drift velocity/current density over the applied electric field. This is exactly how the ionic conductivity is measured experimentally.

2.2.7 Chemical stability against CO_2/H_2O: Carbonate/Hydroxide formation

Typical chemical degradation mechanisms for proton conductors are the carbonate/hydroxide phase formation under working conditions with CO_2/H_2O contaminants. The reaction equation is shown below. For A-site doping:

$$A_xBa_{1-x}HfO_{3-\frac{x}{2}} + (1-x)CO_2 \rightarrow \frac{x}{2}A_2O + (1-x)BaCO_3 + HfO_2$$

$$A_xBa_{1-x}HfO_{3-\frac{x}{2}} + (1-x)H_2O \rightarrow \frac{x}{2}A_2O + (1-x)Ba(OH)_2 + HfO_2$$

Similarly, for B-site doping:

$$BaB_xHf_{1-x}O_{3-\frac{x}{2}} + CO_2 \rightarrow \frac{x}{2}B_2O_3 + BaCO_3 + (1-x)HfO_2$$

$$BaB_xHf_{1-x}O_{3-\frac{x}{2}} + H_2O \rightarrow \frac{x}{2}B_2O_3 + Ba(OH)_2 + (1-x)HfO_2$$

The dissolution free energy is calculated in the same way as the hydration free energy. The solubility curve is obtained in the same way as the proton concentration.

2.2.8 Oxidation/reduction energy

Proton-conducting perovskite in SOFCs are sandwiched between the cathode and the anode, which are exposed to the strong oxidizing and reducing electro-chemical environment. Therefore, it has technical significance in investigating the electro-chemical stability of the perovskite under oxidation and reduction conditions. The reaction equation is shown below:

$\frac{1}{2}O_2(g) + V_O^{\cdot\cdot} \rightarrow 2h^{\cdot} + O_O^{\times}$ for the oxidation reaction

$O_O^{\times} \rightarrow \frac{1}{2}O_2(g) + V_O^{\cdot\cdot} + 2e'$ for the reduction reaction

From the above equations, we can see that the energy is closely related to the hole/electron state within the bandgap. Therefore, an accurate prediction of the bandgap and the defect state within the bandgap is crucial. Therefore, advanced exchange-correlation functionals beyond conventional DFT are required, e.g., DFT+Hartree-Fock, DFT+G_0W_0. Band alignment of Valence-Band-Maximum (VBM) and Conduction-Band-Minimum (CBM) using the surface vacuum level is necessary.

Use oxidation as an example, the oxidation energy is calculated as:

$$\Delta E_{ox} = 2\mu_e - \Delta E_v(\mu_e)$$

where μ_e is electron chemical potential w.r.t VBM and directly related to the band position. ΔE_v is the formation of $V_O^{\cdot\cdot}$. For charged defect, it is a function of electron chemical potential. To obtain ΔE_{ox}, μ_e needs to be solved by satisfying charge neutrality:

$$\sum_{def} qc_{def}(\mu_e) - n_e(\mu_e) + n_h(\mu_e) = 0$$

where n_e and n_h are the electron and hole concentration. Charge neutrality is achieved when the concentration of all ionic and electronic charge carriers are charge-balanced. n_e and n_h are defined as:

$$n_e = \int_{\epsilon_{CBM}}^{\infty} g(\epsilon) f(\epsilon, \mu_e) d\epsilon$$

$$n_h = \int_{-\infty}^{\epsilon_{VBM}} g(\epsilon)[1 - f(\epsilon, \mu_e)] d\epsilon$$

where $g(\epsilon)$ is the electron density of states (e-DOS) from DFT calculations, $f(\epsilon, \mu_e) = \{\exp[(\epsilon - \epsilon_{VBM} - \mu_e)/kT] + 1\}^{-1}$ is the Fermi-Dirac distribution function.

To obtain μ_e under the given temperature and partial pressure of O_2 and H_2O, a self-consistent way of minimization the charge balance equation towards zero is needed.

2.2.9 Clustering energy

To accurately characterize defect-defect interactions, evaluating clustering or association of defects at the microscopic level using statistical methods is necessary. Clustering energy is defined as the energy difference between a fully random structure and a ground-state structure. At 0K, this energy is solely determined by the electronic structure and the configurational entropy. When the temperature goes to finite, vibrational entropy comes into play, tailoring the defect order-disorder transition. A statistical method called cluster-expansion method is proposed to capture this physical picture.

2.2.10 Mean-Square-Displacement

Diffusivity and conductivity involving time and spatial correlations of defects can be captured through molecular dynamics simulations or kinetic Monte-Carlo methods. Hereby mean-square-displacements (MSD) can be generated by tracking charge carriers' moving trajectories. Diffusivity is the slope of the plot between MSD and sampled time interval Δt:

$$\mathrm{D} = \frac{1}{2Nd\Delta t}\sum_{i=1}^{N}\langle|r_i(t+\Delta t) - r_i(t)|^2\rangle_t$$

where d is the dimensionality of diffusion channel, in our case, is 3; N is the number of diffusing ions, $r_i(t+\Delta t)$ and $r_i(t)$ are the displacements of i-th ion at time $t+\Delta t$ and t, with the bracket averaging over time.

Similarly, conductivity can be calculated by the Nernst-Einstein equation:

$$\sigma = z^2 e^2 Bc = \frac{z^2 e^2 Dc}{k_B T}$$

The only difference between the conductivity calculated here and before by DFT is that the former method accounts for defect-defect interactions. Therefore, diffusion time-correlation can be incorporated into the simulation.

2.2.11 Time-Correlation and correlation factor

Concerted diffusion or correlated diffusion is common in non-dilute defect diffusion phenomenon. Therefore, to quantitatively examine and characterize this feature, the Van-Hove correlation function can be evaluated[72]:

$$\mathrm{G}_d(\mathrm{r}, \Delta t) = \frac{1}{4\pi r^2 Nn} \langle \sum_{i=1}^{N} \sum_{j=1, j\neq i}^{N} \delta(r - \left| r_i(t+\Delta t) - r_j(t) \right|) \rangle_t$$

where δ is the Dirac delta function.

Another concept is the Haven ratio[73], or correlation factor that characterizes the correlation effect in diffusion, defined as:

$$f = \frac{N D_\sigma}{D}$$

where D is the average diffusion over N ions, and D_σ is the diffusivity of the center of N ions:

$$D_\sigma = \frac{1}{2d\Delta t}\langle\left|\frac{1}{N}\sum_{i=1}^{N} r_i(t+\Delta t) - \frac{1}{N}\sum_{i=1}^{N} r_i(t)\right|^2\rangle_t$$

2.3 Space charge model in proton-conducting perovskite

Space charge layer is commonly seen in the proton-conducting perovskite with vacancies, protons, and aliovalent dopants segregation. Typically, it is formed due to the inhomogeneity of favorable occupancies across space. Examples include but is not limited to the surface segregation[13] and the grain boundary segregation [39] [74-76]. Segregation near dislocation receives much less attention in this type of materials, but it was studied in oxygen ion conductors such as $SrTiO_3$[54] and CeO_2[55].

In general, there are two ways of modeling space-charge formation: a continuum phase-field model and a discrete atomic-level model. A typical space-charge model starts with the definition of the electrochemical potential by combining electrostatic potential with chemical potential:

$$\tilde{\mu}_i(x) = \mu_i^0(x) + k_B T \ln\frac{c_i(x)}{1-c_i(x)} + q_i\varphi(x)$$

where $\tilde{\mu}_i$ is the electrochemical potential of defect species *i*, with contributions from the chemical potential μ_i^0 of pure defect species *i*, position-dependent concentration $c_i(x)$, and electrostatic potential $q_i\varphi(x)$. q_i is the nominal charge of defect species *i*. $\varphi(x)$ is the position-dependent electric potential.

By solving the Poisson equation:

$$\frac{d^2\Delta\varphi(x)}{dx^2} = -\frac{\rho(x)}{\varepsilon}$$

with charge density given by:

$$\rho(x) = \sum_i eq_i\, c_i(x)$$

under the equilibrium condition that electrochemical potential of defect species *i* across interface and bulk region are all the same:

$$\mu_i^0(x) + k_B T \ln\frac{c_i(x)}{1-c_i(x)} + q_i\varphi(x) = \mu_i^0(\infty) + k_B T \ln\frac{c_i(\infty)}{1-c_i(\infty)} + q_i\varphi(\infty)$$

with ∞ denoting the bulk-like region.

The driving force for the defect segregation is simply the thermodynamic defect formation energy difference under electrostatic potential between the near-interface and the bulk-like positions, which is typically calculated from DFT:

$$\Delta E_{seg}(x) = E_f(x) - E_f(\infty)$$

where the equilibrium space-charge profile $c_i(x)$ and electric potential profile $\varphi(x)$ can be obtained. ε is the static dielectric constant.

Another way of simulating space-charge layer is by preforming the discrete atomic-level simulations. To account for the segregation tendency from both "immobile" aliovalent dopants and "mobile" protons or oxygen vacancies, a so-called "Hybrid MC-

MD" algorithm is devised. Namely, Monte-Carlo method is used to swap dopants within the lattice, while a molecular dynamics run allows the moving of protons or oxygen vacancies. By having interlaced MC-MD simulations, equilibrium positions of both immobile and mobile defects can be secured. After numerous MC-MD loops, the "co-segregation" phenomenon can be captured. As demonstrated before, dopants and vacancies tend to co-segregate to the tensile region, and *vice versa*[54, 55].

2.4 Ionic defects in ceria

The most common ionic defects in ceria are oxygen vacancies and polarons. An intrinsic oxygen vacancy in ceria is created upon reduction, followed by oxygen gas releasing and back-donations of two electrons from the *2p* orbital of an oxygen ion to the lattice. These two electrons prefer to localize on nearby Ce ions and occupy Ce's *4f* orbital[77]. The polaron position w.r.t vacancy in bulk ceria is sensitive to the bulk lattice parameter or pressure[58]. In other words, different defect configurations have different mass densities. Imagine a macroscopic bulk ceria containing a variety of defect configurations locally, with each local zone a distinct mass density. This is also called "density fluctuation" in solid state ionic materials. Besides of defect thermodynamics, it was also found in the bulk ceria that an oxygen ion migration can be coordinated with polarons hopping, a so-called "concerted" migration process[78]. In terms of ceria surface, it was discovered from both theoretical calculations and STM images that vacancies on the ceria (111) surface reside preferably on the sub-surface oxygen layer[61, 79]. Surprisingly, polarons were observed to reside at the 2$_{nd}$-nearest-neighbor, rather than the 1$_{st}$-nearest-neighbor of the corresponding oxygen vacancy. This counter-intuitive discovery was later

found to be from the elastic origin[59]. Since polarons and vacancies are both larger than original Ce^{4+} ions and oxygen ions, bond shortenings between them are energetically costly.

Since the conventional DFT is not able to accurately capture the electron localization of Ce's *4f* orbital, DFT+U with a U parameter on Ce's *4f* orbital is required. Spin-polarized DFT with Hubbard on-site Coulomb interaction correction (rotationally invariant introduced by Dudarev et al. [80]) should be applied to account for the self-interaction error of unpaired *4f* electrons. The DFT+U correction scheme is shown below:

$$E_{DFT+Ueff} = E_{DFT} + \frac{U-J}{2}\sum_{\sigma}\left[\left(\sum_{m1} n^{\sigma}_{m1,m1}\right) - \left(\sum_{m1,m2} n^{\sigma}_{m1,m2} n^{\sigma}_{m2,m1}\right)\right]$$

where n is the occupation matrix with angular momentum $m1$ or $m2$ as its element indices; σ is the spin index, denoting the spin-up or spin-down channel; U is the Coulomb repulsion between electrons and J describes the electron exchange interactions; $n^{\sigma}_{m1,m1}$ thus denote the diagonal elements of the occupation matrix representing the electron wavefunction interactions within the same angular-momentum orbital, while $n^{\sigma}_{m1,m2}$ corresponds to the off-diagonal ones.

CHAPTER 3 METHODOLOGY

In this chapter, we provide a detailed description of each technical methods being used in the dissertation. It include density functional theory, phonon theory, nudged-elastic band method, cluster expansion method, special quasi-random structures, lattice Monte-Carlo and molecular dynamics.

3.1 Density functional theory

The basic idea of density functional theory is contained in the two original papers of Hohenberg, Kohn, and Sham[81, 82], referring as the Hohenberg-Kohn-Sham theorem. Instead of dealing with the many-body Schrödinger equation, which involves the many-body electronic wavefunctions $\psi(\{r_i\})$, one deals with a formulation of the problem that involves the total density of single-electron $\rho(r)$, which is a function of the electron position r. This huge simplification, or alteration of problems, neglects the details of the many-body wavefunctions. Instead, it describes the behavior of the system with the appropriate single-particle equation as a functional of the charge density.

The energy of the system is considered as the sum of several components:

$$E = E[\rho(r)] = T[\rho(r)] + V_{ext}[\rho(r)] + V_{Hatree}[\rho(r)] + E_{xc}[\rho(r)]$$

where $T[\rho(r)]$ is the kinetic energy of the electrons summed up, $V_{ext}[\rho(r)]$ is the potential energy of the electrons with respect to the external potential induced by ions or lattice, $V_{Hatree}[\rho(r)]$ is the electron-electron Coulombic interactions, with $E_{xc}[\rho(r)]$ accounting for the many-body effect of electrons and standing for the exchange-correlation energy of electrons.

When the three terms $V_{ext}[\rho(r)] + V_{Hatree}[\rho(r)] + E_{xc}[\rho(r)]$ are all treated as an effective external potential, the Kohn-Sham equation is then the Schrödinger equation of a fictitious system of non-interacting electrons that generate the same density as any given system of interacting particles. The equation is shown below:

$$(T[\rho(r)] + V_{ext}[\rho(r)] + V_{Hatree}[\rho(r)] + E_{xc}[\rho(r)])\psi(r) = E\psi(r)$$

where E is the total energy of the system.

Since the exchange-correlation term $E_{xc}[\rho(r)]$ depends on $\rho(r)$, which needs to be solved in the Kohn-Sham equation together with $\psi(r)$. Therefore, $\rho(r)$ depends on itself. The procedure of solving the Kohn-Sham equation has to be done in a self-consistent way.

$E_{xc}[\rho(r)]$ is approximated initially via a local-density approximation (LDA)[81]:

$$E_{xc}[\rho(r)] = \int dr \cdot \rho(r)\varepsilon_{xc}([\rho(r)], r)$$

with ε_{xc} the exchange-correlation energy per particle of a homogeneous electron gas with charge density ρ. To account for the inhomogeneity of the true electron density, the gradient of charge density is included. This allows for correction from electron density away from the coordinate. It is referred as the generalized gradient approximation (GGA)[83]:

$$E_{xc}[\rho(r)] = \int dr \cdot \rho(r)\varepsilon_{xc}([\rho(r), \nabla\rho(r)], r)$$

There are many versions of GGA, developed or parameterized by different groups of people at various times, e.g., PW91[84], PBE[85], RPBE[86], PBEsol[87], AM05[88].

Hybrid functional incorporates a portion of the exact exchange from the Hartree-Fock theory with the rest of DFT exchange-correlation functional. The improvement can be dramatic in band-gap prediction and the polaronic behavior of electrons in insulating materials. Hartree-Fock exact exchange functional is defined as:

$$E_x^{HF} = -\frac{1}{2}\sum_{i,j}\iint \psi_i^*(r_1)\psi_j^*(r_1)\frac{1}{r_{12}}\psi_i(r_2)\psi_j(r_2)dr_1dr_2$$

An example of hybrid functional, i.e. PBE0[89], is defined as:

$$E_{xc}^{PBE0} = \frac{1}{4}E_x^{HF} + \frac{3}{4}E_x^{PBE} + E_c^{PBE}$$

where E_x^{HF} is the Hartree-Fock exact exchange functional, E_x^{PBE} is the PBE exchange functional, E_c^{PBE} is the PBE correlation functional.

DFT calculations can be performed using Vienna *ab-initio* Simulation Package (VASP)[90, 91].

3.2 Phonon theory

In the harmonic approximation of low-temperature crystals, the potential energy of a crystal w.r.t the vibration of nuclei can be written as[92]:

$$U_{harm} = E_{perf} + \frac{1}{2}\sum_{lsα,l'tβ}\Phi_{lsα,l'tβ}u_{lsα}u_{l'tβ}$$

where U_{harm} is the internal energy of a crystal, E_{perf} is the energy of a crystal from the electronic structure within a static lattice, and the second term on the right denotes the

potential energy change due to nuclei displacements. $u_{ls\alpha}$ is the displacement of atom s in unit cell l along Cartesian direction α, same for $u_{l't\beta}$. $\Phi_{ls\alpha,l't\beta}$ is the force-constant matrix, or Hessian-matrix, given by the double-derivative of internal energy against two displacements, i.e. $\frac{\partial^2 U}{\partial u_{ls\alpha}\partial u_{l't\beta}}$, while keeping all other atoms at their equilibrium positions. From here, the relation between force and displacement can also be derived:

$$F_{ls\alpha} = -\partial U/\partial u_{ls\alpha} = -\sum_{l't\beta} \Phi_{ls\alpha,l't\beta} u_{l't\beta}$$

If the volume change from thermal expansion is also taken into consideration, then the force-constant matrix also depends on the equilibrium lattice parameters at each temperature. Therefore, the Helmholtz free energy can be calculated as:

$$F(V,T) = E_{perf}(V) + F_{harm}(V,T)$$

where the harmonic vibration energy can be evaluated from the Bose-Einstein distribution equation of phonon:

$$F_{harm} = k_B T \sum_n \ln(2\sinh(\hbar\omega_n/2k_B T))$$

with ω_n the frequency of nth vibrational mode. In the harmonic approximation, the volume dependence of ω_n has not to be counted. Specifically, in a periodic crystal system, a summation of ω_n needs to include the whole range of wave-vector q. Thanks to the point group symmetry and translational invariance of a periodic crystal, the

summation can only take over the irreducible Brillion zone (IBZ), corresponding to the primitive cell in real space:

$$F_{harm} = \frac{k_B T}{\Omega} \int_{IBZ} dq \sum_{s} \ln\left(2 \sinh\left(\hbar\omega_{qs}/2k_B T\right)\right)$$

Alternatively, F_{harm} can also be calculated from integration over phonon density of states $g(\omega)$:

$$F_{harm} = k_B T \int_{0}^{\infty} d\omega \, g(\omega) \ln(2 \sinh(\hbar\omega/2k_B T))$$

where $g(\omega)$ is normalized to the number of phonon branches when integrating the whole frequency range.

The vibrational frequencies ω_{qs} are the eigenvalues of the dynamical matrix, $D_{s\alpha,t\beta}(q)$, defined as:

$$D_{s\alpha,t\beta}(q) = \frac{1}{\sqrt{M_s M_t}} \sum_{ll'} \Phi_{ls\alpha,l't\beta} \, exp[iq \cdot (R_{l'} + \tau_t - R_l - \tau_s)]$$

where $R_{l'} + \tau_t$ represents the equilibrium position of atom t in primitive cell l, the summation is over all possible combination of primitive cell l and l'. M_s is the atomic mass of atom s.

The calculation of phonon has two methods: small-displacement, direct or frozen-phonon method; linear-response method from density functional perturbation theory. For

the former method, the supercell needs to be large enough so that elements of the force-constant matrix fall off to negligible values at the boundary of the super-cell. This is easily achievable in metallic systems, but not for ionic solids. It is due to the nearly zero wave-vector vibrational mode creates an artificially macroscopic electric field, which causes the so-called LO-TO (LO: Longitudinal Optical; TO: Transverse Optical) splitting in ionic solids. In this special case, the dynamic matrix has a non-analytical form:

$$D^{na}_{s\alpha,t\beta} = \frac{1}{\sqrt{M_s M_t}} \frac{4\pi e^2}{\Omega} \frac{(q \cdot Z^*_s)_\alpha (q \cdot Z^*_t)_\beta}{q \cdot \epsilon^\infty \cdot q}$$

where Z^*_s is the Born effective charge tensor (3×3 matrix) for atom s, ϵ^∞ is the high-frequency static dielectric tensor. q is the wave vector. $(q \cdot Z^*_s)_\alpha$ is the α Cartesian composition in the projection of Born effective charge along wave vector. $q \cdot \epsilon^\infty \cdot q$ represents the projection of dielectric tensor into wave vector q.

For the linear-response method, the use of the Hellman-Feynman theorem gives atomic forces by perturbing the Kohn-Sham Hamiltonian under un-perturbed wave functions[93].

Phonon calculations can be performed and analyzed by Phonopy developed by Dr. Atsushi Togo[94].

3.3 Nudged elastic band

The nudged elastic band (NEB) method is a chain-of-states method in which a string of images is constructed to represent the reaction pathways. The pathway converged from NEB is usually called the minimum energy pathway (MEP) with at least one saddle

point. The convergence criterion is minimizing the NEB force on each image of the string, i.e. F_i^{NEB}, which is defined as:

$$F_i^{NEB} = F_i^{\perp} + F_i^{S\parallel}$$

where $F_i^{\perp}$ is the true DFT force from potential energy surface perpendicular to the string,

$$F_i^{\perp} = -\nabla(R_i) + \nabla(R_i) \cdot \hat{\tau_i}\hat{\tau_i}$$

and $F_i^{S\parallel}$ is the NEB string force in parallel to the string.

$$F_i^{S\parallel} = k(|R_{i+1} - R_i| - |R_i - R_{i-1}|)\hat{\tau_i}$$

$\hat{\tau_i}$ and R_i is the tangent of the string and position vector at image i, k is the spring constant of the string.

NEB calculations can be performed with the aid of the VTST package developed by Prof. Graeme Henkelman's group[95].

3.4 Cluster expansion

Cluster expansion is a method to describe configurational disorder and its effect on free energy. It describes substitutional degrees of freedom in the partition function. The expansion is over a variety size of clusters, e.g., singlet, doublet, triplet, that each cluster is a combination of occupation variable characterizing on-site occupancy status. Specifically, for cluster α, its configurational state φ_α is:

$$\varphi_\alpha = \prod_{i \in \alpha} \sigma_i$$

where σ_i is the occupation variable for site i, i.e. ± 1 for occupied or not, or for occupied by species A or B. φ_α forms a complete and orthonormal basis for describing any property of a specific configuration, e.g., energy, volume. Therefore, a cluster expansion description of configurational energy takes the form

$$E = V_0 + \sum_\alpha V_\alpha \varphi_\alpha$$

where the expansion goes over all sizes of clusters, starting from singlet to large clusters till a satisfactory convergence towards E. V_0 and V_α are fitted expansion coefficient from DFT or semi-empirical MD calculations, often called effective cluster interactions (ECIs).

It is possible that multiple sublattices contain substitutional disorder, in which case a composite basis made from each sublattice basis function is needed. For example, for sublattice α and β, each with a basis function φ_α and θ_β, contribute to the new basis function $\psi_{\alpha\beta}$:

$$\psi_{\alpha\beta} = \varphi_\alpha \theta_\beta$$

ECIs are largely defined by the atomic orbital overlap in the metallic system, but have multiple factors in ionic solids. Besides orbital overlap, or covalent interaction between ions, which is rare in localized d and f orbitals or closed-shell ions, there are steric effects, partially due to ionic size, and electrostatic effects. Especially for strong-ionic crystals with coherent dopant ionic radius to the host, electrostatic energy, or Madelung energy, can be dominant.

The goal of utilizing cluster expansion is to predict configurational entropy of crystal without exhausting all possible configurations but rather predict arbitrary configuration's energy through a small set of configurations. The relevant calculations are performed *via* the Alloy Theoretic Automated Toolkit (ATAT)[96, 97].

3.5 Special quasi-random structures

In the scenario of the high-temperature limit, defects of various kinds tend to be fully randomized. In order to describe the correlation function of randomly mixed ions in a periodic supercell, a so-called "quasi-random" structure[98] can be adopted. By approximating the correlation function of real random structure with that of local random structure up till a few Angstrom of atomic distance, accurate enough properties such as phonon spectrum[99], elastic constant[100] and electronic structure[101] can be predicted. For instance, the ensemble average of a physical property P over configurations can be described as an expansion over clusters:

$$\langle P \rangle = \sum_{k,m} D_{k,m} \langle \overline{\Pi}_{k,m} \rangle p_{k,m}$$

where $p_{k,m}$ is local property of cluster with size k and m$_{th}$ distance, $D_{k,m}$ is the multiplicity of this k,m-type of the cluster, $\langle \overline{\Pi}_{k,m} \rangle$ are the correlation functions.

Instead of approaching $\langle P \rangle$ with statistical sampling, people can construct a special supercell S with distinct correlation functions $\overline{\Pi}_{k,m}(S)$ best match the ensemble averages $\langle \overline{\Pi}_{k,m} \rangle_R$ of random alloys, so that the difference of property is minimized:

$$\langle P \rangle_R - P(S) = \sum_{k,m} D_{k,m} \left[(2x-1)^k - \overline{\Pi}_{k,m}(S) \right] p_{k,m}$$

3.6 Lattice Monte-Carlo

Metropolis Monte-Carlo for lattice point swapping is listed briefly as below:

Start at an initial lattice configuration, calculate its energy; loop through all lattice points: for each point, swap it with a random point and calculate the energy difference ΔU. If $\Delta U < 0$, it indicates a thermodynamically more stable configuration and accepts this swap; otherwise, the probability from Boltzmann distribution W is calculated as

$$W = \exp\left(\frac{-\Delta U}{kT}\right)$$

and compared with a random number R from 0 to 1. If W>R, accept this swap; otherwise, reject this swap. Go to the next point. After looping through all points, it is called an MC step. Numerous MC steps are needed to ensure the system reaches equilibrium, e.g., lattice energy fluctuation converges to a certain threshold.

Thermodynamic quantities such as free energy can be calculated through ensemble averaging.

3.7 Molecular dynamics

Molecular dynamics is a computer simulation technique of studying physical vibrations or trajectories of atoms and molecules, by solving the many-body Newton's equation of motion. Give atoms initial positions and velocities, and choose time step Δt. Update atoms positions and velocities by applying last step velocity and acceleration.

Calculate atomic forces from potentials or force fields, which are usually functions of atomic positions. Apply boundary conditions, temperature and pressure controls if needed. Update simulation time by time step and iteration count. Loop over as many times as needed. Classical molecular dynamics can be performed via the Large-scale Atomic/Molecular Massively Parallel Simulator (LAMMPS)[102], and *ab-initio* molecular dynamics can be performed via Vienna *ab-initio* Simulation Package (VASP). For classical MD, force-field is either a static function or functional of atomic positions, bond order, etc. Specifically, ReaxFF developed by Adri Van Duin, et al.[57] with force field fitted for Y:$BaZrO_3$ is available, with a comprehensive description of interaction energy:

$$E_{system} = E_{bond} + E_{lp} + E_{over} + E_{under} + E_{val} + E_{pen} + E_{coa} + E_{C2} + E_{triple} + E_{tors} + E_{conj} + E_{H-bond} + E_{vdWaals} + E_{Coulomb}$$

where the contribution of each energy term is from, E_{bond} bond order, E_{lp} lone pair, E_{over} over-coordination, E_{under} under-coordination, E_{val} valance angle terms, E_{pen} penalty term, E_{coa} three-body conjugate term, E_{C2} correction for C_2-molecule, E_{triple} triple bond energy correction, E_{tors} torsion angle terms, E_{conj} four-body conjugate term, E_{H-bond} hydrogen bond interactions, $E_{vdWaals}$ van der Waals interactions, $E_{Coulomb}$ Coulomb interactions. The use of ReaxFF can accurately capture the protonic features (e.g. polarizability) by having electronic structure information cast in bond-order formalism, without expensive quantum mechanics computations.

For *ab-initio* MD, the atomic forces are calculated on-the-fly from ground state electronic wavefunction:

$$M_I \ddot{R}_I(t) = -\nabla_I \langle \Psi_0 | H_e | \Psi_0 \rangle$$

where M_I is the mass of ion I, $\ddot{R}_I(t)$ is the acceleration of ion I at time t, Ψ_0 is the ground state electronic wavefunction, H_e is the electronic Hamiltonian.

CHAPTER 4 RATIONAL DESIGN OF A/B-SITE DOPED $BAHFO_3$

4.1 Abstract

$BaHfO_3$ (BHO) is a novel yet rarely studied proton-conducting perovskite. In this work, 13 dopant candidates, including 5 A-site alkali (Li, Na, K, Rb, Cs), 3 B-site metalloid (Al, Ga, In), and 5 B-site rare earth (Sc, Y, La, Gd, Lu) elements are screened, *via* the evaluation of dopant solubility, proton concentration, proton diffusivity, and materials stability against CO_2/H_2O. A-site and B-site dopants such as K and Sc are recommended because of their overall outstanding properties in doped-BHO. A-site dopants significantly promote hydration capability, while B-site ones demonstrate consistent hydration suppressions. Specifically, A-site dopants with smaller ionic radii give higher hydration capability, while B-site dopants with medium ionic radii give the lowest hydration capability (e.g. In). A-site dopants demonstrate negligible "trapping" effects on proton mobility, probably due to the long distance between the A-site and the proton-site. A "volcano-shaped" relation between binding energies and ionic radii of dopants, with energy crossings of the 1_{st}-nearest-neighbor (1NN) and the 2_{nd}-nearest-neighbor (2NN) proton binding sites, indicates a delicate elastic-electrostatic balance among defects. Interestingly, high electronegativity of In creates a "valley" in the "volcano plot", indicating a poor proton mobility near In. BHO with A-site dopants such as K demonstrate excellent chemical stability against CO_2, which is crucial for the materials durability under working conditions.

4.2 Introduction

Proton-conducting perovskites are promising materials used as electrolytes in solid oxide fuel cells. Proton-conducting mechanism and materials composition design received extensive experimental and computational investigations. Especially, theoretical calculations based on density functional theory[103] were demonstrated as a powerful tool in predicting charge carrier concentration and mobility within solid-state ionic conductors. Thermodynamic, kinetic, and electronic properties of protons in $BaZrO_3$[12-15, 18, 20, 21, 24, 28, 30, 32-34, 36, 37, 39, 41, 42, 67, 104] (or BZO), $BaCeO_3$[50-52, 105] (or BCO) and $BaSnO_3$[44-46, 48, 106, 107] (or BSO) systems have been intensively studied by DFT-based calculations, together with kinetic Monte-Carlo and molecular dynamics simulations. However, investigations of the dopant selection and the doping level optimization for $BaHfO_3$-based materials are yet to be performed, either computationally or experimentally[108].

N. Bork et al.[109] carried out DFT calculations and found a negative linear correlation between $OH_O^{\cdot}$ group formation energy from hydrogen gas and proton hopping/rotation energy barriers. However, the $OH_O^{\cdot}$ group formation energy is slightly different from the hydration energy defined and computed in the current work, as they use H_2 as the reference proton source and treat H as neutral species in the lattice. A series of pure perovskites, e.g., (Ca/Sr/Ba/Pb)(Ti/Zr/Nb/Mn)O_3 were tested. However, the materials they computed are not necessarily qualified for solid electrolytes in SOFCs but rather for materials in hydrogen permeation membranes, as the electronic conductivity can be expected in Nb/Mn-based perovskites. Nevertheless, the concept of competition between

proton concentration and mobility could be universal and waiting to be tested in the doped $BaHfO_3$.

Per G. Sundell et al.[40] did a comprehensive study on pre-factors and energy barriers of the proton diffusion in $BaZrO_3$ via DFT calculations in the classical, semi-classical and quantum scenarios. Zero-point vibrational frequencies play distinct roles in the classical and the semi-classical scenarios, making the prediction of pre-factors and energy barriers different. Quantum tunnelling of protons at extremely low temperature was also discussed. A similar investigation was also reported for $BaSnO_3$[47].

Beyond investigations of pure perovskites, dopants in doped-perovskites have also been widely studied. Yamazaki et al.[110] reported experimentally the dopant trapping energy and the proton migration energy to be 29 kJ/mol and 13~16 kJ/mol, proving that dopant trapping effect is detrimental to proton transport. It is actually widely accepted in the community of solid state ionic materials that acceptor dopants (with a negative effective charge) can electrostatically trap positively charged charge carriers such as oxygen vacancies and protons, preferably in 1_{st}-nearest-neighbor (1NN). However, acceptor dopants with larger ionic radii than host cations can have elastic repulsions with oxygen vacancies and/or protons at the 1_{st}-nearest-neighbor, pushing those charge carriers further away to the 2_{nd} or 3_{rd}-nearest neighbours. This elastic-electrostatic interaction balance was widely observed in doped CeO_2[111], $BaZrO_3$[15], $BaCeO_3$[105] and $BaSnO_3$[45]. Hydration enthalpy, another major quantity governing proton concentration in the lattice, was also found to be affected by dopant's ionic radius and electronegativity. In $BaSnO_3$, it was found that larger the ionic dopant, less favourable the hydration process[45]. Besides,

dopants with higher electronegativity tend to increase the hydration enthalpy and disfavour the hydration process, probably due to its over-stabilization of dopants binding with vacancies. Experimental investigation on $BaZrO_3$ also found a strong correlation between dopant ionic radius and proton conductivity[112]. Therefore, an "optimal" dopant with a suitable ionic radius and electronegativity exists in the host material.

Using computational methods, Kim et al.[113] recently discovered that proton trapping effects from acceptor dopants can be effectively screened and suppressed by the clustering of oxygen vacancies near those dopants. This was demonstrated in In-doped $BaZrO_3$ and $BaCeO_3$, where oxygen vacancies near In can effectively screen the electrostatic attraction between In and protons. This is fundamentally due to a weak hybridization between In's low lying $4d^{10}$ states and O's 2p states, such that In's valence electron density does not get affected much by the vacancy nearby. This points out a novel strategy of alleviating proton trapping, simply by an adequate annealing procedure and vacancy equilibration near In. By doing that, oxygen vacancies are allowed to segregate close to those acceptor dopants *via* thermal diffusion. On the contrary, vacancies will be randomly distributed within the lattice in the absence of annealing, which is a kinetically stable but thermodynamically metastable state frozen from the high-temperature state.

In addition to the dopants' chemistry, dopants configurations also affect the properties in the proton-conducting perovskites. Takahashi et al.[42] demonstrated computationally that isolated and associated dopants within $BaZrO_3$ result in distinct hydration capabilities. From their calculations, it was realized that perovskites with associated dopants tend to get more easily hydrated than the case of isolated ones.

Therefore, it is a potentially effective way of enhancing the hydration capability by promoting dopant associations *via* extensive thermal annealing.

$BaHfO_3$-based materials have a proton conductivity similar to that of $BaZrO_3$-based materials; however, the chemical stability of the former is inherently better than that of the latter. A recent computational study of perovskite-based proton conductors[10] suggested $BaHfO_3$ as a novel proton-conducting perovskite regarding to the conventional $BaZrO_3$. Although they share the similarity, subtle differences between them need to be understood through accurate quantum mechanical based calculations.

4.3 Computational methods and models

DFT calculations are performed via Vienna *ab-initio* Simulation Package (VASP)[90]. Periodic lattice model with a 2×2×2 40-atom supercell is used for most of the energy calculations. A 4×4×4 Monkhorst-Pack KPOINTS[114] with an energy cutoff of 520 eV is used to ensure an energy accuracy of 1 meV per structure. Planewave basis set of exchange-correlation functional with generalized-gradient approximation parameterized by Perdew, Burke and Eernzerholf (GGA-PBE)[85] is used, with pseudopotentials of Ba_sv, Hf_pv, O, H and dopants (Li_sv, Na_sv, K_sv, Rb_sv, Cs_sv, Sc_sv, Y_sv, La, Gd, Lu, Al, Ga_d, In_d). To extrapolate from the 0K energy to the finite temperature Gibbs free energy, vibrational contribution is evaluated via calculations of the phonon density of states in relevant structures. By utilizing a linear response (perturbation theory) or a supercell method (finite-difference), vibrational frequencies of supercells are obtained. Thermodynamic quantities are then evaluated in the vibrational partition function. By replacing one A-site or B-site host ion with an acceptor dopant, a 12.5% site-concentration

of doping is created. Similarly, supercells with one oxygen vacancy and one extra proton bonded with the lattice oxygen are also created to simulate the status before and after hydration. With a dopant inside the lattice, stability and mobility of the vacancy and the proton are expected to be position-dependent. Therefore, the proton and the vacancy are put at the 1st-nearest-neighbor (1NN) and the 2nd-nearest-neighbor (2NN) near the dopant. As we inevitably create supercells with an extra electronic charge, the energy correction of a charged supercell is taken into consideration (*vide infra*). The mobility of protons is evaluated by calculating the transition state energy through searching for the minimum migration energy pathway using the standard Nudged Elastic Band (NEB) method. The binding energy between dopant and proton due to electrostatic attraction is expected to play an important role in proton mobility, which is supposed to be largely related to the ionic radius and electronegativity of dopants. It is believed that a "trade-off" exists between proton mobility and concentration, where it is eventually attributed to the dopant's binding energy with proton and effect on hydration energy. To evaluate dopant solubility and doped-BHO's chemical stability, the reaction energy is calculated by evaluating energies of reactants and products involved. Detailed reaction formulas are shown *vide infra*. Estimation of proton conductivity is carried out *via* a dilute defect diffusion theory and the Nernst-Einstein equation, with calculated thermodynamic quantities as the input.

Representative supercells in the calculations are shown in Figure 6, including perfect BHO, doped-BHO, a vacancy in BHO, a proton in BHO, a dopant + a proton in BHO (1NN&2NN), a dopant + a vacancy in BHO (1NN&2NN).

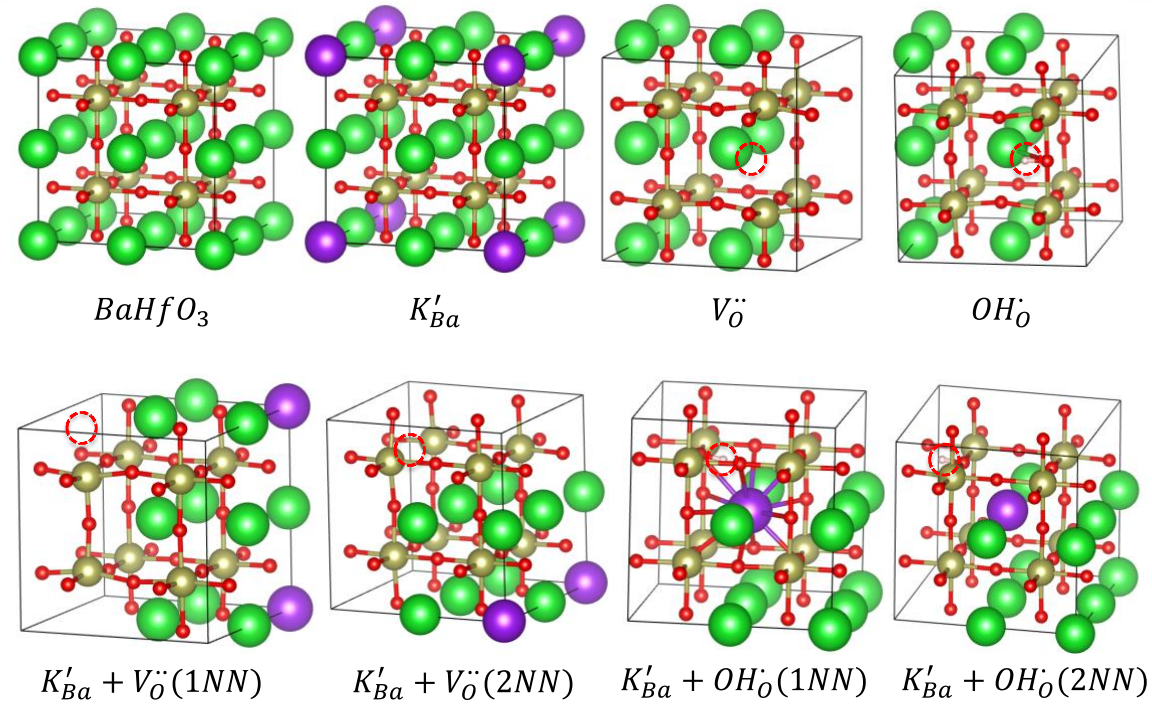

Figure 6 Representative supercells in the calculations, with defect configurations in the Kröger-Vink notation: $BaHfO_3$, K'_{Ba}, $V_O^{\cdot\cdot}$, $OH_O^{\cdot}$, $K'_{Ba} + V_O^{\cdot\cdot}(1NN)$, $K'_{Ba} + V_O^{\cdot\cdot}(2NN)$, $K'_{Ba} + OH_O^{\cdot}(1NN)$, $K'_{Ba} + OH_O^{\cdot}(2NN)$. Color coding: Emerald, Ba; bronze, Hf; red, O; pale pink, H; Purple, K. Dotted red circle marks the positions of vacancy and proton.

4.4 Results and discussion

4.4.1 Dopant solubility

Dopant solubility is determined by the dissolution free energy. For either A-site and B-site, the dissolution process starts from binary dopant oxides, with either HfO_2 or BaO dissolved into pure BHO matrix. By doing that, it creates 2 dopant ions in the lattice, together with an oxygen vacancy to maintain charge neutrality. The reaction equations and dissolution energies are shown below:

$$For\ A-site: 2Ba_{Ba}^{\times} + O_O^{\times} + A_2O(s) + 2HfO_2(s) \rightarrow 2A'_{Ba} + V_O^{\cdot\cdot} + 2BaHfO_3(s)$$

$$\Delta_{diss}G = 2\Delta_f G_{A'_{Ba}} + \Delta_f G_{V_O^{\cdot\cdot}}$$

$$where\ \Delta_f G_{A'_{Ba}} = E_{A'_{Ba}} - E_{perfect} + \mu_{BaHfO_3} - \mu_{HfO_2} - \frac{1}{2}\mu_{A_2O} - \frac{1}{4}\mu_{O_2} - (\varepsilon_f + \Delta\varepsilon)$$

$$and\ \Delta_f G_{V_O^{\cdot\cdot}} = E_{V_O^{\cdot\cdot}} - E_{perfect} + \frac{1}{2}\mu_{O_2} + 2(\varepsilon_f + \Delta\varepsilon)$$

$$For\ B-site: 2Hf_{Hf}^{\times} + O_O^{\times} + B_2O_3(s) + 2BaO(s) \rightarrow 2B'_{Hf} + V_O^{\cdot\cdot} + 2BaHfO_3(s)$$

$$\Delta_{diss}G = 2\Delta_f G_{B'_{Hf}} + \Delta_f G_{V_O^{\cdot\cdot}}$$

$$where\ \Delta_f G_{B'_{Hf}} = E_{B'_{Hf}} - E_{perfect} + \mu_{BaHfO_3} - \mu_{BaO} - \frac{1}{2}\mu_{B_2O_3} - \frac{1}{4}\mu_{O_2} - (\varepsilon_f + \Delta\varepsilon)$$

$$and\ \Delta_f G_{V_O^{\cdot\cdot}} = E_{V_O^{\cdot\cdot}} - E_{perfect} + \frac{1}{2}\mu_{O_2} + 2(\varepsilon_f + \Delta\varepsilon)$$

It is assumed that the finite-size correction for charged-defect before and after dissolution is canceled. The obtained dissolution energy $\Delta_{diss}G$ is shown in Figure 7. At 0K, Rb and K have negative energy values. The slope of the Gibbs energy curve is essentially $-\Delta_{diss}S$, i.e. the minus dissolution entropy. From Figure 7 it is observed that Rb and Li have negative $\Delta_{diss}S$ above ~500K, while all the rest dopants have positive $\Delta_{diss}S$. At 1000K, $\Delta_{diss}G$ has the order of $K < Lu < Y < Sc < Cs < In < Rb < Gd < Ga < Na < Al < La < Li$. It is found that too large or too small dopant ions are difficult to get dissolved in the BHO lattice.

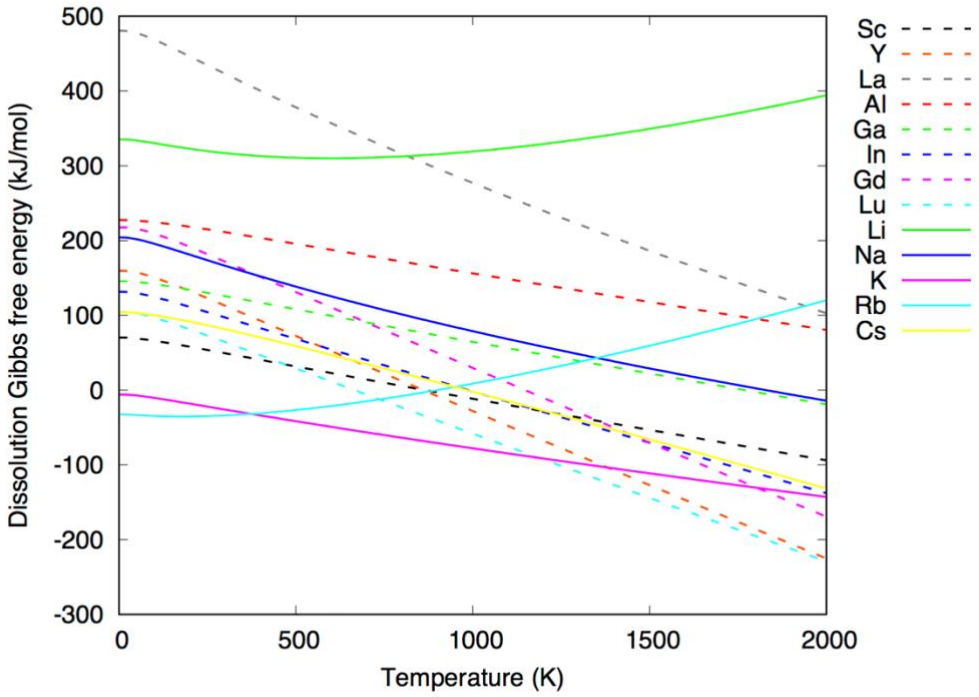

Figure 7 Dissolution Gibbs free energy in kJ/mol for the dissolution reaction w.r.t a temperature range of 0 to 2000 K. A-site and B-site dopants are represented by solid and dashed lines.

Concentrations of dopants are determined by the law of mass action, with $\Delta_{diss}G$ as thermodynamic input. Shown in Figure 8, solubilities of most dopants increase w.r.t increasing temperature, except the case of Rb. Li has a rather low solubility below 1%, and is unable to be captured in this plot. K, on the other hand, demonstrates a steady 100% solubility, due to its negative $\Delta_{diss}G$ over the whole temperature range. A typical value of dopant concentration in experiments is ~20%. Therefore, by looking at 1000K, dopants with solubilities above 20% include K, Lu, Y, Sc, Cs, In, Rb and Gd, and are recommended

as soluble dopants in the BHO matrix. Solubility of Gd drops to 10% as temperature drops to 800K, solubility of Cs, In and Y drops to 10% as temperature drops to 600K.

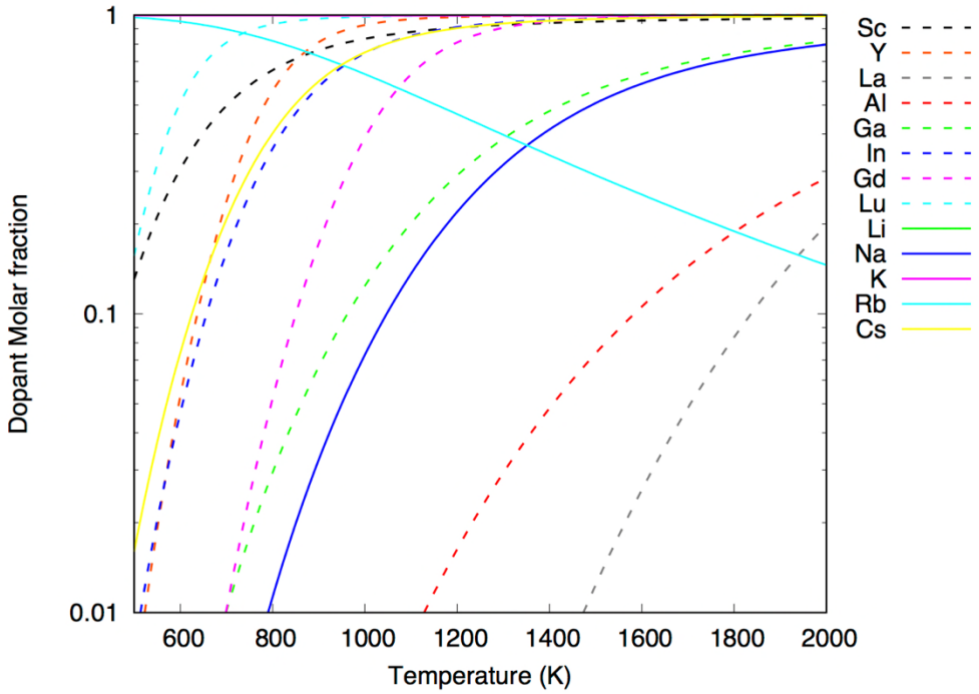

Figure 8 Dopant molar fraction for the dissolution reaction w.r.t temperature range 500~2000K. A-site and B-site dopants are represented by solid and dashed lines. K is always 1 and coincides with the top-axis, Li is way below 0.01 and not captured in this plot.

4.4.2 Proton concentration

Firstly, the hydration expansion and enthalpy at 0K are evaluated. Chemical expansion (CE) upon hydration is plotted against Shannon's ionic radius (R_{ion}) shown in Figure 9. There is an obvious linear correlation between CE and R_{ion}, indicating an intuitive relation between dopant's size and its effect on host lattice's softness. It is believed that

larger dopants make the host lattice softer. The linear relation holds perfectly among A-site dopants, i.e., Li, Na, K, Rb, Cs, but has a few exceptions in B-site ones, e.g., In, Y, Gd. The exceptions could be due to the covalent feature of dopant-oxygen bonds.

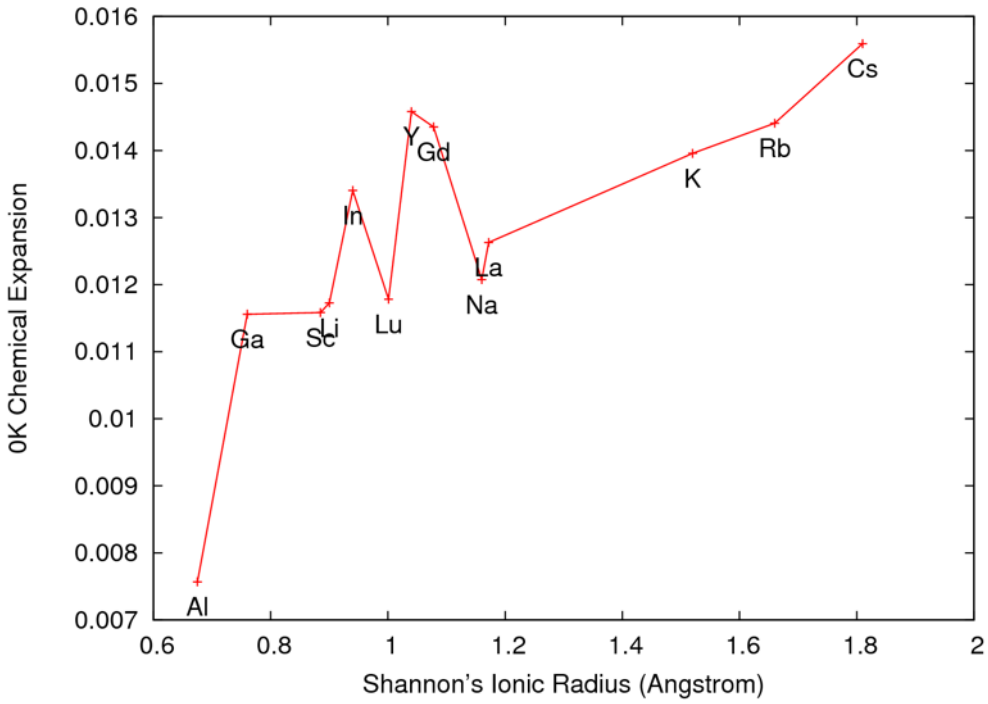

Figure 9 Chemical expansion at 0K upon hydration for A-site and B-site doped BHO w.r.t Shannon's Ionic Radius (Å) of the dopants. A-site dopants: Li, Na, K, Rb, Cs; B-site dopants: Al, Ga, In, Sc, Y, La, Gd, Lu.

Hydration enthalpy at 0K provides the first order of estimation on proton concentration. An obvious linear trend is again obtained for A-site dopants. It indicates that a small dopant on A-site contributes to a large negative hydration enthalpy, which promotes the proton concentration. Similar to the trend in CE, B-site dopants show scattered data points. Although the smallest dopant Al gives the most negative hydration enthalpy, consistent with the conclusion we draw among A-site dopants, the largest dopant La also demonstrate a high value among B-site dopants. Interestingly, outliers in the CE plot, e.g.,

In, Y, turn out to give exceedingly high enthalpy values. It is worth mentioning that comparing with the benchmark line of the pure BHO, hydration enthalpies of all A-site dopants are lower (or more negative), and *vice versa* for most of the B-site dopants. It is thus recommended to utilize A-site dopants to promote hydration processes, comparing with B-site ones.

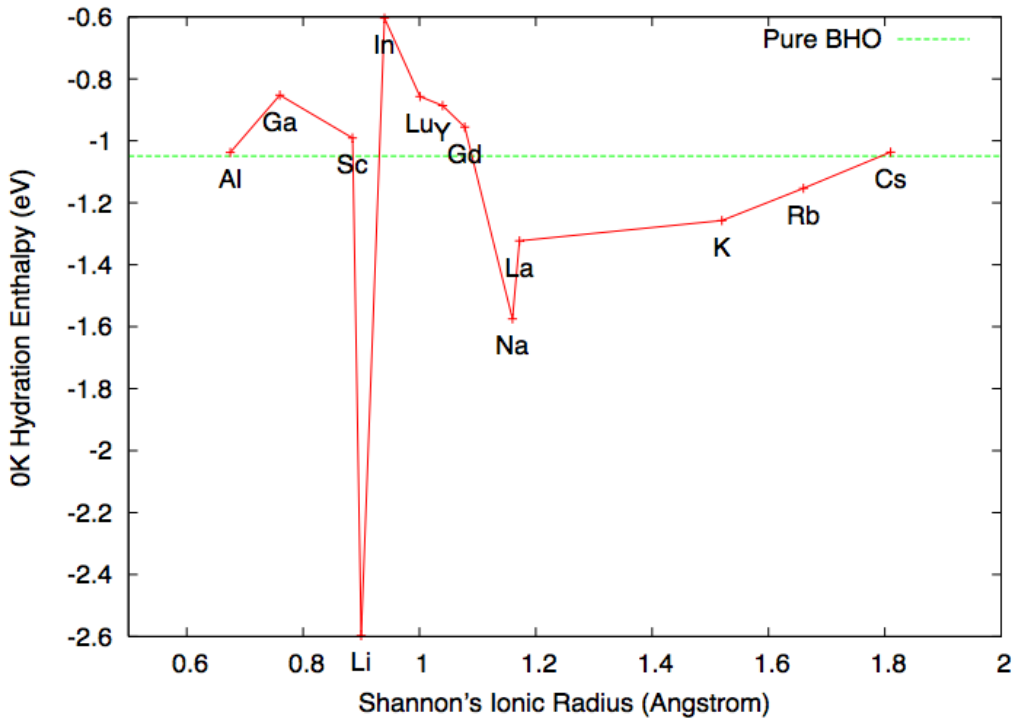

Figure 10 Hydration enthalpy (eV) at 0K for A-site and B-site doped BHO w.r.t dopants Shannon's Ionic Radius (Å). A-site dopants: Li, Na, K, Rb, Cs; B-site dopants: Al, Ga, In, Sc, Y, La, Gd, Lu. The horizontal green dotted line denotes the value in pure BHO.

Starting from the baseline of 0K hydration enthalpy, the finite-temperature vibrational energy is calculated to obtain the hydration free energy for each dopant. Phonon spectrums for the pure BHO, a vacancy in BHO, and a proton in BHO are shown below in Figure 11. Three acoustic modes starting from Γ-point disperse flatly. When a vacancy and

a proton are introduced, imaginary phono modes start to emerge at R and M points, indicating a dynamic instability or a lower-symmetry structure induced by defects. A proton has three featured vibrational modes, with one O-H stretching mode giving the highest frequency above 100 THz, and two softer O-H swaging modes giving frequencies ~20 THz.

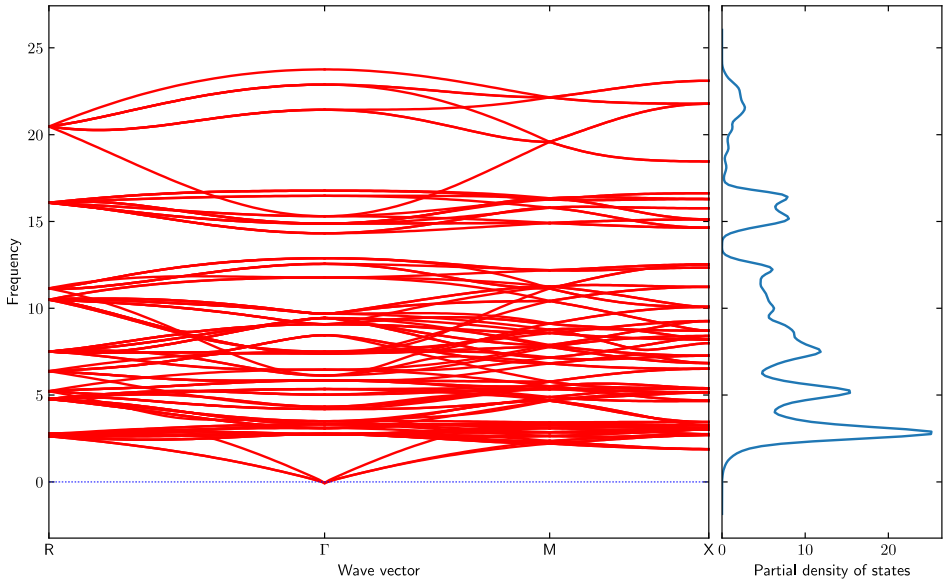

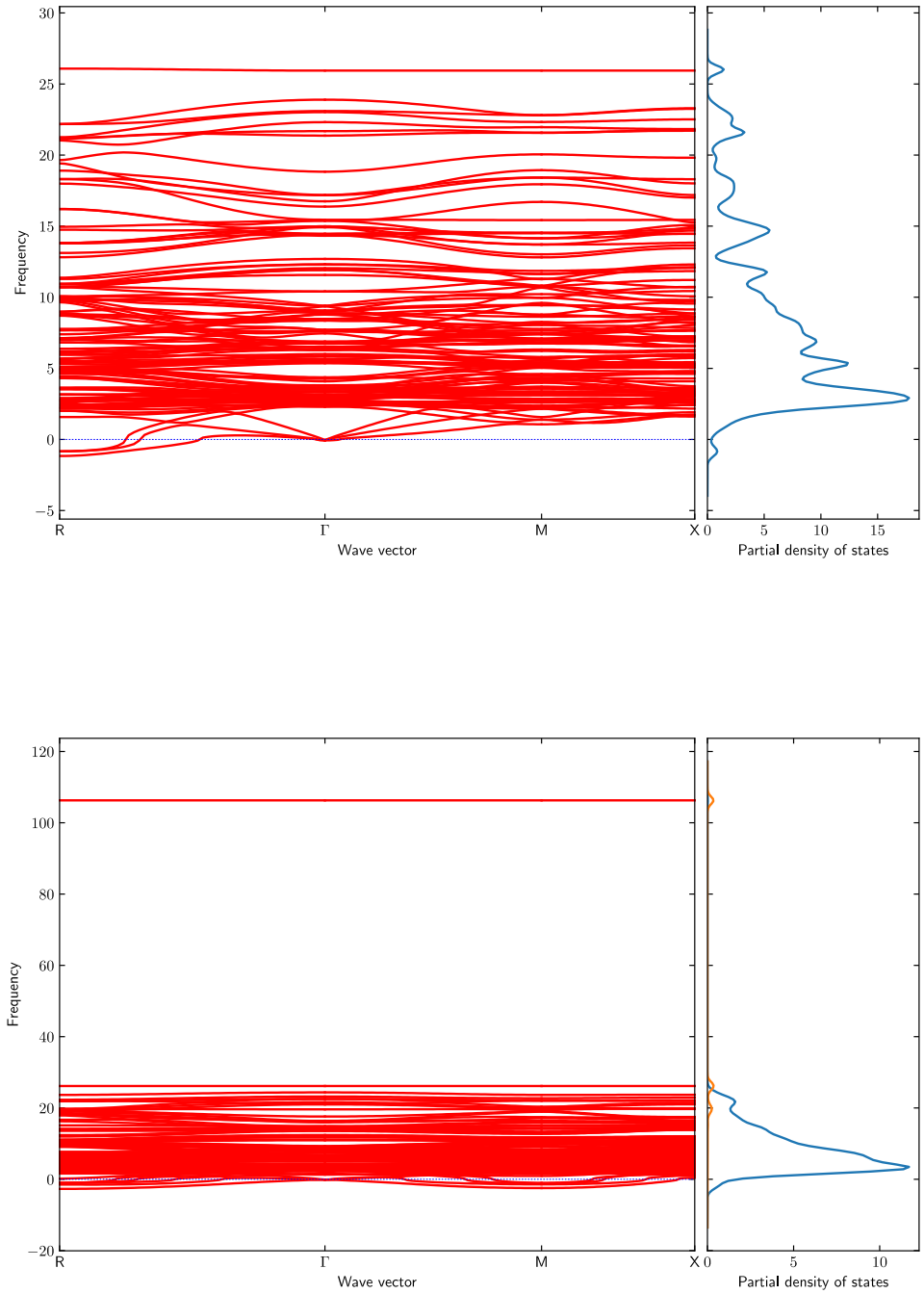

Figure 11 Phonon spectrum (in THz) along R − Γ − M − X with the density of states (DOS) for the pristine BHO, a Va in BHO, and a proton in BHO. Blue and orange lines in DOS represent modes of the BHO lattice and the proton.

Hydration entropy is represented by the slope of the Gibbs free energy curve w.r.t temperature, and is crucial for finite temperature hydration properties. Therefore, it is necessary to accurately evaluate the entropy component. From Figure 12, it is found that pure BHO has a slightly decreasing entropy approaching to -120 J/mol/K. Among the A-site dopants, Li, Rb and Cs have higher hydration entropies ~-50 J/mol/K than pure BHO, possibly due to higher proton vibration frequencies comparing with the ones in pure BHO. Na and K, on the other hand, have lower entropy values. Especially for Na, the entropy value is extremely low, i.e. ~-240 J/mol/K. At 1000 K, hydration entropy for A-site dopants has the order of：

$$Na < K < BHO < Li < Rb < Cs$$

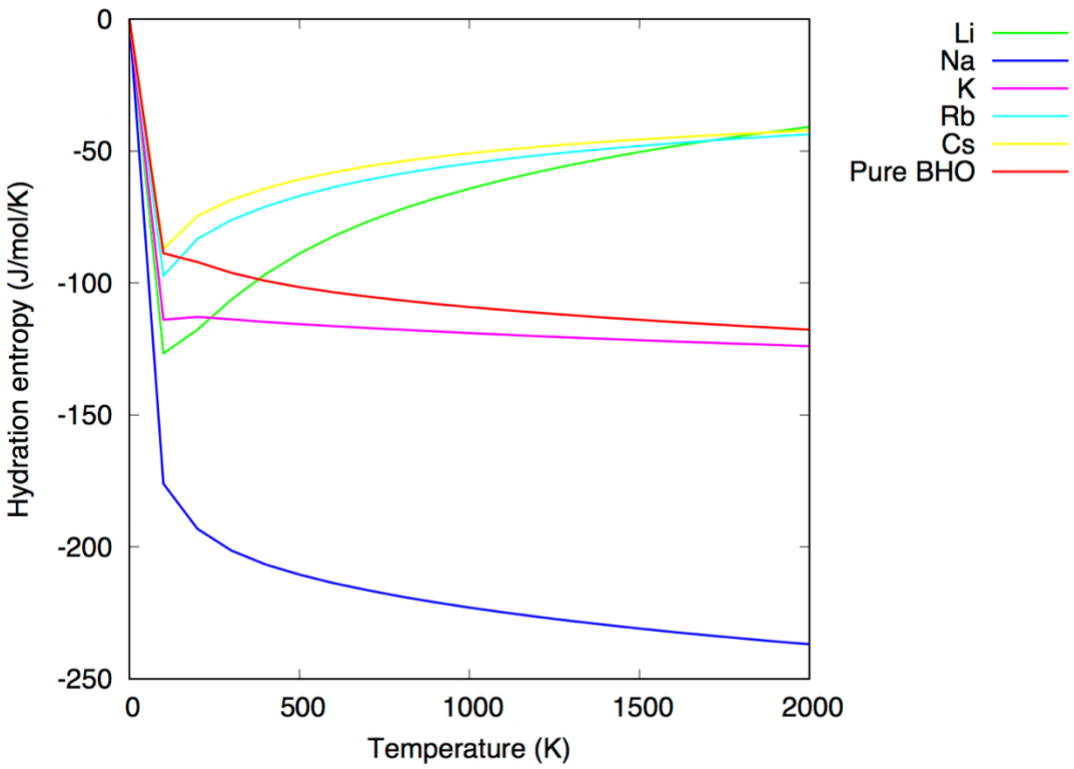

Figure 12 Hydration entropy of A-site doped BHO w.r.t temperature ranging from 0 to 2000 K. Pure BHO curve is plotted in red for the benchmark.

For B-site dopants, hydration entropy is plotted in Figure 13. Interestingly, the entropy values for all B-site dopants are lower than the BHO benchmark line. Especially for Y and La, the entropy values are as low as ~-300 J/mol/K. At 1000 K, hydration entropy for B-site dopants has the order of:

$$Y < La < In < Lu < Gd < Sc < Ga < BHO$$

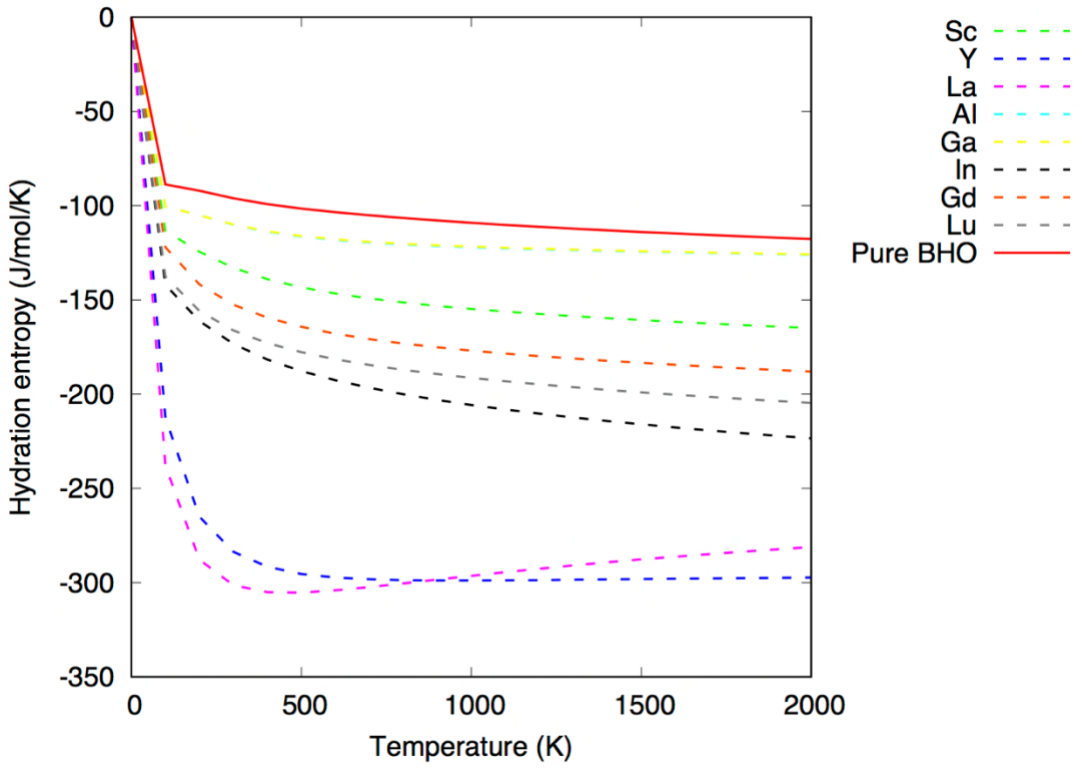

Figure 13 Hydration entropy of B-site doped BHO w.r.t temperature ranging from 0 to 2000 K. Pure BHO curve is plotted in red for the benchmark.

Based on the hydration entropy, the slope of hydration Gibbs free energy can be determined. Combining vibrational free energy with 0K DFT electronic hydration energy, the Gibbs free energy of hydration at finite temperature is calculated. In Figure 14, it is observed that energy of Na has a larger slope, going beyond that of pure BHO when temperature increases. This is due to the extremely low hydration entropy of Na. K has a slightly larger slope than the pure BHO. The rest of A-site dopants always have lower energies than that of the pure BHO, due to either a lower electronic or a vibrational hydration energy. At 1000 K, hydration Gibbs free energies of A-site dopants follows the sequence of:

$$Li < Rb < Cs < K < BHO < Na$$

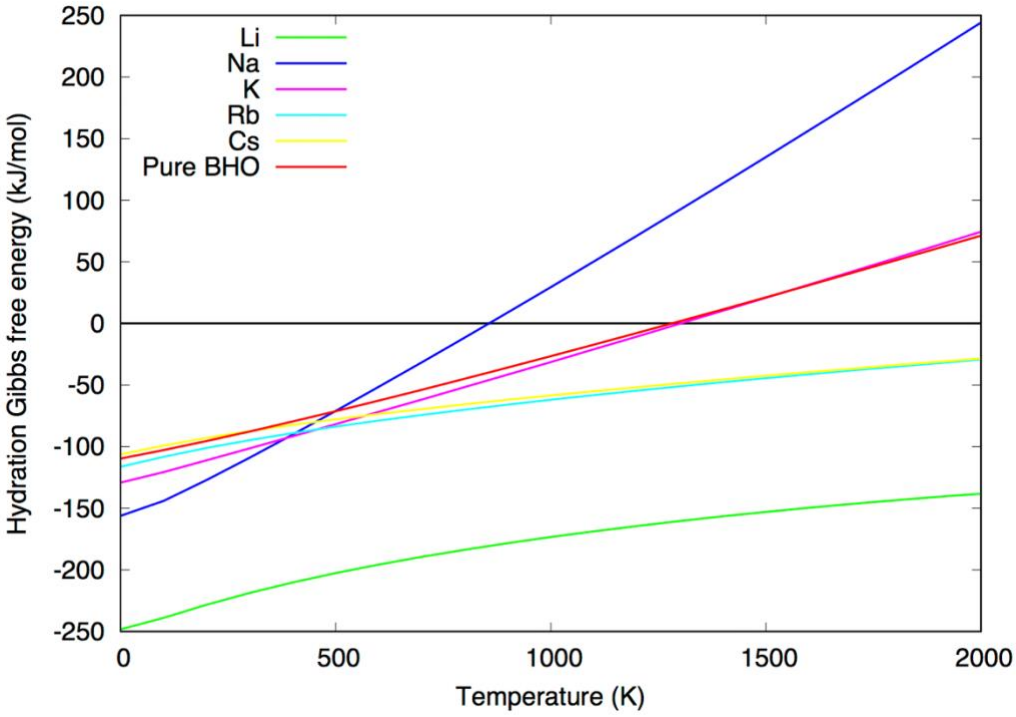

Figure 14 Hydration Gibbs free energy of A-site doped BHO w.r.t temperature ranging from 0 to 2000 K. Pure BHO curve is plotted as well for the benchmark.

Similarly, for B-site dopants (Figure 15), the larger slopes of all dopants w.r.t that of BHO is due to lower hydration entropies w.r.t pure BHO. The crossing points at 0 energy black line take place at low temperatures for La and Y, due to their extremely low hydration entropy. Other than that, the rest of B-site dopants show very consistent slopes in free energy curves. At 1000 K, hydration Gibbs free energy of B-site dopants follows the sequence of:

$$BHO < Al < Ga < Sc < Gd < Lu < In < La < Y$$

It is necessary to mention that hydration energy is calculated from the most stable configuration before and after hydration. For example, the proton in Y-doped BHO cell is most stable at 2NN site than 1NN site w.r.t Y; the vacancy, however, is most stable at

1NN site than 2NN site w.r.t Y. Therefore, the proton at 2NN and the vacancy at 1NN site energies are taken for hydration energy calculation.

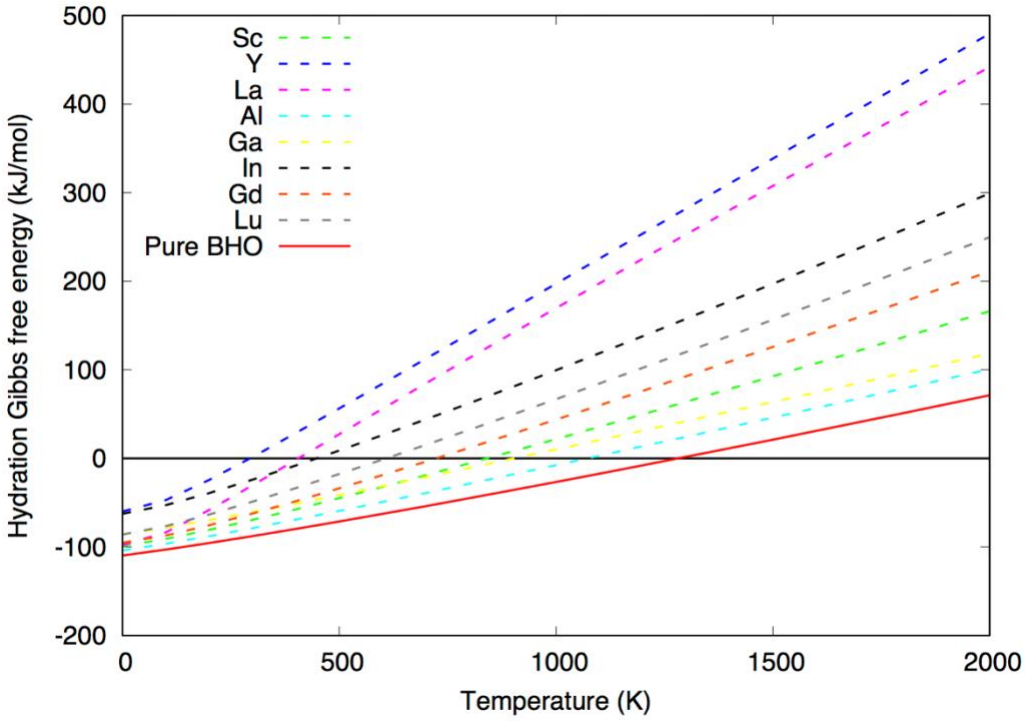

Figure 15 Hydration Gibbs free energy of B-site doped BHO w.r.t temperature ranging from 0 to 2000 K. Pure BHO curve is plotted as well for the benchmark.

As we have the comprehensive Gibbs free energy in the finite temperature, the concentration of charge carriers can be readily calculated from the equation shown below:

$$K = \frac{c[OH_O^{\cdot}]^2}{c[V_O^{\cdot\cdot}]c[O_O^{\times}]p[H_2O]} = exp\left(\frac{\Delta_{Hydr}S}{R}\right)exp\left(-\frac{\Delta_{Hydr}H}{RT}\right)$$

with the constraint of mass and charge balance:

$$c[V_O^{\cdot\cdot}] + c[O_O^{\times}] + c[OH_O^{\cdot}] = 1$$

$$2c[V_O^{\cdot\cdot}] + c[OH_O^{\cdot}] = c[dopant]$$

where $\Delta_{Hydr}H$ and $\Delta_{Hydr}S$ are enthalpy and entropy part of hydration Gibbs free energy. Here an external parameter, i.e. $p[H_2O]$, the partial pressure of water is introduced. Hence concentration is dependent on both temperature and partial pressure of the gas phase water.

Using $p[H_2O] = 0.05$ as an example, $c[OH_O^{\cdot}]$ vs. temperature from 300 to 2000 K are plotted for the A-site doped (Figure 16) and B-site doped BHO (Figure 17). Based on the thermodynamic arguments, proton concentration profiles are obtained, obeying the same sequence as hydration Gibbs free energies do.

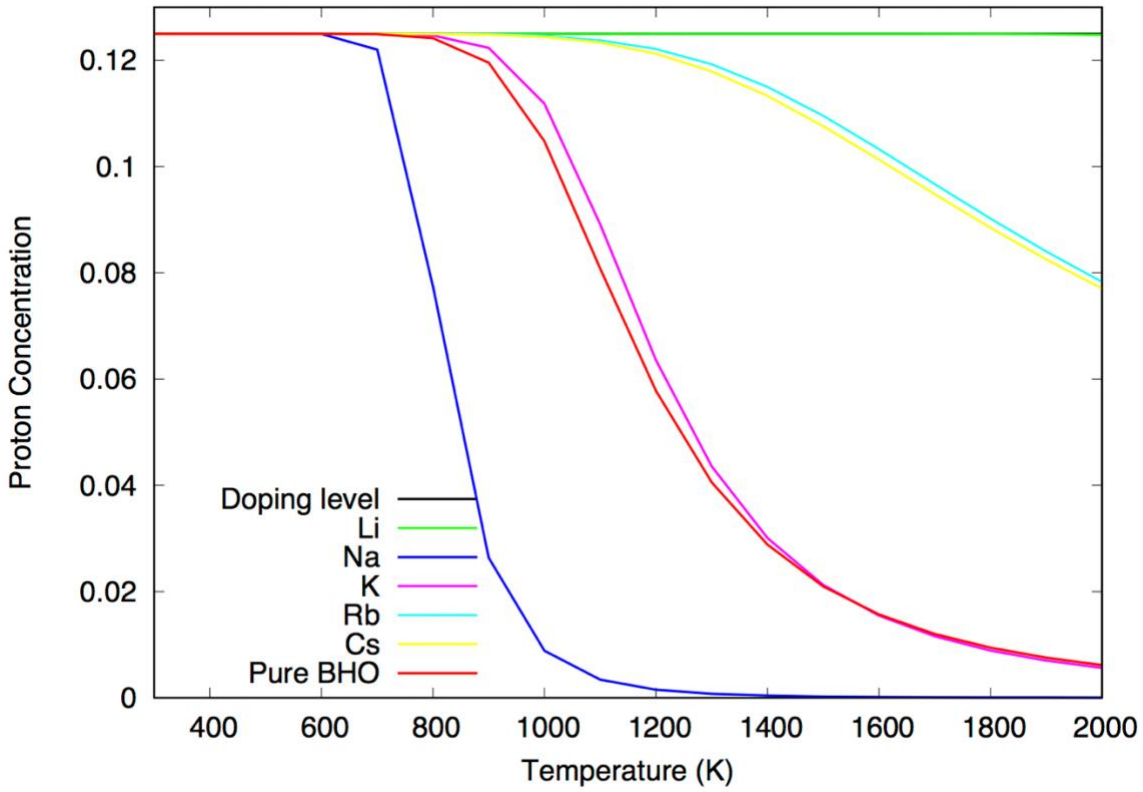

Figure 16 Proton concentration w.r.t temperature at 0.05 water partial pressure, for A-site doped BHO (A=Li, Na, K, Rb, Cs). The doping level is 0.125 based on DFT supercell size.

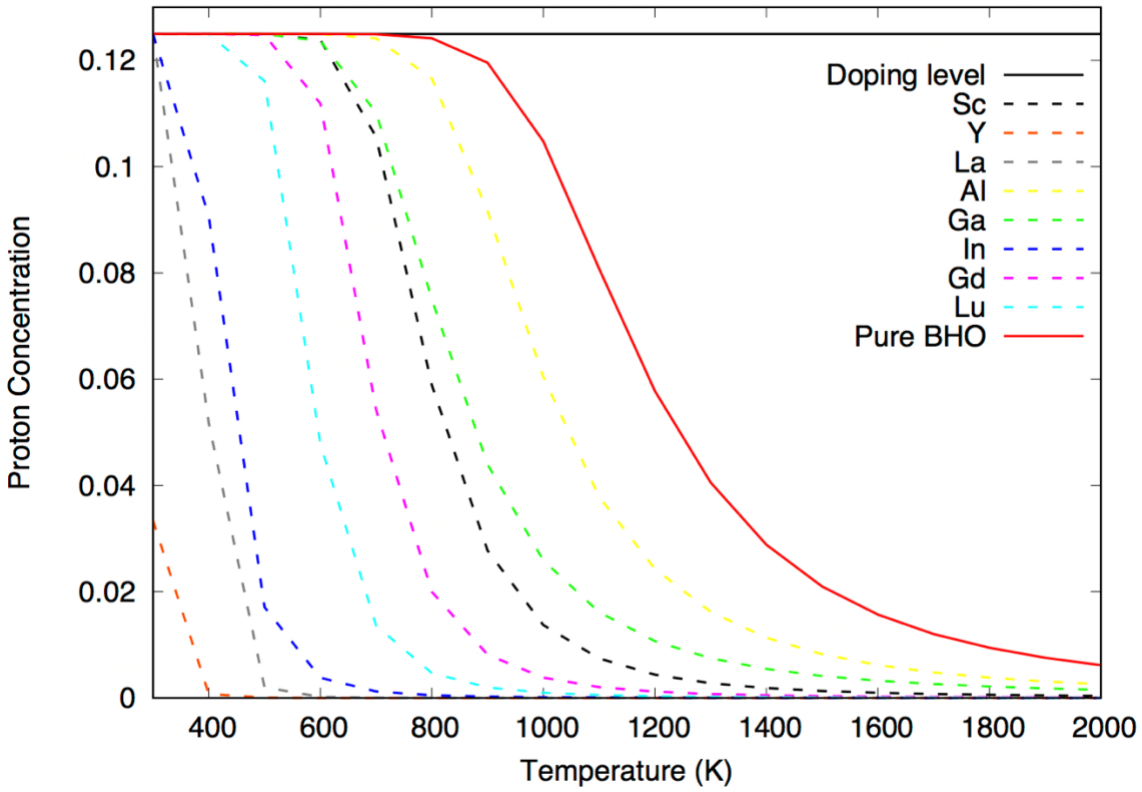

Figure 17 Proton concentration w.r.t temperature at 0.05 water partial pressure, for B-site doped BHO (B=Sc, Y, La, Al, Ga, In, Gd, Lu). The doping level is 0.125 based on DFT supercell size.

4.4.3 Proton mobility

First of all, binding energy between a dopant and a proton, a dopant and an oxygen vacancy are discussed. Binding or trapping can occur at 1NN or 2NN around the dopant, due to a balance between the elastic and the electrostatic interactions, depending on the dopant's ionic radius and electronegativity.

Binding energy is calculated as (use A-site dopant and proton as an example):

$$E_{binding} = E_{(A_{Ba}OH_O)^{\times}} + E_{perfect} - E_{A'_{Ba}} - E_{OH_O^{\cdot}}$$

where $E_{(A_{Ba}OH_O)^{\times}}$ is the energy of dopant-proton associate in the host material with the proton at 1NN or 2NN-site near dopant, $E_{perfect}$ is the energy of pristine host material, $E_{A'_{Ba}}$ and $E_{OH_O^{\cdot}}$ are energies of isolated dopant and proton in the host material. When the zero-point vibrational energy is taken into account, each electronic energy term is then replaced by $E_{elec} + E_{zpe}$, i.e. adding E_{zpe} on top of the original electronic energy term.

The obtained binding energy for dopant-proton and dopant-vacancy in 1NN and 2NN are plotted against dopant's ionic radius, with and without consideration of the zero-point vibrational energy correction, shown in Figure 18 and Figure 19 for A-site dopants and shown in Figure 20 and Figure 21 for B-site dopants. It is found that in A-site dopants, smaller ionic radius Li and Na bind proton strongly at the 1st-nearest-neighbor (1NN) site, i.e. -0.8 and -0.2 eV respectively, while larger dopants like K, Rb and Cs have near-zero binding energies. Li even binds proton at the 2nd-nearest-neighbor (2NN) for about -0.2 eV, while the rest dopants show "anti-trapping" effects at 2NN. In terms of vacancy binding, A-site dopants show negligible or even positive values, albeit in the presence of electrostatic attractions between the two. Na, K, and Rb even show large repulsive behaviors against the vacancy, which is probably due to elastic repulsions. Intuitively, elastic repulsions from A-site dopants are stronger on a 1NN vacancy than a 2NN vacancy. For B-site dopants, binding energy with proton shows a cross-point at Y's ionic radius or between Y and Gd if accounting for the zero-point energy. This indicates a balance between electrostatic and elastic interactions occurring at 1NN and 2NN protons. Y or Gd is the "right" dopant with optimal radius equilibrating the thermal stability of trapped protons at 1NN w.r.t 2NN. Either too large La or too small Al binds proton strongly, due to large

elastic trapping effects. However, this elastic trapping seems to be more effective for 1NN protons near small dopants and 2NN protons near large dopants. Looking back at A-site dopants trapping on protons, it is expected that with virtually larger dopants than Cs, 2NN could become the preferred trapping site, showing similarity with B-site dopants in terms of proton binding. However, this is not the case for vacancies. B-site dopants consistently bind vacancy more strongly at 1NN-site, comparing with A-site dopants would do at 2NN-site. The energy difference between 1NN-site and 2NN-site can be as large as 1 eV for B-site dopants and -0.15 eV for A-site dopants. This indicates vacancy and A-site dopants have stronger elastic repulsions than electrostatic attractions, and *vice versa* for B-site cases. Interestingly, In shows a small "valley" in the "volcano-like" binding energy vs. ionic radius plot. This is due to In's large electronegativity comparing with its two lanthanoid neighbors Sc and Lu, which makes it an electron scavenger and binds with donor-type proton and vacancy tightly.

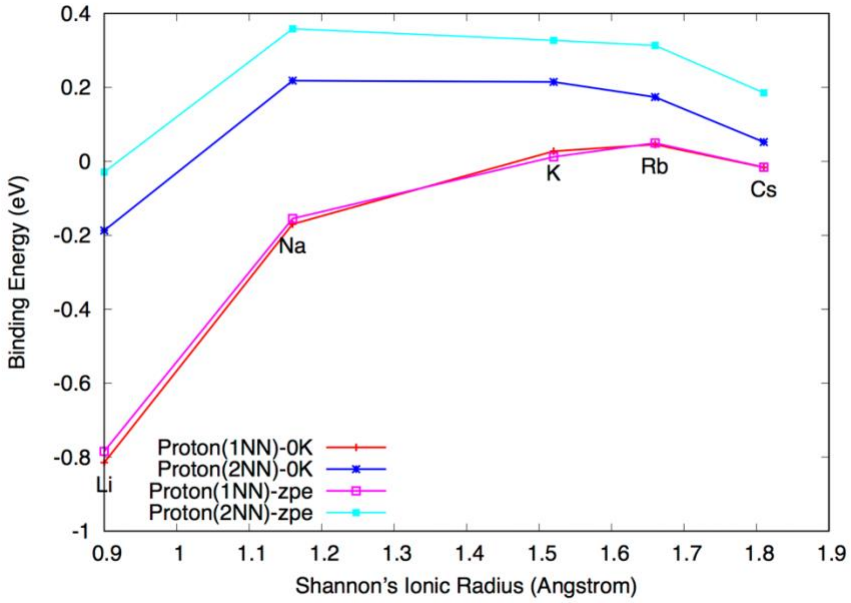

Figure 18 Binding energy (in eV) between various A-site dopants and the proton, at the 1st and 2nd nearest-neighbor (1NN, 2NN) respectively, w.r.t the dopant's ionic radius (Angstrom). Both 0K electronic energy with (-zpe) and without (-0K) zero-point vibrational effects are taken into consideration for comparison.

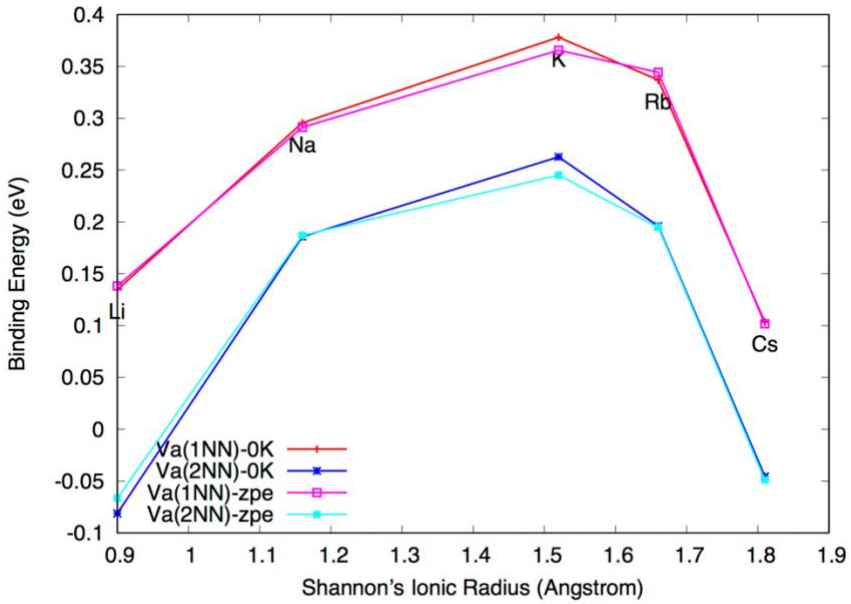

Figure 19 Binding energy (in eV) between various A-site dopants and the vacancy, at the 1st and 2nd nearest-neighbor (1NN, 2NN) respectively, w.r.t the dopant's ionic radius (Angstrom). Both 0K electronic energy with (-zpe) and without (-0K) zero-point vibrational effects are taken into consideration for comparison.

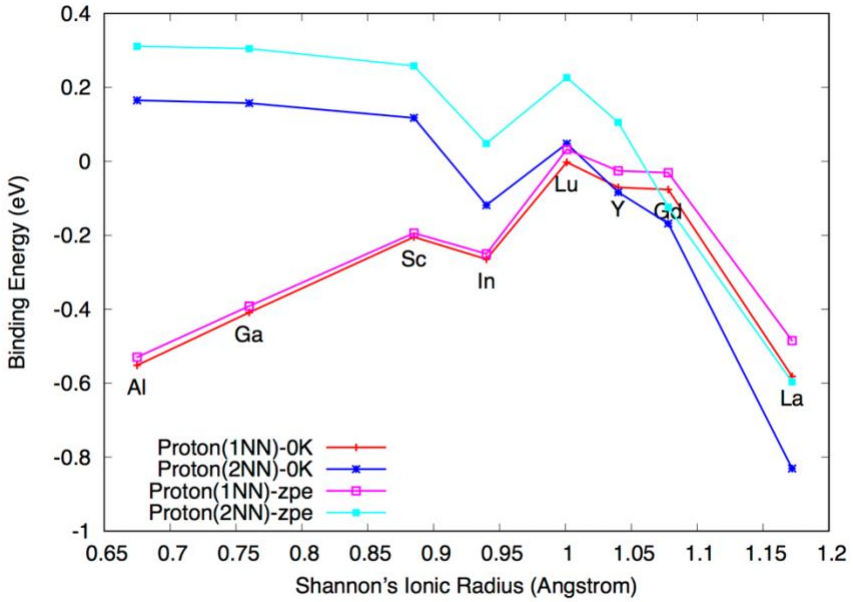

Figure 20 Binding energy (in eV) between various B-site dopants and the proton, at the 1st and 2nd nearest-neighbor (1NN, 2NN) respectively, w.r.t the dopant's ionic radius (Angstrom). Both 0K electronic energy with (-zpe) and without (-0K) zero-point vibrational effects are taken into consideration for comparison.

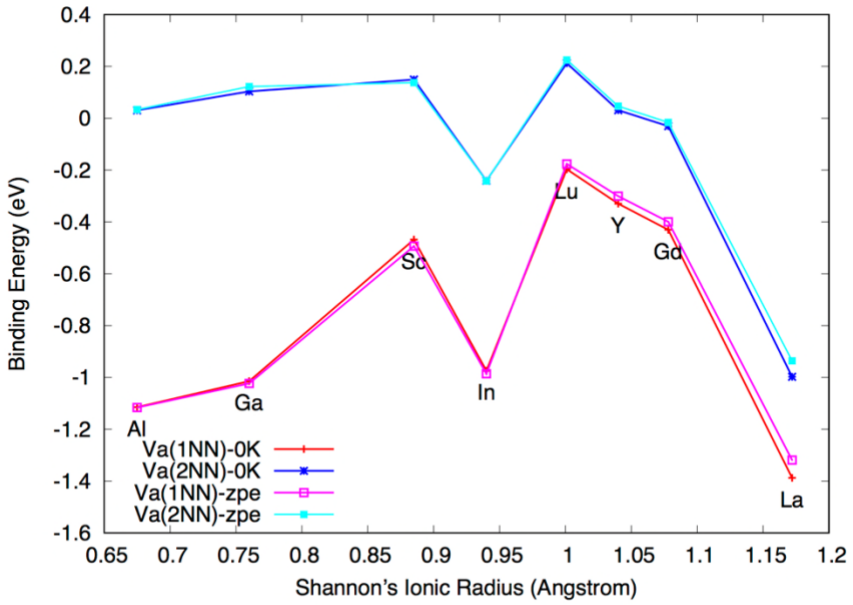

Figure 21 Binding energy (in eV) between various B-site dopants and the vacancy, at the 1st and 2nd nearest-neighbor (1NN, 2NN) respectively, w.r.t the dopant's ionic radius (Angstrom). Both 0K electronic energy with (-zpe) and without (-0K) zero-point vibrational effects are taken into consideration for comparison.

Local structure information of protonated BHO shed some light on the trend of binding energy between dopant and proton. Maximum bond length change between dopant and surrounding oxygen ions $\Delta Max_{M-O}(\text{Å})$, as the variable of binding energy (M the dopant site), is plotted in Figure 22. It is found that the best descriptor for proton binding energy among other structure features (e.g., O-H bond length, M-O bond length, M-O-H bond angle) is $\Delta Max_{M-O}(\text{Å})$.

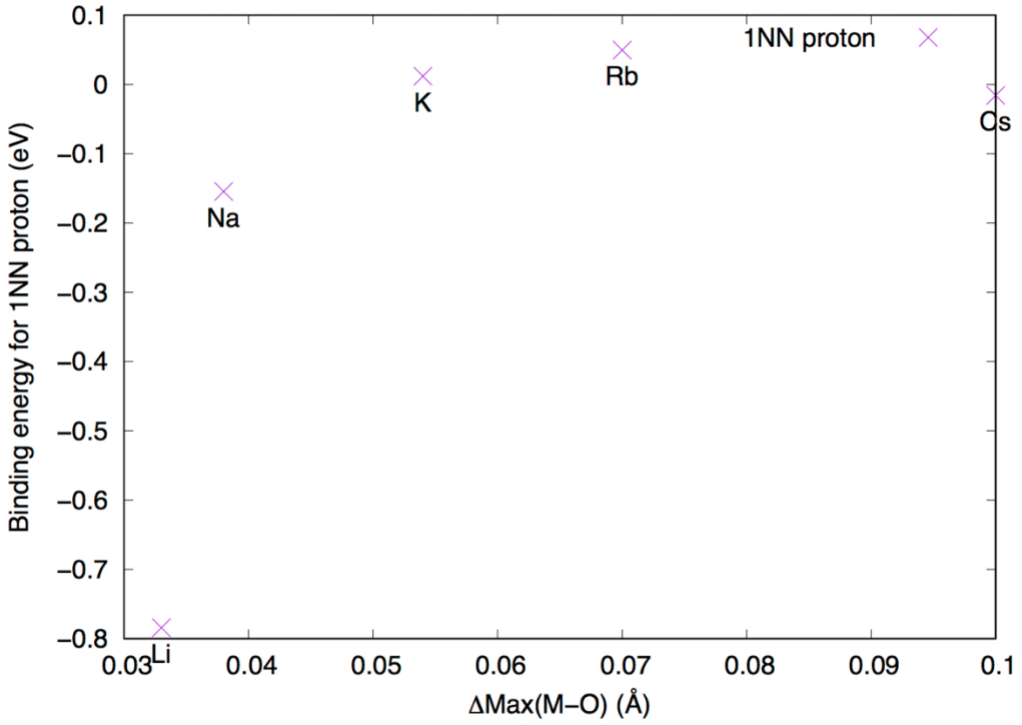
0.1
0
−0.1
−0.2
−0.3
−0.4
−0.5
−0.6
−0.7
−0.8
Binding energy for 1NN proton (eV)
0.03
0.04
0.05
0.06
0.07
0.08
0.09
0.1
ΔMax(M–O) (Å)
1NN proton
Li
Na
K
Rb
Cs

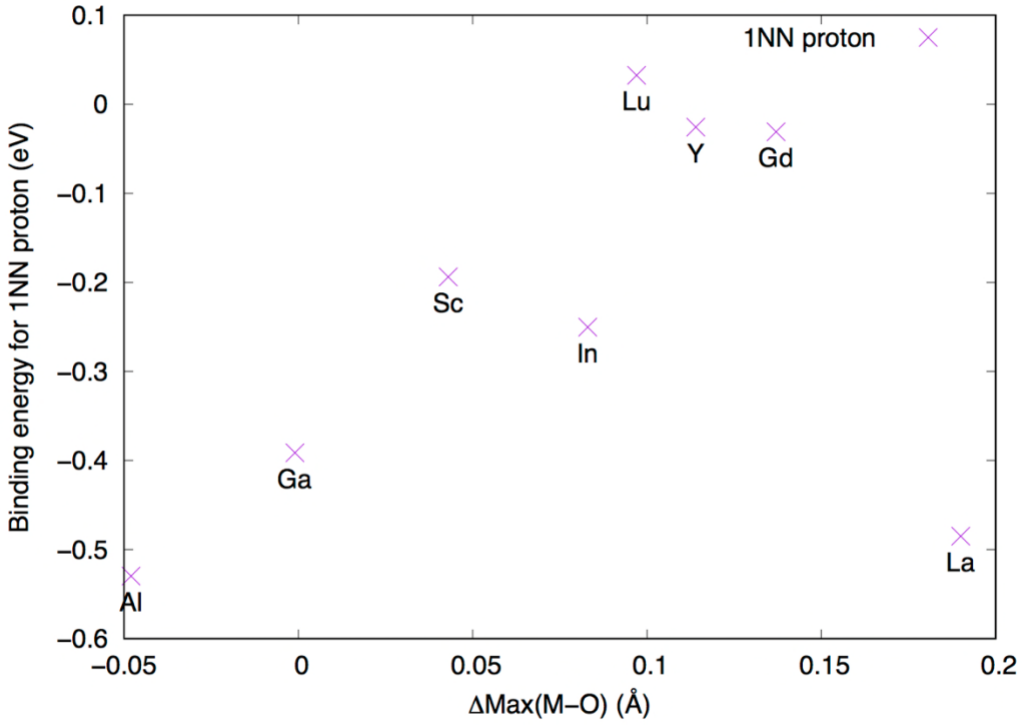

Figure 22 Binding energy (eV) of 1NN proton as a function of local structure descriptor, i.e., maximum bond length change between dopant and surrounding oxygen ions $\Delta Max_{M-O}(\text{Å})$.

4.4.4 Proton conductivity (Analytical estimation)

Let us first consider pristine $BaHfO_3$ with a single proton. As mentioned in CHAPTER 2, rotation and hopping are two jumping modes of the proton in the cubic BHO. Jump rate Γ of the proton can be averaged as:

$$\Gamma_{effective}(T) = \left[\Gamma_{OH\,rot}^{-1}(T) + \Gamma_{H\,hop}^{-1}(T)\right]^{-1}$$

where each jump mode has the Arrhenius relation with its activation energy timed with a pre-factor determined by vibration frequencies at initial and transition states:

$$\Gamma(T) = \frac{\prod \nu_{initial}}{\prod \nu_{TS}^{\ddagger}} \times exp\left(\frac{-E_a}{k_B T}\right)$$

The pre-factors for hydroxyl rotation and proton hopping are 0.89 and 0.43 THz, and the activation energies (without ZPE) for hydroxyl rotation and proton hopping are 0.173 and 0.262 eV. Therefore, $\Gamma_{effective}(T)$ can be calculated in average.

In doped-$BaHfO_3$, the binding energy between dopant and charge carrier proton impedes the proton transport near dopants. This extra energy penalty on proton jumping further contributes to the activation barrier. To simplify the diffusivity estimation, we add this binding energy right on top of the regular activation energy proton overcomes in pristine BHO, so that the jump rate now is:

$$\Gamma(T) = \frac{\prod \nu_{initial}}{\prod \nu_{TS}^{\ddagger}} \times exp\left(\frac{-(E_a - E_{binding})}{k_B T}\right)$$

where the pre-factor for doped BHO is assumed as the same as in pure BHO for simplicity. As negative $E_{binding}$ indicates dopant's "trapping" effect, total activation energy felt by protons is indeed increased by the magnitude of $-E_{binding}$. Positive $E_{binding}$ thus means "anti-trapping" effect *vice versa*.

To initiate the conductivity estimation, we divide the proton species in doped-BHO into two groups: trapped ones and free ones. The generic equation to do the estimation is:

$$\Gamma_{average} = \Gamma_{trapped} c_{trapped} + \Gamma_{free} c_{free}$$

where the only difference between $\Gamma_{trapped}$ and Γ_{free} is the activation energy, i.e., $E_a - E_{binding}$ for trapped ones and E_a for free ones; $c_{trapped}$ and c_{free} are the concentration of protons in trapped and free states. The quotient between $c_{trapped}$ and c_{free} obeys the Boltzmann distribution:

$$\frac{c_{trapped}}{c_{free}} = exp\left(\frac{-E_{binding}}{k_B T}\right)$$

with the mass balance $c_{trapped} + c_{free} = c_{total}$, where c_{total} is determined by hydration energy. With $E_{binding} = 0$, trapped and free protons are equipartitioned in these two states.

Since we have $D = \frac{1}{2} f \sum_k \zeta_k \lambda_k^2 \Gamma_k^d$, we implement the perovskite geometry and OH bond configuration to obtain:

$$D = \frac{1}{2} f (2 \cdot \overline{BO}^2 \cdot \Gamma + 2 \cdot \overline{BO}^2 \cdot \Gamma + 2 \cdot \overline{OH}^2 \cdot \Gamma + 2 \cdot \overline{OH}^2 \cdot \Gamma) = 2f(\overline{BO}^2 + \overline{OH}^2)\Gamma$$

where f is the correlation factor and cannot be obtained *in prior*. Here we simply assume f is 1 for proton's interstitial jumping mechanism.

Finally, conductivity σ can be calculated from D:

$$\sigma = \frac{z^2 e^2 D c}{kT} = \frac{z^2 e^2}{kT} \left(D_{trapped} c_{trapped} + D_{free} c_{free}\right)$$

The proton conductivity of pure-BHO is shown in Figure 23, where the Arrhenius plot shows a linear activation of conductivity w.r.t inverse temperature, with a value of

0.001 to 0.01 S/cm in the temperature window of 127 to 827 ^{o}C. Interestingly, the linear relationship lasts up to 727 ^{o}C. The conductivity drops at this threshold temperature due to limiting hydration percentage. Therefore, w.r.t temperature, there is a "trade-off" between proton mobility and concentration. Low mobility and high concentration of protons occur in low-temperature range, and *vice versa* in high-temperature range.

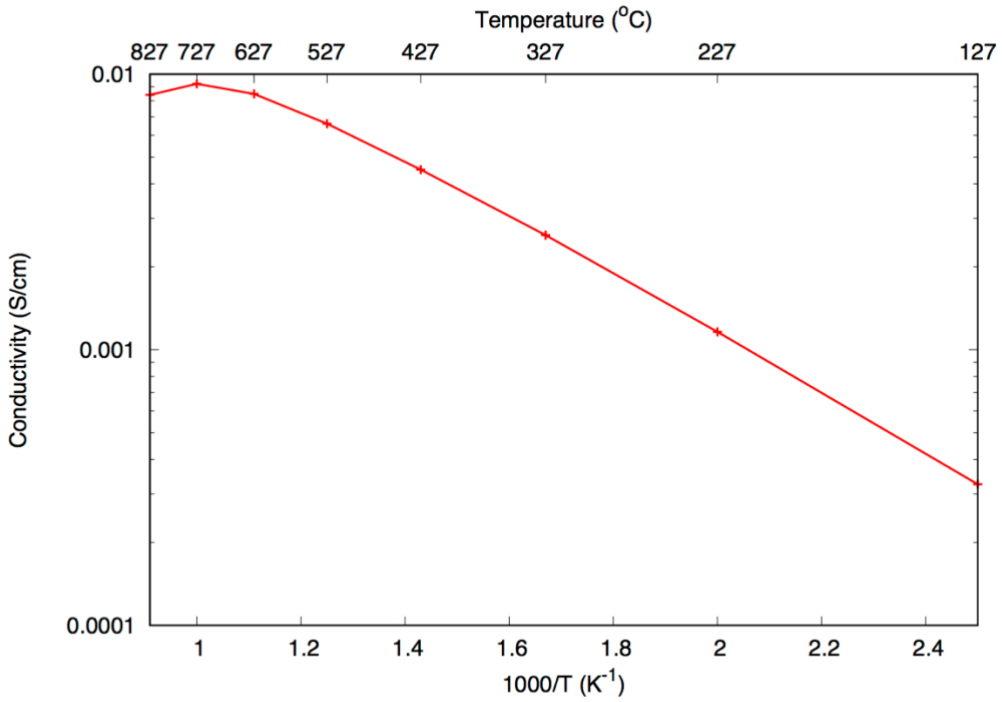

Figure 23 Proton conductivity (S/cm) of pure BHO w.r.t temperature. The temperature range is 127 to 827 ^{o}C (400 to 1100 K). The absolute value of conductivity is around 0.001 to 0.01 S/cm.

With the effects of dopants, both the proton mobility and concentration can change w.r.t the pure BHO benchmark line. The result is shown in Figure 24 for A-site dopants and Figure 25 for B-site dopants. A-site dopants such as Rb, K, Cs have higher

conductivities than pure BHO benchmark line, and *vice versa* for B-site ones. It is observed that for A-site and B-site dopants at 827 ₀C, conductivity has the order of:

$$Rb > K > Cs > BHO > Na > Li$$

$$BHO > Sc > Gd > Lu > Ga > Al > In > Y > La$$

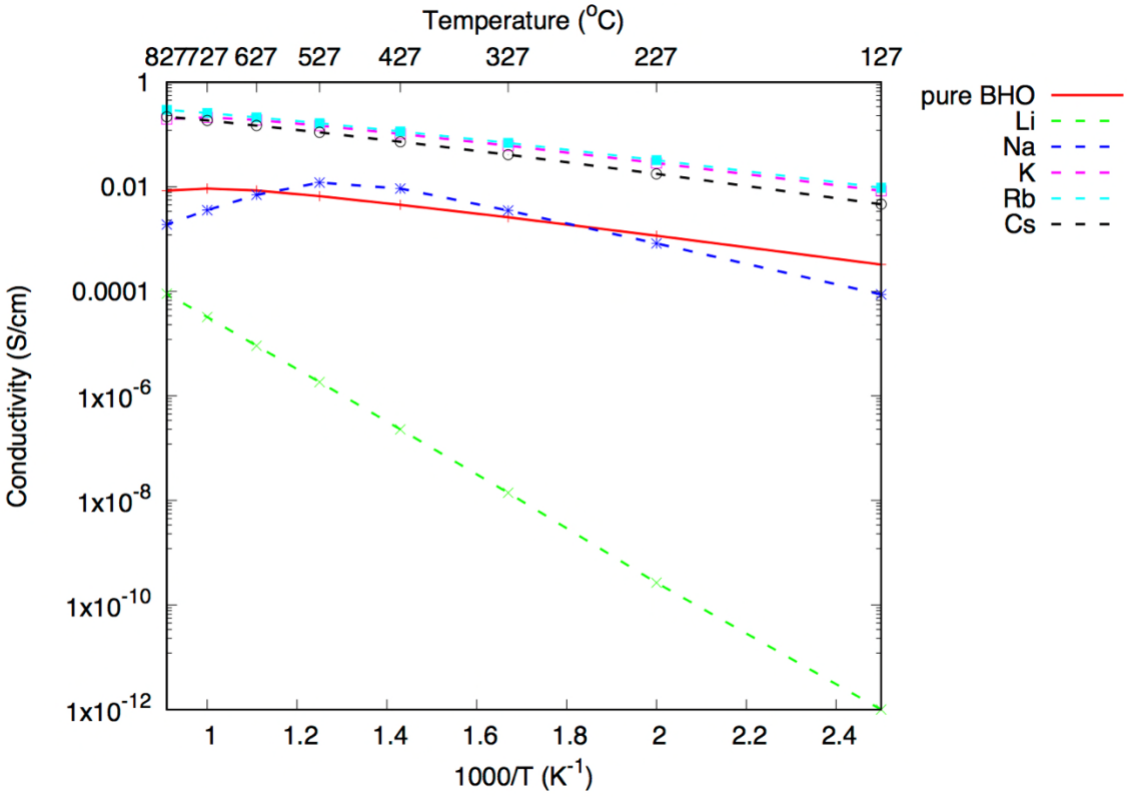

Figure 24 Proton conductivity (S/cm) of A-site doped BHO w.r.t temperature. The temperature range is 127 to 827 ₀C (400 to 1100 K). The absolute values of conductivity for all samples are around 0.001 to 1 S/cm except Li. Conductivity orders in Rb>K>Cs>BHO>Na>Li.

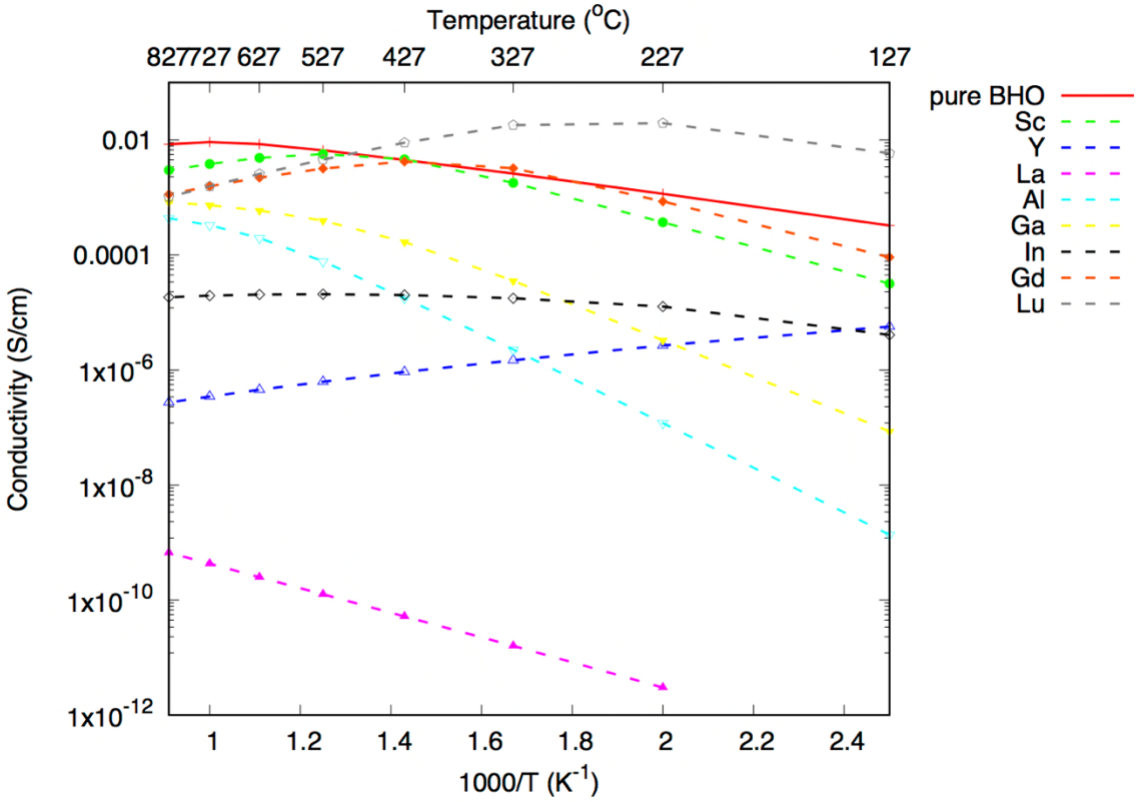

Figure 25 Proton conductivity (S/cm) of B-site doped BHO w.r.t temperature. The temperature range is 127 to 827 °C (400 to 1100 K). The absolute values of conductivity for all samples are around 0.001 to 1 S/cm except Ga, Al, In, Y and La. Conductivity orders in BHO>Sc>Gd>Lu>Ga>Al>In>Y>La.

4.4.5 Chemical stability against CO_2/H_2O: Carbonate/Hydroxide formation

In the calculations of carbonate/hydroxide reaction free energy, initial compositions of reactants are represented by the doped-BHO. Due to this supercell set-up, the reaction equation is slightly different from that of the pure BHO, with excess oxygen gas participating in the reactions:

$$A_1Ba_7Hf_8O_{23} + 7CO_2 + 0.25O_2 \rightarrow 0.5A_2O + 7BaCO_3 + 8HfO_2$$

$$A_1Ba_7Hf_8O_{23} + 7H_2O + 0.25O_2 \rightarrow 0.5A_2O + 7Ba(OH)_2 + 8HfO_2$$

$$Ba_8B_1Hf_7O_{23} + 8CO_2 + 0.25O_2 \rightarrow 0.5B_2O_3 + 8BaCO_3 + 7HfO_2$$

$$Ba_8B_1Hf_7O_{23} + 8H_2O + 0.25O_2 \rightarrow 0.5B_2O_3 + 8Ba(OH)_2 + 7HfO_2$$

Similarly, the equilibrium constant can be written as, e.g., using CO_2 as an example:

$$\mathrm{K} = \frac{1}{p_{CO_2}^{n} p_{O_2}^{0.25}} = \exp\left(-\frac{\Delta G}{RT}\right)$$

where $\Delta G = \Delta E + \Delta G_{vib}$, ΔE is the reaction energy at 0K from electronic energy contribution, and ΔG_{vib} is the vibrational contribution to the reaction energy. For gas molecules, their entropic data are obtained directly from the NIST JANAF table, while the rest of the thermodynamic data are obtained from DFT phonon calculations. Assume the partial pressure of oxygen gas is from the ambient environment, i.e. 0.21. $n = 7$ for A-site doping, 8 for B-site doping. Specifically, we have the Gibbs free energy of gas molecules:

$$\begin{aligned} G(T) &= H_{elec,0K} + G_{vib,rot,tran}(T) \\ &= H_{elec,0K} + H_{vib}(T) + H_{rot}(T) + H_{tran}(T) - T * S_{vib,rot,tran}(T) \\ &= H_{elec,0K} + H_{vib}(T) - T * S_{vib,rot,tran}(T) + E_{rot}(T) + E_{tran}(T) + k_B T \end{aligned}$$

Where $E_{rot}(T) =$

$1.5k_BT\ for\ nonlinear\ molecule, and\ k_BT\ for\ linear\ molecule;\ E_{tran}(T) = 1.5k_BT$

The plot of p_{CO_2} and p_{H_2O} w.r.t T is the so-called Van't Hoff plot where we can locate the critical secondary-phase formation temperature at any arbitrary partial pressure of contaminant gas. The Gibbs free energies of reactions for BHO-based proton conductor with H_2O/CO_2 are shown in Figure 26 and Figure 27. All the Gibbs energy curves w.r.t

temperature have positive slopes, indicating the contamination reaction involves entropy reduction. This is intuitive as gas-phase H_2O/CO_2 is consolidated to corresponding carbonate and hydroxide with degrees of freedom in translation and rotation quenched. H_2O contamination process has less entropy decrease than CO_2 does, which is largely attributed to the entropy difference of these two gas phases. However, reaction energy at 0K is positive for water contamination. Therefore, H_2O contamination is energetically unfavorable across the whole temperature range. In terms of dopant selection for stability, A-site dopants (solid lines) in BHO give higher Gibbs energies of reaction and higher stability at a lower temperature region. However, a cross-point occurs somewhere in the middle, making B-site doped BHO (dashed lines) more stable at a higher temperature region. Unlike H_2O, CO_2 contamination reaction is thermodynamically favorable at low-temperature range up till ~800 K.

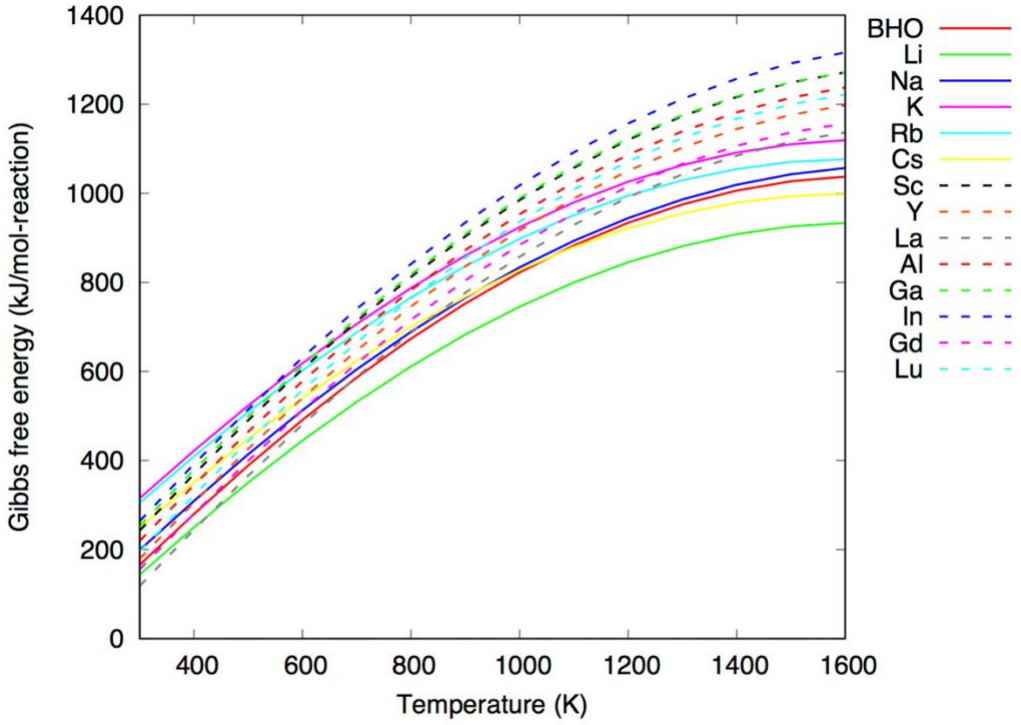

Figure 26 Gibbs free energy of reaction (kJ/mol-reaction) for BHO-based proton conductor and H_2O. Pure BHO is shown in a red solid line. A-site dopants, i.e., Li, Na, K, Rb, Cs and B-site dopants, i.e., Sc, Y, La, Al, Ga, In, Gd, Lu are shown in solid and dashed lines. The Gibbs free energy is per mole reaction.

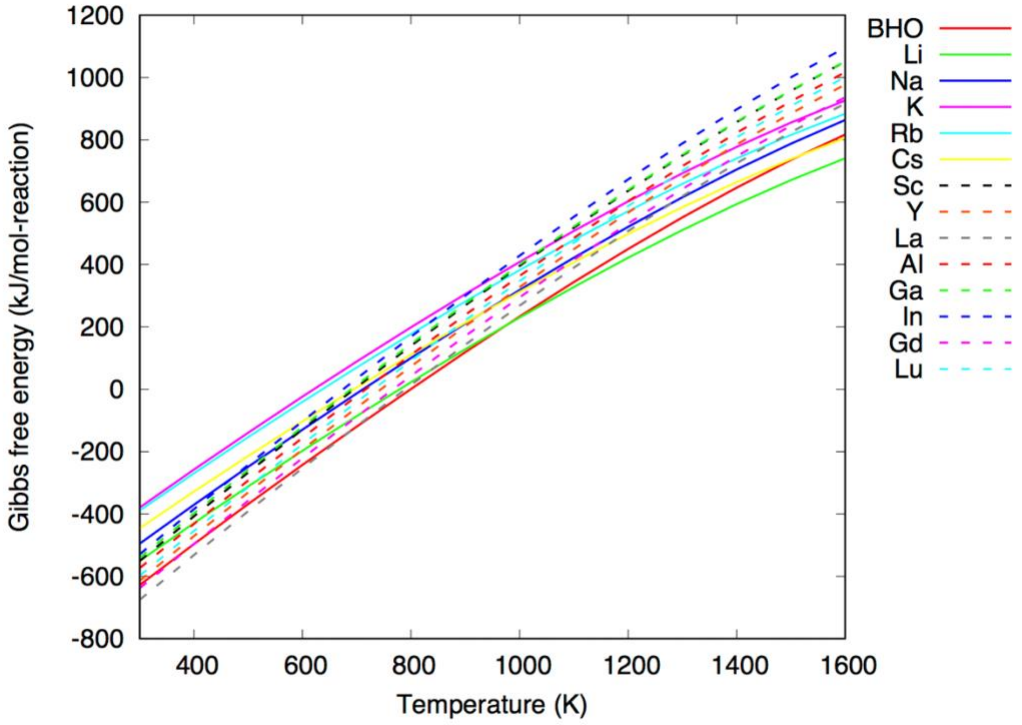

Figure 27 Gibbs free energy of reaction (kJ/mol-reaction) for BHO-based proton conductor and CO_2. Pure BHO is shown in a red solid line. A-site dopants, i.e., Li, Na, K, Rb, Cs and B-site dopants, i.e., Sc, Y, La, Al, Ga, In, Gd, Lu are shown in solid and dashed lines. The Gibbs free energy is per mole reaction.

Van't Hoff plot can be easily derived from the Gibbs energy of reaction shown above, using the law of mass action. Each Van't Hoff plot with the corresponding dopant is essentially a phase diagram with the upper-left and bottom-right regions the contaminated phases and functional perovskite phase regions. The black horizontal line crosses the Van't Hoff curve with the cross-point standing for the "critical temperature", above which the perovskite phase is thermodynamically stable. Therefore, the lower the critical temperature, the larger the stability window for the perovskite. Critical temperatures for H_2O reaction are nonexistent, as H_2O contamination requires extremely

high partial pressure of water. The order of critical temperature for CO_2 reaction at 1 bar is $K < Rb < In < Ga < Sc < Cs < Na < Al < Lu < Y < Gd < Li < La < BHO$. It is observed that A-site doped BHO are in general more stable than B-site ones against CO_2 contamination.

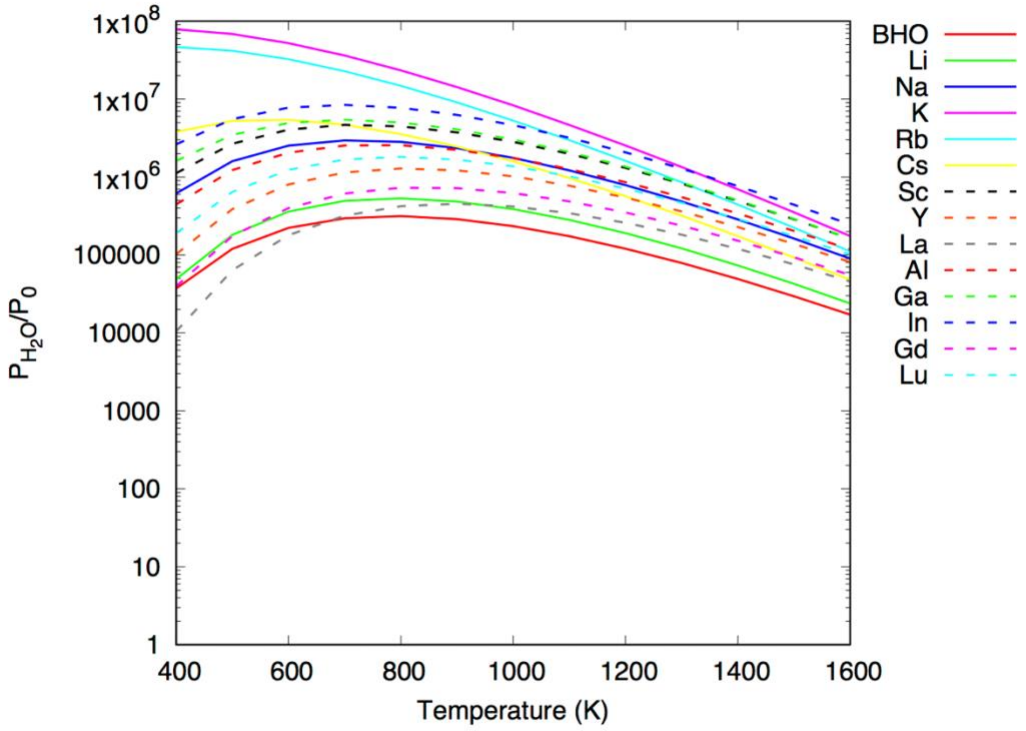

Figure 28 Van't Hoff plot for BHO-based proton conductor and H_2O. Pure BHO is shown in a red solid line. A-site dopants, i.e., Li, Na, K, Rb, Cs and B-site dopants, i.e., Sc, Y, La, Al, Ga, In, Gd, Lu are shown in solid and dashed lines.

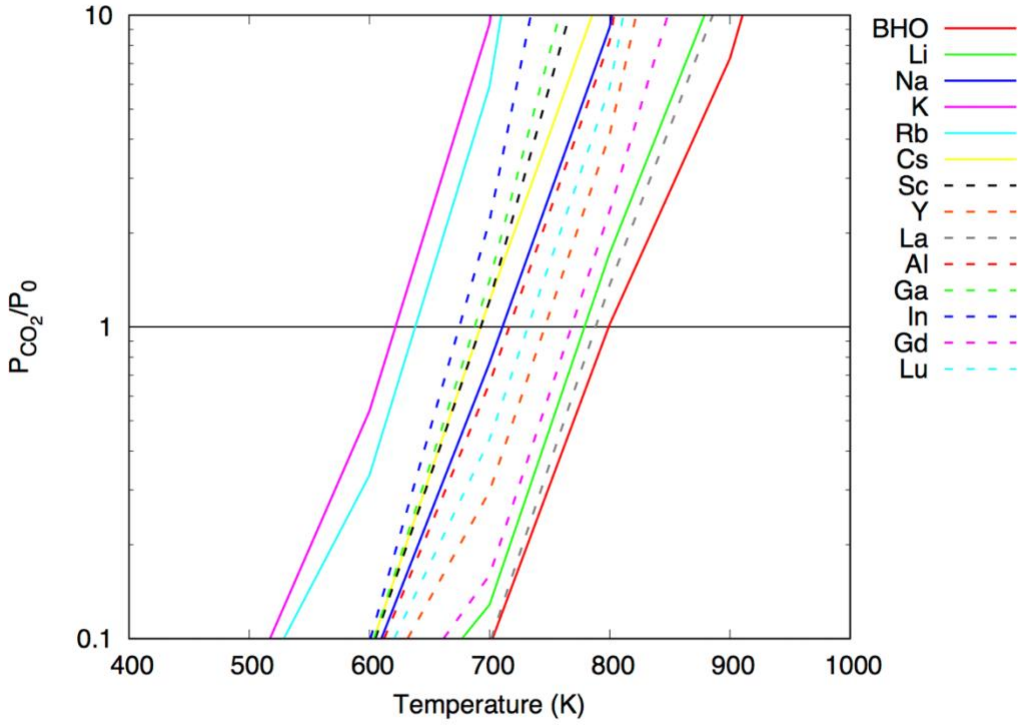

Figure 29 Van't Hoff plot for BHO-based proton conductor and CO_2. Pure BHO is shown in a red solid line. A-site dopants, i.e., Li, Na, K, Rb, Cs and B-site dopants, i.e., Sc, Y, La, Al, Ga, In, Gd, Lu are shown in solid and dashed lines. The black horizontal line crosses with each sample's Van't hoff curve with a cross point the "critical temperature" for phase transformation under 1 bar pressure of CO_2.

4.4.6 Thermodynamic stability via cluster expansion: Defect-Ordering in Ba(Hf,Ce)O_3 solid solution

Making a solid-solution Ba(Hf,Ce)O_3, or BHCO, between $BaHfO_3$ (BHO) and $BaCeO_3$ (BCO) is a common strategy to balance conductivity and stability for proton-conducting electrolyte in PCFCs. The reason is that BHO-based perovskite has higher stability but lower conductivity w.r.t BCO-based perovskite. A compromise is thus

achieved when BHCO with “optimal” Hf:Ce ratio demonstrates both “good enough” stability and conductivity under working conditions.

To understand the mixing behavior between BHO and BCO, we construct the cluster expansion model, together with 3*3*3 135-atom SQS cells across Ce composition. 0K DFT calculated energies (including SQS energies) and CE predicted energies w.r.t BHO and BCO references are shown in Figure 30. It is found that mixing is favored near Ce-rich BHCO, but *vice versa* near Hf-rich BHCO. Mixing energies from SQS supercells also coincide with the formation energies of predicted/fitted structures in the middle. A ground-state structure is predicted ~0.9 Ce composition. It indicates that clustering is highly favorable near the Hf-rich side, as mixing enthalpies of SQS random alloys are larger than formation enthalpies of ordered compounds, and *vice versa* near Ce-rich side.

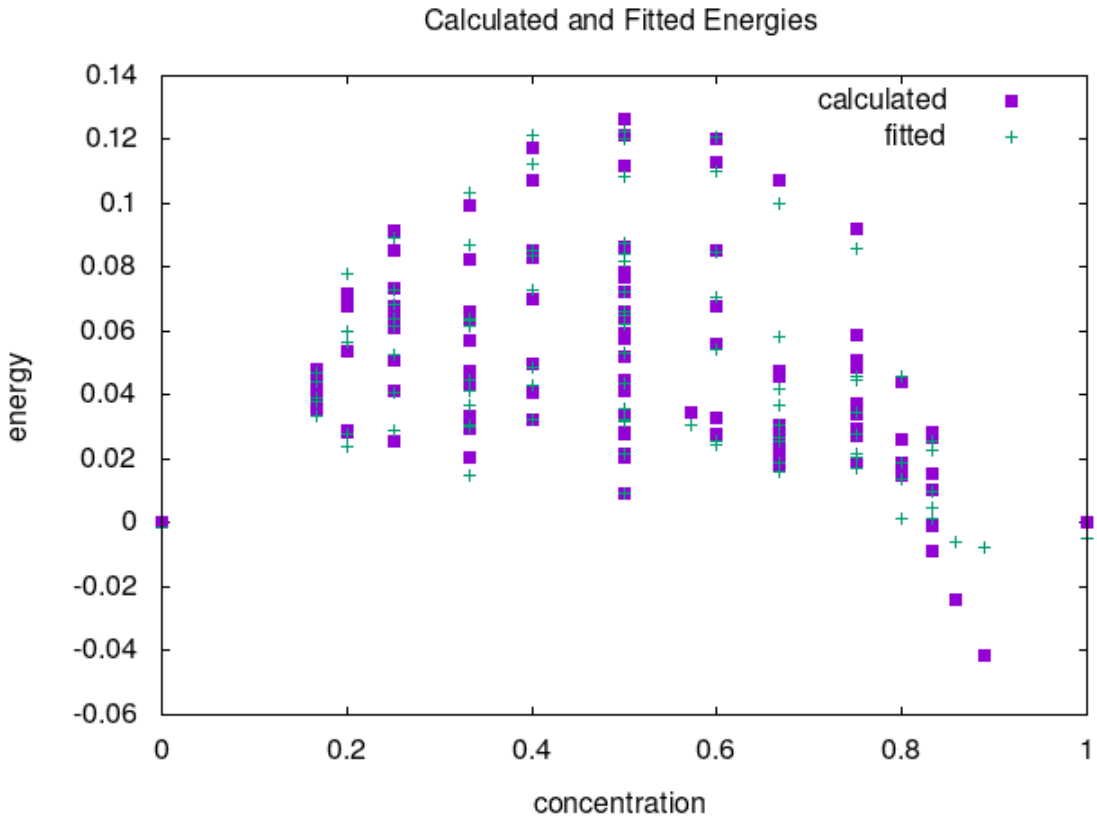
Calculated and Fitted Energies
calculated
fitted
energy
concentration
0.14
0.12
0.1
0.08
0.06
0.04
0.02
0
-0.02
-0.04
-0.06
0
0.2
0.4
0.6
0.8
1

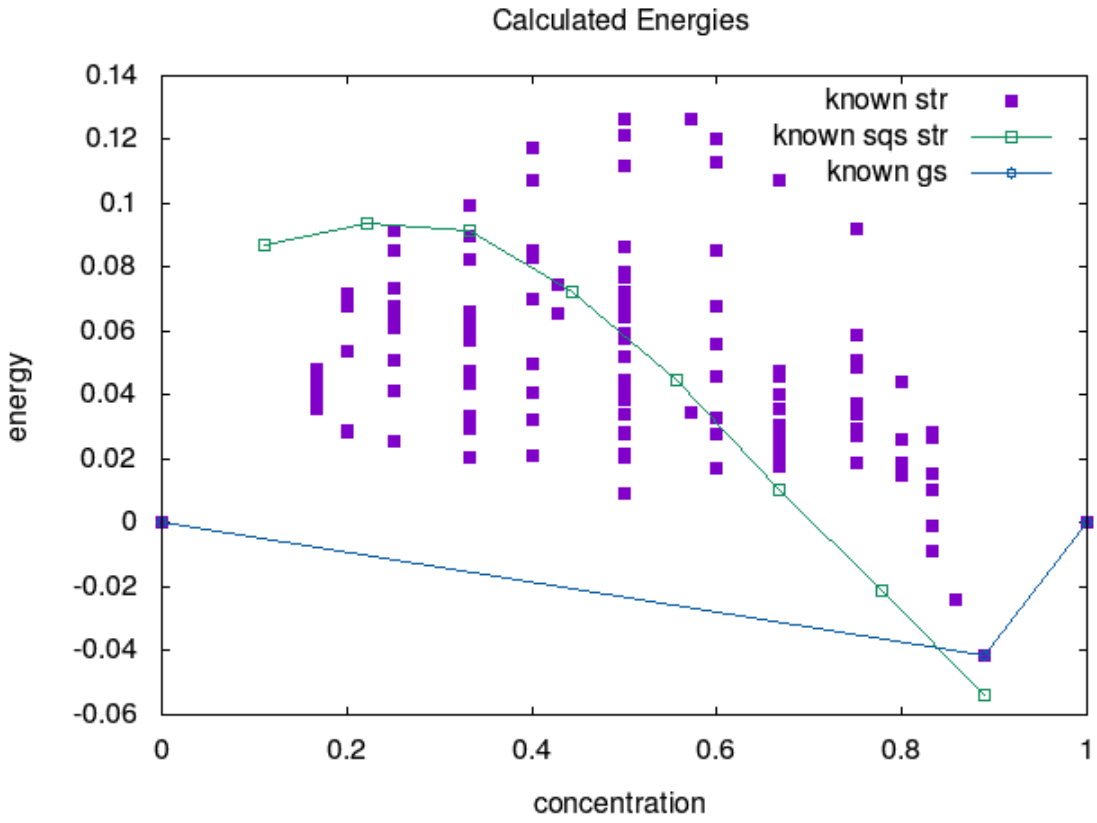

Figure 30 0K energies (in eV/unit formula) of BHCO structures with BHO and BCO energies as references, w.r.t Ce site-composition in BHCO. Formation energies of intermediate compounds calculated from DFT (calculated, known str) and fitted from CE model (fitted) are in solid purple squares and blue crosses. Additionally, mixing energies of SQS (known sqs str) are in hollow green squares connected by the green line. Convex hull of BHCO solid solution is connected by a blue line, with one intermediate ground state (known gs) at ~0.9 Ce composition.

4.4.7 Hydration thermodynamics of doped-BHCO

Similar to we calculate hydration thermodynamics for doped-BHO, we expand the same methodology to 3*3*3 135-atom doped-BHCO SQS cells. The SQS cells have dopant composition as 22.22%, and Ce composition as 70.37% and 55.56% in A-site and B-site dopant scenarios. The SQS supercell samples for A-site and B-site doped BHCO are shown in Figure 31.

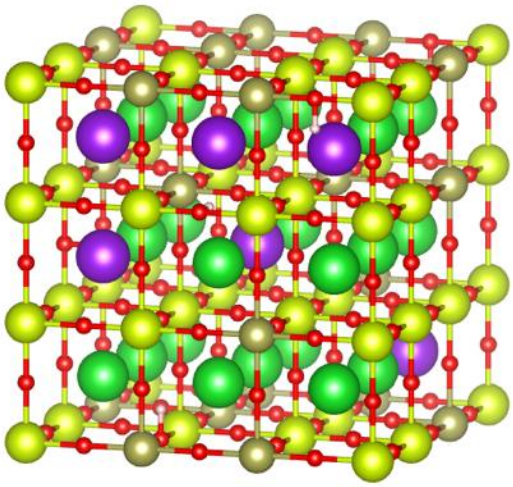

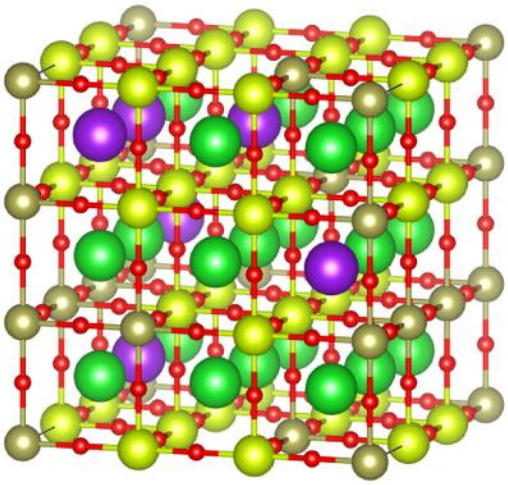

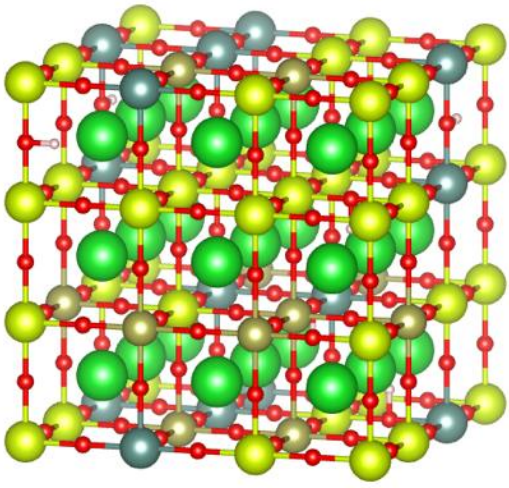

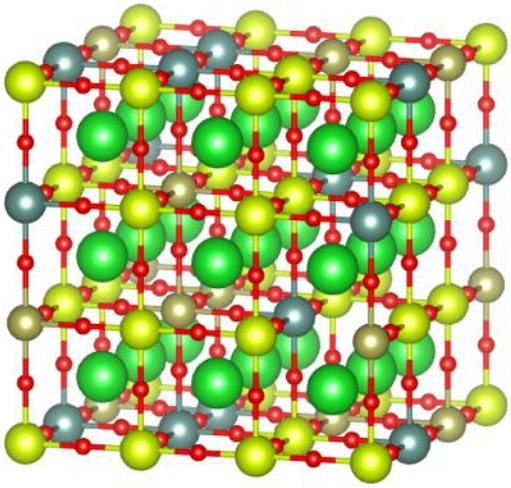

Figure 31 A-site and B-site doped BHCO SQS cells (3*3*3 of primitive perovskite cell). Ba: green; Hf: bronze; Ce: yellow; O: red; H: pink; A-site dopant: purple; B-site dopant: cyan.

Firstly, 0 K hydration enthalpy/entropy is computed following the equation:

$$\Delta_{Hydr}H = H_{6*OH_O^{\cdot}-6*dopant} - H_{3*V_O^{\cdot\cdot}-6*dopant} - 3 * H_{H_2O}$$

$$\Delta_{Hydr}S = S_{6*OH_O^{\cdot}-6*dopant} - S_{3*V_O^{\cdot\cdot}-6*dopant} - 3 * S_{H_2O}$$

where in SQS cells, configurations before and after hydration are all neutral. 6-dopant SQS cells can absorb 3 water molecules at the full hydration.

Shown in Figure 32, 0K hydration enthalpy for 7 dopants (Sc, In, Lu, Y, Gd, K, Cs) are all negative, indicating that hydration takes place automatically at 0K. Nonetheless, A-site dopants K, Cs are still showing excellent hydration capability. Interestingly, in BHCO, B-site dopants Sc and Gd also stand out. Consistent with the prediction in BHO, In, Lu, Y are not as good, either.

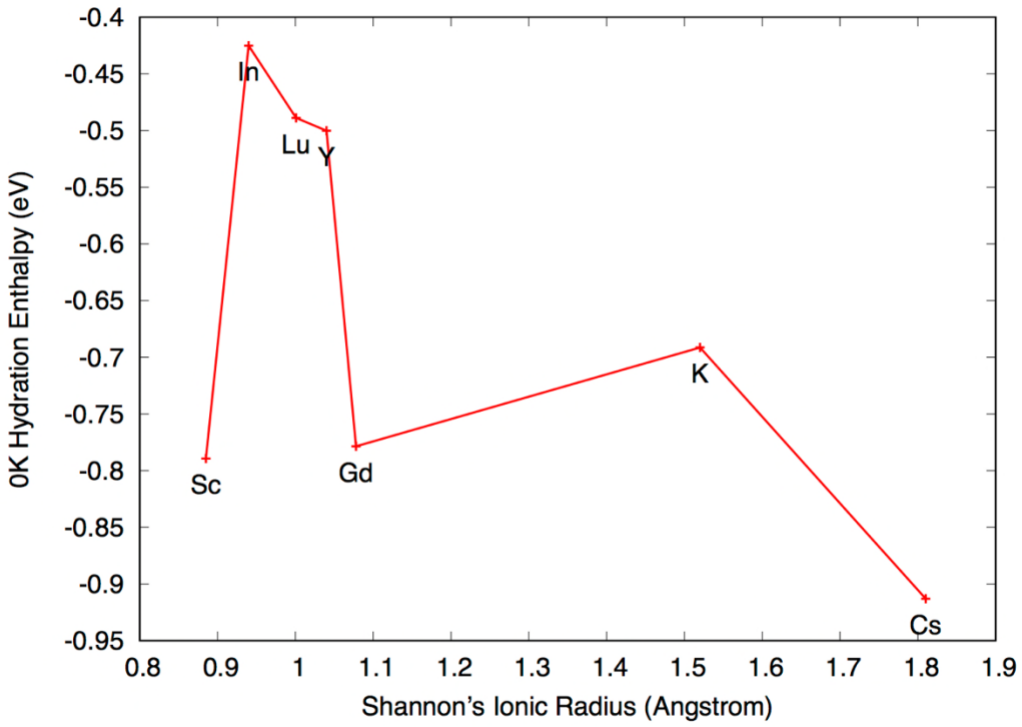

Figure 32 0K hydration enthalpy (eV/H_2O) for 7 dopants (Sc, In, Lu, Y, Gd, K, Cs) in BHCO solid-solution, w.r.t Shannon's ionic radius (Å).

Extending from 0K to finite temperature, hydration entropy needs to be taken into account, by evaluating phonon frequencies in the vibrational partition function. From Figure 33, it is observed that Lu has the most negative hydration entropy, i.e. approaching ~-250 J/mol/K, followed by K, Sc, In, Gd, Cs, and Y (~-150 J/mol/K). All 7 doped-BHCO have more negative hydration entropies than pure BHO benchmark line.

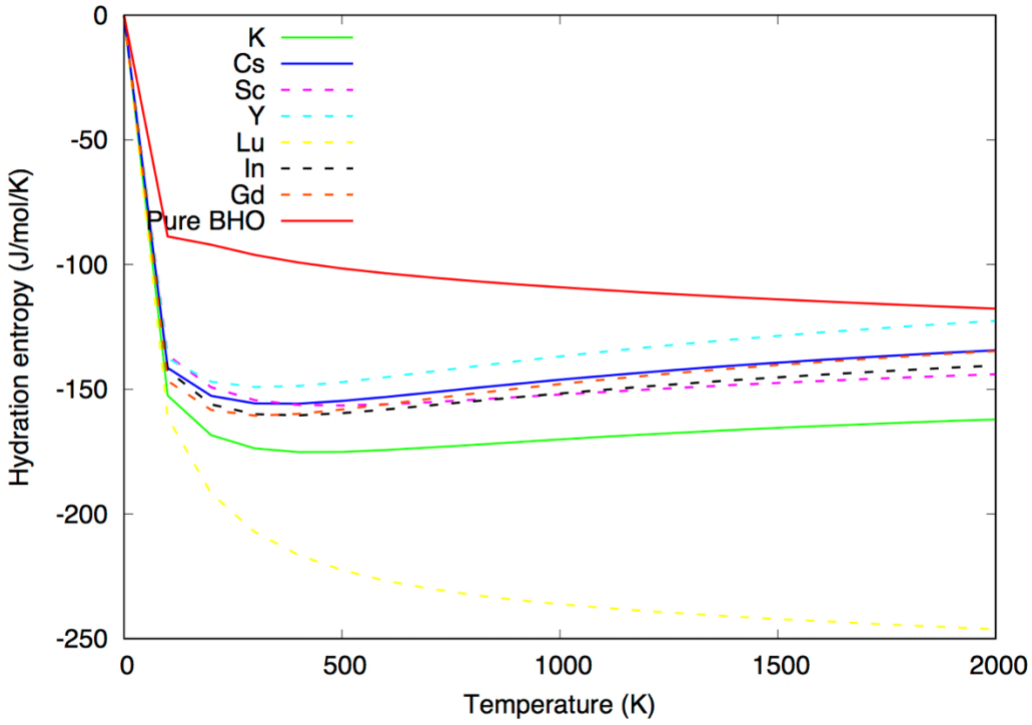

Figure 33 Hydration entropy (J/mol/K) for 7 dopants (Sc, In, Lu, Y, Gd, K, Cs) in BHCO solid-solution. Pure BHO is also plotted and serves as the benchmark.

Combining the hydration entropy and enthalpy, the Gibbs free energy of hydration is obtained. Shown in Figure 34, Lu has the largest slope, corresponding to its lowest hydration entropy. Critical temperature at which hydration free energy is zero has the sequence of $K < In < Lu < Y < Gd < Sc < Cs < BHO$.

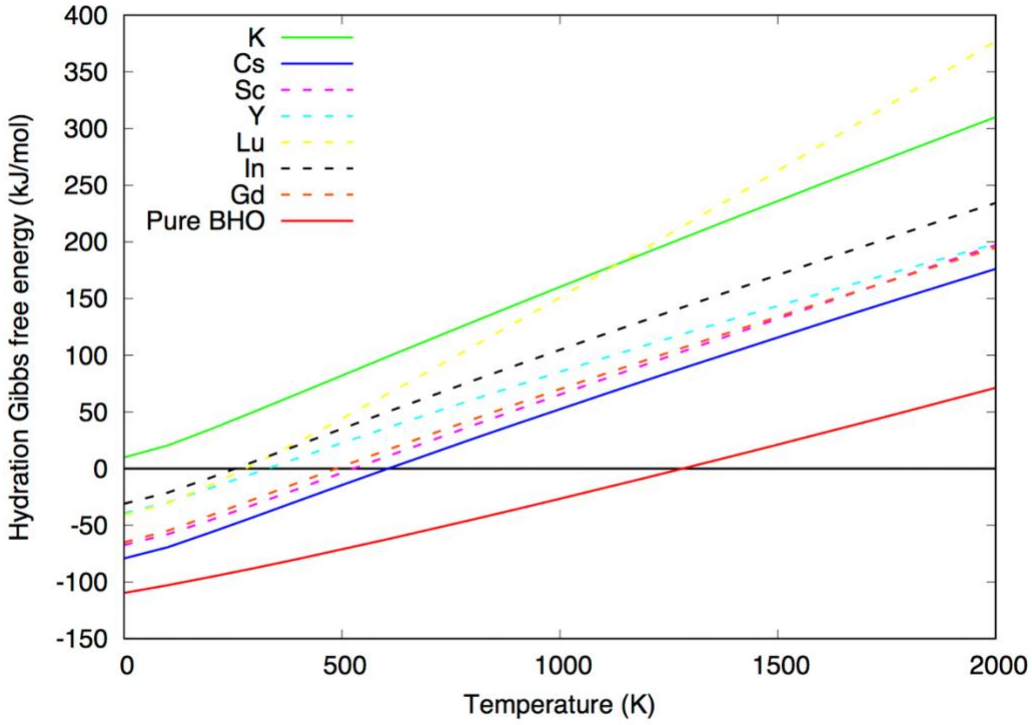

Figure 34 Hydration Gibbs free energy (kJ/mol) for 7 dopants (Sc, In, Lu, Y, Gd, K, Cs) in BHCO solid-solution. Pure BHO is also plotted and serves as the benchmark. 0 kJ line divides the thermodynamic driving force (negative/positive) for the hydration process.

Putting the Gibbs free energy into the law of mass action, proton concentration profile can be obtained. Shown in Figure 35, all 7 doped-BHCO dehydrate more quickly than pure BHO does.

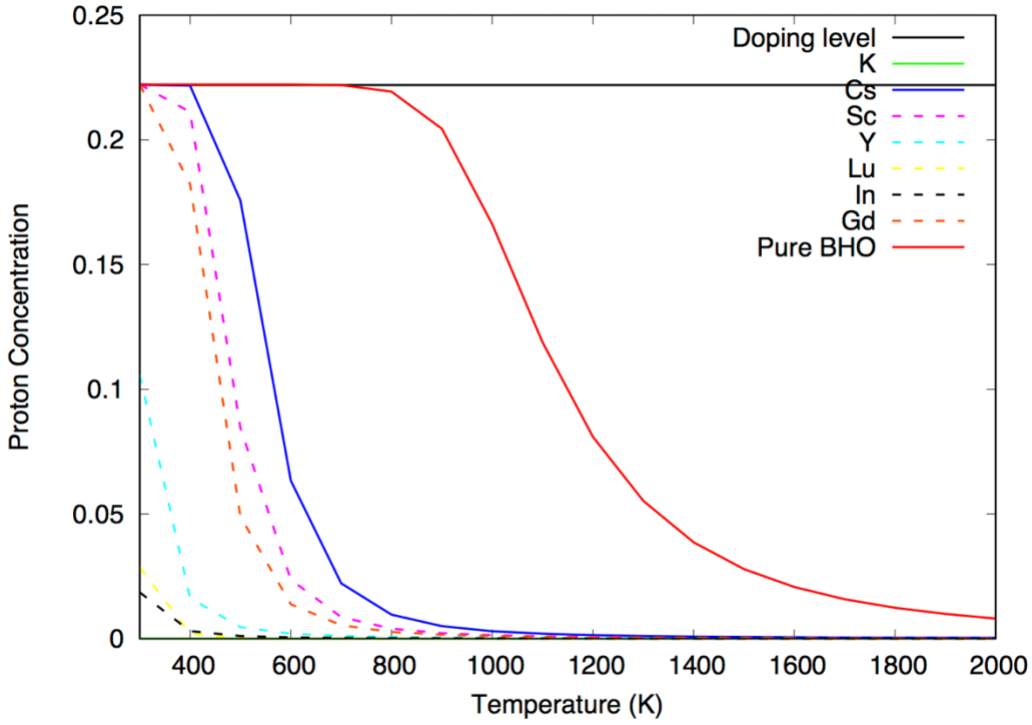

Figure 35 Proton concentration (lattice composition) for 7 dopants (Sc, In, Lu, Y, Gd, K, Cs) in BHCO solid-solution. Pure BHO is also plotted and serves as the benchmark. 0.222 line denotes the hydration saturation level and dopant level.

4.4.8 Diffusivity of doped-BHCO

To evaluate the diffusivity for non-dilute charge carriers, dilute diffusion theory is not sufficient in describing defect-defect interactions. A better approach is the *ab-initio* molecular dynamics simulation over SQS cells. Here we present diffusivity vs. inverse temperature Arrhenius plot for Gd, Sc, and Y *via ab-initio* MD simulations in Figure 36. It is found that: although diffusivities of the three doped-BHCO are all ~10^{-5} cm^2/s, Y has the lowest activation energy of 96 meV, Gd and Sc both have relatively large activation

energies of 221 and 395 meV. Combining with the hydration capability, it indicates that proton concentration and mobility play a “trade-off” in BHCO solid solution as well.

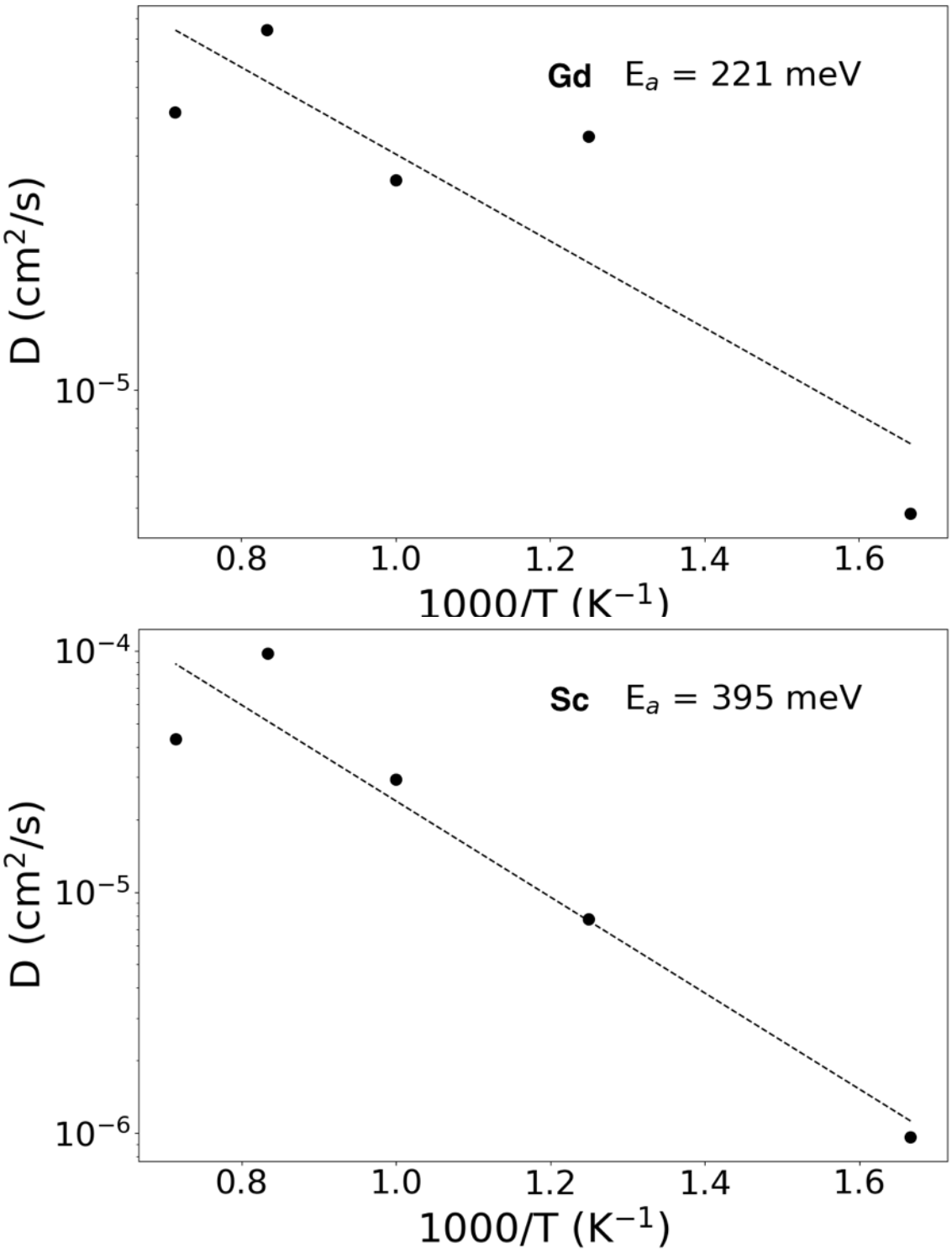

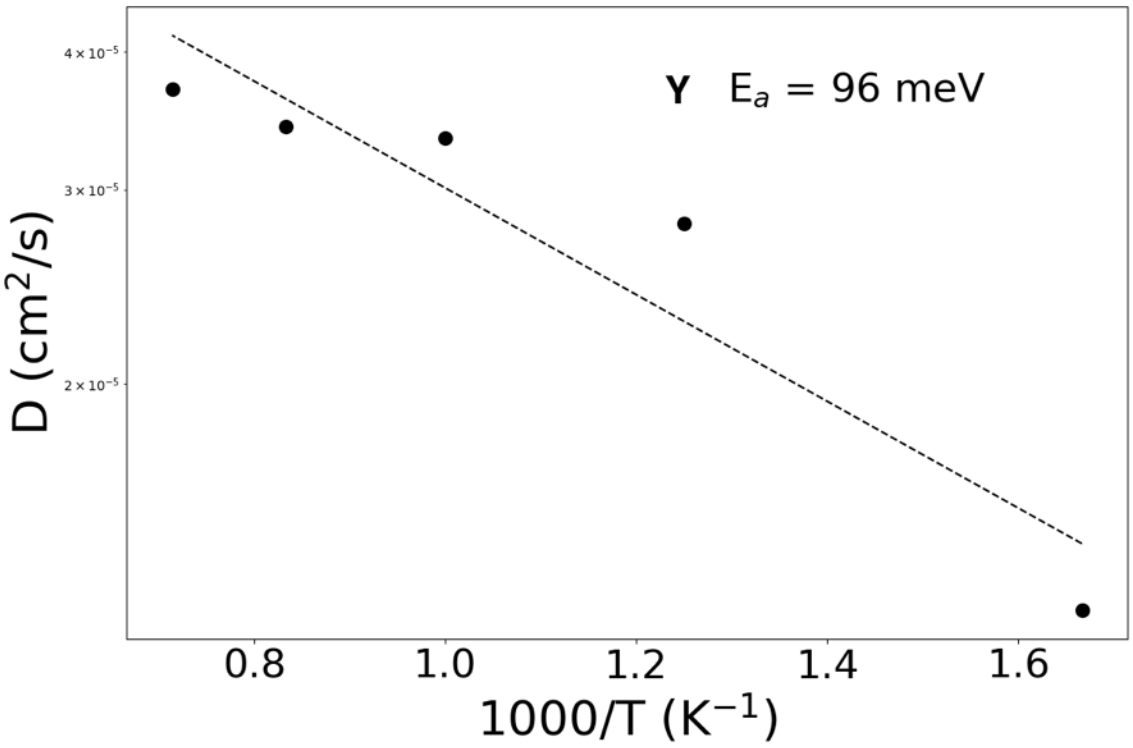

Figure 36 Arrhenius plot of proton diffusivity (cm^2/s) for 3 dopants (Gd, Sc, Y) in BHCO solid-solution. Activation energy E_a (meV) is shown at the right-top corner.

4.5 Conclusion

Dopant solubilities in BHO were calculated as $K < Lu < Y < Sc < Cs < In < Rb < Gd < Ga < Na < Al < La < Li$. At 1000K, the ones with solubilities above 20% are K, Lu, Y, Sc, Cs, In, Rb and Gd. Gd's solubility drops to 10% as temperature drops to 800K, Cs, In and Y's solubilities drop to 10% as temperature drops to 600K. Proton conductivities in doped-BHO were estimated as $Rb > K > Cs > BHO > Na > Sc > Gd > Lu$ at 827 ◦C, where they are all above 0.001 S/cm under the atmosphere of $P_{H_2O} = 0.05$. Critical temperatures against CO_2 were calculated as $K < Rb < In < Ga < Sc < Cs < Na < Al < Lu < Y < Gd < Li < La < BHO$.

Based on the above three figures of merit, it is recommended to test A-site dopants K, Rb, Cs, together with Sc, Gd, Lu experimentally as "optimal dopants" in BHO. A-site dopant K demonstrates the best solubility, proton conductivity, and CO_2 resistance. The appropriate ionic radius and electronegativity, and weak interaction of the A-site ion with the proton make K the promising A-site dopant for BHO system. Further experimental validation and optimization are needed.

BHCO solid solution, however, shows different hydration and mobility sequences comparing with BHO: The critical temperature at which hydration free energy is zero has the sequence of $K < In < Lu < Y < Gd < Sc < Cs < BHO$. Proton activation energy gives the sequence of $Y < Gd < Sc$. This agrees with the "trade-off" relation between hydration and diffusion of protons. Additionally, BHCO shows unsymmetrical mixing behavior: favorable mixing/unfavorable ordering near Ce-rich side, and *vice versa* near the Hf-rich side. Further study of microstructural defect configuration is needed to address the challenge of dopant selection in complex BHCO systems.

CHAPTER 5 ION TRANSPORT NEAR DISLOCATION IN Y:BAZRO$_3$

This chapter is a reproduction of published paper with permission from all parties: Xuejiao Li§, Lei Zhang§, Zhongfeng Tang*, Meilin Liu*, Fast Oxygen Transport in Bottle-like Channels for Y-doped $BaZrO_3$: A Reactive Molecular Dynamics Investigation, ***The Journal of Physical Chemistry C***, 2019. For this chapter, I formulated the original idea and hypothesis, provided computational resources, advised the generation and analysis of data, and participated manuscript writing and revision.

5.1 Abstract

Yttrium-doped barium zirconate (BZY) has emerged as an attractive candidate of proton (H^+) and oxygen-ion (O^{2-}) conducting solid electrolyte because of its high ionic conductivity and excellent chemical stability. In this work, the O^{2-} transport properties and mechanisms of BZY coexisting oxygen vacancies, dopants and edge dislocations are simulated by reactive molecular dynamics for the first time, and the yttrium concentration (Y %) and temperature (T) dependences of thermodynamic and kinetic properties are studied for the bulk and dislocation (Bulk and Disl) systems, respectively. It is concluded that the Y % under 20 mol% for Bulk BZY can promote O^{2-} conduction, while 30 mol% Y-doped Disl BZY has the highest O^{2-} diffusion coefficient. Besides, dislocations will accelerate O^{2-} diffusion when T is less than 1173.15 K due to the formation of double-bottle diffusion channels that enables facile reorientation of oxygen polyhedron.

Therefore, it is feasible to introduce line defects to enhance ion conductivity at low temperature in the practical applications of BZY electrolytes.

5.2 Introduction

Microstructure of defects in perovskite-type oxides are of key importance in ionic transport for a wide range of technological applications in solid oxide fuel cells, solar cells, and oxygen generators.[115, 116] Yttrium-doped barium zirconate (BZY) is one of the representative perovskite oxides, where substitution of larger radius Y^{3+} for Zr^{4+} generates oxygen vacancies and forms an oxygen deficient structure.[117, 118] Except for the point defects resulted from substitution and vacancy, there also exist line defects (dislocation), planar defects (grain boundary and stacking fault) and so on in BZY introduced during the high-temperature calcination, sintering, and stress processes.[119, 120] Effects of line and planar defects, dopant concentrations, sintering process, and temperature on local structures and ion migration properties of BZY have been widely investigated experimentally.[121-124] Theoretically, atomistic simulations studied the interactions of charge-carriers and dopants, mechanisms of ion migration, diffusion pathways, and the effects of grain boundary on overall diffusion of BZY.[125-128]

The current experimental and theoretical discoveries have shown that ion migration mechanisms can be dramatically changed in materials with existing line defects, e.g. edge dislocations. For example, dislocations can greatly accelerate ion diffusion in metals due to the formation of dislocation-pipe diffusion, but it fails to accelerate or even slows down ion diffusion in ceramics like CeO_2 and $SiTiO_3$ due to strong co-segregation of dopants and charge-carriers modulated by lattice strain near dislocation core.[129-131] Similarly,

there was no observable effect of dislocations acting as faster diffusion paths by assessing the oxygen transport in yttria-stabilized zirconia with electrochemical impedance spectroscopy and isotope exchange diffusion profiling.[132] Instead, the evidence of fast oxygen ion diffusion along dislocations in Sr-doped $LaMnO_3$ was detected by secondary ion mass spectrometry.[133] However, the defect structures and migration mechanisms of BZY coexisting point defects and line defects is not clear yet, which is crucial to a greater understanding of their macroscopic transport behavior.

Molecular dynamics (MD) modelling techniques are suitable to investigate defect transport properties at the atomistic level and have been successfully applied to study the oxygen transport of perovskite materials with line defects.[134-137] In the previous work, classical MD simulations of BZY were conducted with the combination of Coulomb and Buckingham potential, but it failed in describing the structural details, especially the rotation of oxygen octahedron.[138] However, the reactive molecular dynamics (RMD) whose reactive force field (ReaxFF) casts the empirical interatomic potential within a bond-order formalism, can implicitly describe the breaking and forming of chemical bonds by incorporating electronic-structure information.[139] In this work, the oxygen vacancies ($V_O^{\cdot\cdot}$), dopants (Y^{3+}) and edge dislocations (Disl) are incorporated into the barium zirconate (BZO) supercell. The effects of dopant concentration (Y %) and temperature (T) on structural and dynamic migration properties in the dislocation and dislocation-free BZY systems is elucidated by RMD simulations, respectively. This provides theoretical suggestions and design rules for the application of dislocation lines in BZY-based solid electrolyte materials.

5.3 Computational methods and models

5.3.1 Technological details and ReaxFF validation

The initial configurations are first pre-equilibrated for 500 ps using RMD simulations in an isothermal-isobaric (NPT) ensemble with a Nose-Hoover thermostat and barostat (drag factor = 0.2) to obtain the equilibrium lattice parameters and volumes.[140, 141] And then, the production simulations within canonical ensemble (NVT) are conducted for an evolution time of 100 ps to get the final stable configurations. Finally, all structural and dynamic analysis are based on the NVT results. During the RMD simulations, the Verlet integration scheme is used to solve the Newtonian equation of motion for the ions with an integration step time of 1 fs, and the 3-D periodic boundary conditions are applied to eliminate boundary effects.[142] The ReaxFF interaction parameters are consistent with reference as implemented in the LAMMPS package, and the charge equilibration method is performed to minimize the electrostatic energy with a precision of 10^{-6}.[143] To verify the predictability of ReaxFF, the radial distribution functions (RDFs) as one of the fundamental structural information are obtained from the trajectory recorded to evaluate the nearest distance (*R*) and coordination number (*CN*), and compare with experimental data.

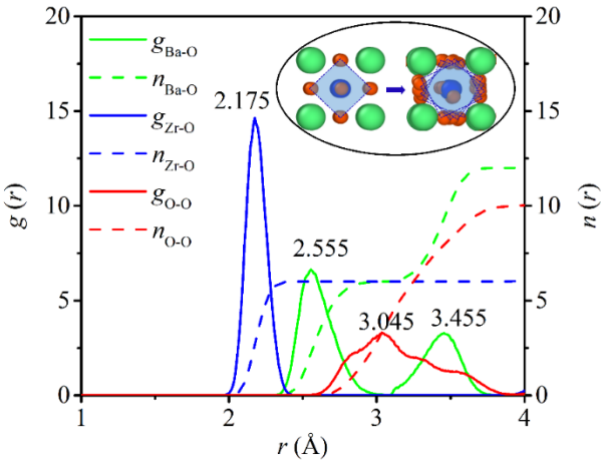

Figure 37 Radial distribution functions $g(r)$ and its integral functions $n(r)$ of Ba-O, Zr-O and O-O for Bulk BZO at room temperature by RMD simulations.

From Figure 37, the simulated *R* of Zr-O for Bulk 8x8x8 BZO at room temperature is 2.175 Å, slightly greater than the experimental value 2.099 Å.[144] It can be seen that there are two sharp peaks of Ba-O, and the average distance of 3.005 Å agrees well with XRD result (2.969 Å).[145] Furthermore, the first shell *CN*s of Ba-O and Zr-O are 11.99 and 6.00 Å, respectively, significantly consistent with that of ideal Bulk BZO. However, the O-O peak is relatively gentle in a large distance range from 2.505 to 3.995 Å attributing to the distortion of oxygen octahedron (see the insert of Figure 37), and the position of highest peak is similar to literature value of 3.09 Å;[143] meanwhile, the unsmooth RDF curve of O-O hints the limitation of small simulation system. In addition, the lattice parameters (α) of Bulk 8x8x8 BZO and BZY systems changing with *T* and *Y* % are also simulated to evaluate the thermal and chemical expansion coefficient (*TEC* and *CEC*), respectively. From **Section. S1** of the supporting information (SI), the simulated α are slightly greater than experimental values, however, the *CEC* of 0.0413 for Bulk BZY are similar to the experimental result of 0.0316 and DFT result of 0.0301.[104, 128] Besides,

the volumetric and linear *TEC* (3.12×10^{-5} and $1.06 \times 10^{-5}\ K^{-1}$) of Bulk BZO are almost consistent with the experimentally measured results, suggesting that the ReaxFF is credible to study the structural characteristics.[146, 147]

Table 1 Supercell models of Bulk and Disl BZY with corresponding ionic number and mole ratio concentration

System	Total	Ba^{2+}	Zr^{4+}	Y^{3+}	Y %	O^{2-}	$V_o^{\cdot\cdot}$	$V_o^{\cdot\cdot}$ %
Bulk Y10	39600	8000	7200	800	10.00	23600	400	1.67
Bulk Y15	39400	8000	6800	1200	15.00	23400	600	2.50
Bulk Y20	39200	8000	6400	1600	20.00	23200	800	3.33
Bulk Y25	39000	8000	6000	1600	25.00	23000	1000	4.17
Bulk Y30	38800	8000	5600	2400	30.00	22800	1200	5.00
Bulk Y36	38560	8000	5120	2880	36.00	22560	1440	6.00
Disl Y10	38783	7835	7051	784	10.01	23113	392	1.67
Disl Y15	38587	7835	6659	1176	15.01	22917	588	2.50
Disl Y20	38391	7835	6267	1568	20.00	22721	784	3.34
Disl Y25	38196	7835	5877	1958	24.99	22526	979	4.17

Disl Y30	38000	7835	5485	2350	29.99	22330	1175	5.00
Disl Y36	37765	7835	5015	2820	35.99	22095	1410	6.00

5.3.2 Model construction and optimization

Based on the above discussion, the large-scaled Bulk and Disl BZY supercells with multiple Y % (from 10 mol% to 36 mol%) are modeled by ATOMSK program, whose steps are similar to author's previous work as shown in **Section S2**.[138, 148, 149] The system names, ionic numbers and mole ratio concentrations of these BZY systems are listed in Table 1. Considering the association of point and line defect structure, the Monte Carlo (MC) simulations are carried out by the command of atom/swap to randomly exchange the position of Y^{3+} and Zr^{4+}, to search the minimum of potential energy, and to obtain the preliminary stable configuration.[150] In Figure 38, the ionic distribution maps of Disl Y10 ~ Y36 at the yz plane after MC simulations at 1073.15 K are depicted, respectively. As shown in Disl Y10, the symmetric dislocation structure ensures the periodic boundary conditions of the simulated system, and the larger y and z (10.494 and 18.996 nm) spatial extent avoids the interaction of two dislocations, while the smaller x axis (2.968 nm) reduces computational cost.

Figure 38 Ionic distribution maps of Disl BZY at the yz plane after MC simulations (color code: Zr-bule, Y-yellow, Ba-green and O-red, the sizes of Ba and O spheres are zoomed out to clearly show the illustrations, and the red T-shaped marks denote the dislocation cores).

From Figure 39 (a), the total energy (E_t) and swap success (*SS*) of Disl BZY systems are convergent as the increase of swap attempt (100 times/100 steps in 100,000 times), respectively, indicating the MC simulations overcoming the dynamic energy barrier accelerate the simulation system reach to equilibrium. In addition, the Y^{3+} number (N_Y) around two dislocation centers ((0.5x, 0.5y, 0.25z) and (0.5x, 0.5y, 0.75z)) as a function of sphere shell radius (r = 0 to 120 Å) are summarized in **Table S1** to evaluate the association of dislocation and dopant. It can be seen that the corresponding N_Y almost linearly increases between 30 and 90 Å indicating the even distribution of Y^{3+} after structure relaxation. In Figure 39 (b), the average percentage of Y^{3+} number (P_Y) for Disl BZY systems is depicted separately, and the maximum of P_Y is about 8% when the r is between 50 and 55 Å suggesting the influence range of dislocation core.

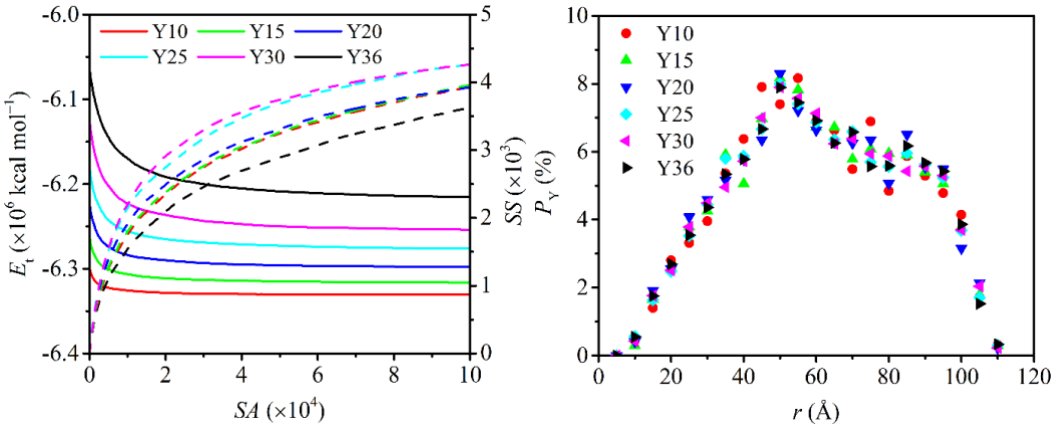

(a) (b)

Figure 39 (a) Total energy E_t and swap success SS of Disl BZY as a function of swap attempt SA, and (b) shell radius r dependence of the Y^{3+} distribution percentage P_Y for Disl BZY by MC simulations

5.4 Results and discussion

5.4.1 Oxygen transport properties

The mean square displacement (MSD) of O^{2-} can be obtained from the RMD simulations and expressed as follows,

$$MSD(j) = \frac{1}{N}\frac{1}{(M-j)}\sum_{i=1}^{N}\sum_{j_0=1}^{(M-j)}\{[x_i(j_0+j)-x_i(j_0)]^2+[y_i(j_0+j)-y_i(j_0)]^2 + [z_i(j_0+j)-z_i(j_0)]^2\}$$

where N represent the total O^{2-} number, x_i (j), y_i (j), and z_i (j) are coordinates of O^{2-} i at time step j recorded during the M steps simulation. The first summation runs over all the N ions, and the second summation runs over (M–j) times after time origin j_0. In addition,

the O^{2-} self-diffusion coefficient (D_O, unit: cm^2s^{-1}) can be evaluated from the long-time limit of the MSD on the basis of the Einstein formula,

$$D_O = \frac{1}{6}\lim_{\tau\to\infty}\frac{\mathrm{d}(\mathrm{MSD}(\tau))}{\mathrm{d}\tau}$$

where τ is the elapsed time.

5.4.2 Diffusion coefficient vs. Y %

The NVT simulations for Bulk and Disl BZY systems with the *Y* % from 10 mol% to 36 mol% are first conducted at 1073.15 K to evaluate the *Y* % dependence of D_O. In Figure 40, the MSDs of these systems show good linear relationships with simulation time, and the total D_O (O_{total}) and the D_O in three directions (O_x, O_y, and O_z) are deduced from the corresponding MSDs after 10 ps, respectively. To avoid the error caused by individual initial configuration, 10 initial configurations with randomly distribution of Y^{3+} and $V_o^{\cdot\cdot}$ for each Bulk BZY are modelled separately. The O_{total} and its average value of 10 configurations are listed in **Table S2**, and the uncertainty of D_O introduced by initial configuration is thus evaluated as $1.95\sim8.46\times10^{-8}cm^2s^{-1}$. Besides, the average value and error bar of O_{total} are pictured in **Fig. S2** from which the trend of O_{total} varied with *Y* % does not change, and thus one kind of initial configuration is considered in the following simulation systems.

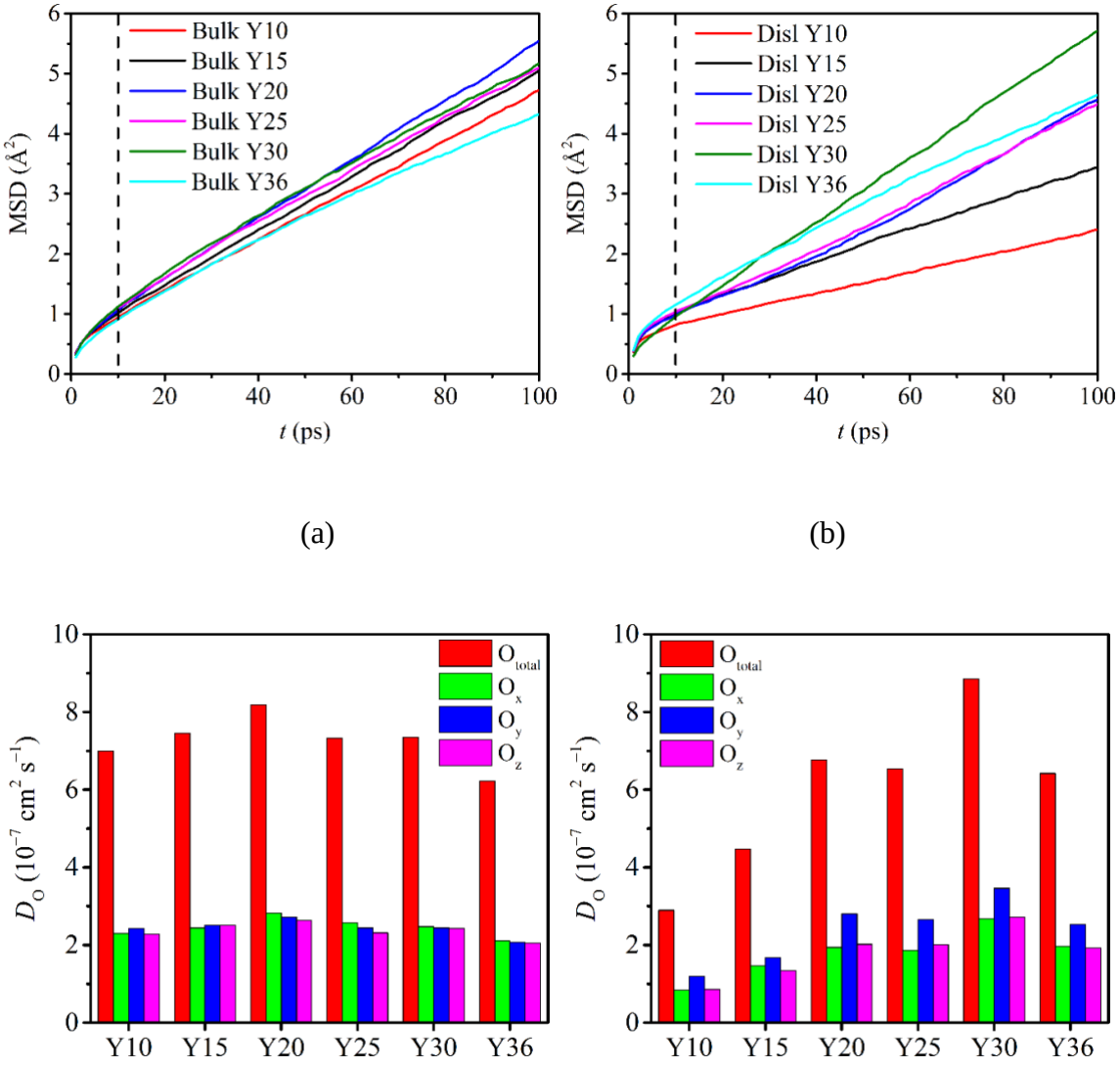

Figure 40 Mean square displacements MSDs of (a) Bulk and (b) Disl BZY, and total and separate O^{2-} diffusion coefficient D_O of (c) Bulk and (d) Disl BZY at 1073.15 K

As shown in Figure 40 c and d, the O_{total} for Bulk BZY increases with the *Y* % increasing from 10 mol% to 20 mol%, and then decreases with the continually increase of *Y* %; while the O_{total} of Disl BZY increases with the *Y* % from 10 mol% to 30 mol% except for slightly decreasing at *Y* % of 25 mol%. The Bulk Y20 and Disl Y30 system have the

highest D_O, respectively, which agree well with the experimental Y^{3+} concentration range of 10 mol% ~ 30 mol% for fast ion BZY conductor.[121, 146, 151] In addition, the O_{total} are between $6.22 \times 10^{-7} \sim 8.19 \times 10^{-7} cm^2 s^{-1}$ and $2.90 \times 10^{-7} \sim 8.85 \times 10^{-7} cm^2 s^{-1}$ for Bulk and Disl BZY, respectively, similar to the experimental and computational values of 6.6×10^{-8} and $1.1 \times 10^{-7} cm^2 s^{-1}$.[117, 143] And the slight overestimation depends on the ideal simulation models without involving other defects such as grain boundary which maybe exist in high-temperature experiments, produce resistances and hinder the ion transport.[9] Furthermore, most of the O_{total} for Disl systems are lower than the corresponding Bulk systems, indicating that there is no dislocation-pipe diffusion for O^{2-} whose diffusivity should be higher than lattice diffusivity. However, the O_y is significantly larger than corresponding O_x and O_z in all Disl BZY, which suggests that the positive effect of dislocation on the transport of O^{2-} at a certain direction.

5.4.3 Diffusion coefficient vs. T

In order to evaluate the T dependence of D_O, the RMD simulations of Bulk Y20, Bulk Y30 and Disl Y30 are conducted at five temperatures varying from 873.15 to 1273.15 K, respectively. It is noted that the thermal expansion effect is ignorable because *CEC* of BZY is larger than *TEC* with several orders of magnitude (**Section 4.3.1**), therefore, the last configurations from above NPT simulations at 1073.15 K are used as the initial inputs for the reproduction NVT simulations with multiple temperatures, respectively. In Figure 41, the D_O of the three systems increase about one order of magnitude with the increased temperature, and the D_O of Bulk Y30 changes significantly from 2.30×10^{-7} to $1.65 \times 10^{-6}\ cm^2 s^{-1}$. Besides, the D_O of Disl Y30 is higher than that corresponding value

of Bulk Y20 and Y30 when temperature is below 1173.15 K, while the D_O of Bulk Y20 are larger at higher temperature (≥1173.15 K). The result conforms to the previous conclusion that the D_O is slowed down in $SrTiO_3$ with dislocations at high temperature of 1200 K, therefore, it can be deduced that the edge dislocations will accelerate the ionic diffusion at lower temperature, which is a process of structure-driven (a thermodynamic factor).[131]

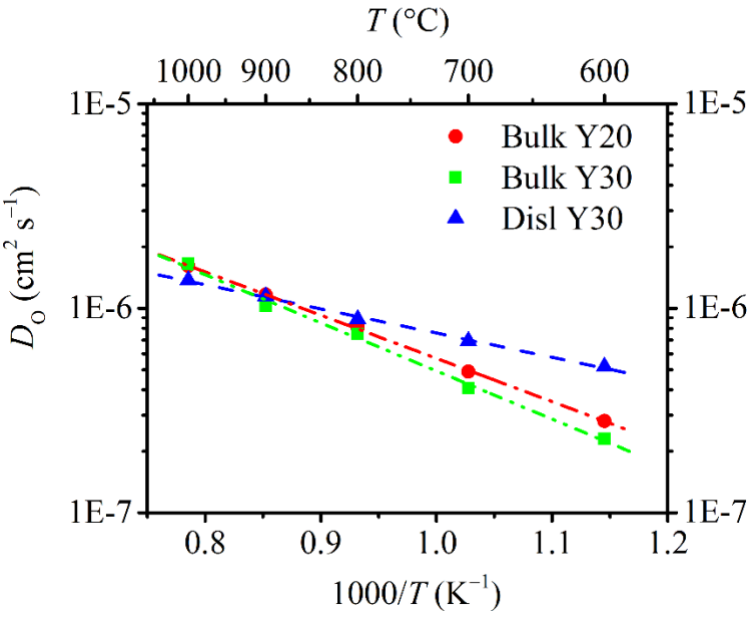

Figure 41 Temperature T dependence of O^{2-} diffusion coefficient D_O

In addition, the pre-exponential factor (A) and activation energy (E_a) are evaluated by fitting the relationship of D_O and T to the Arrhenius equation,

$$D_O = A\exp(-\frac{E_a}{RT})$$

The calculated E_a of D_O are 0.42 and 0.47 eV for Bulk Y20 and Bulk Y30, greatly lower than corresponding simulated values of 0.95 eV for 12 mol% BZY (1000-2000 K).[143]

The perfection of the simulation cell decreases the E_a, and the temperature range and large-scaled model are also the possible influence factors on E_a. Besides, the E_a of Disl Y30 (0.24 eV) is lower than that of Bulk Y20 and Y30, indicating the edge dislocations decrease the migration barriers of O^{2-} at low temperature range. In addition, the A of the three systems are positively correlated with corresponding E_a, which are 1.16×10^{-5}, 1.12×10^{-4} and $7.42 \times 10^{-5}\ cm^2 s^{-1}$, respectively.

5.5 Embedded-trapping effect

Compared with D_O, the ionic conductivity (σ, unit: $S \cdot cm^{-1}$) involves the term of ion concentration which can be approximately calculated from the Nernst-Einstein equation,[152]

$$\sigma = \frac{e^2 c Z^2 D}{k_B T} = \frac{4e^2 N D}{k_B T V}$$

where e is primitive charge (unit: C), Z is the charge number, c the mole concentration of O^{2-} who is the main carrier of charge, and V the volume (unit: cm^3). Figure 42 shows that the conductivity of oxygen ion (σ_O) for Bulk BZY systems changes with the T and Y %, respectively. It is found that the σ_O of each systems increases as T increases from 873.15 to 1273.15 K, and the overall σ_O increases from 0.07 $S \cdot cm^{-1}$ (for Bulk Y36) to 0.34 $S \cdot cm^{-1}$ (for Bulk Y20). At 873.15 and 973.15 K, that σ_O decreases from 0.11 and 0.16 to 0.07 and 0.10 $S \cdot cm^{-1}$ as the Y % increases from 10 mol% to 36 mol%.

However, the relationship curve of σ_O and Y % is turned at 1073.15 K, the system owning the highest σ_O transfers from Bulk Y10 to Bulk Y20 as the T increasing, and the

maximum of σ_O at 1073.15 and 1173.15 K are 0.20 and 0.27 $S \cdot cm^{-1}$, respectively. In other word, the 10 mol% and 20 mol% Y-doped system are conducive to the O^{2-} transport when temperature below and above 1073.15 K, respectively. These results are consistent well with the experimental results where ionic conductivity increases with the Y content increasing from 10 to 20 mol %, but does not further increase when the Y content is higher than 20 mol %.[153, 154] Besides, the right-shift of σ_O maximum could be explained by the embedded-trapping mechanism where the trapping ability of single Y^{3+} is weaken as the T increases,[155] and thus it needs to dissolve more Y^{3+} to capture the vacancies. That is why the Disl Y30 has the highest D_O but not Disl Y20 whose embedded-trapping effect is more feeble due to a small amount of N_Y.

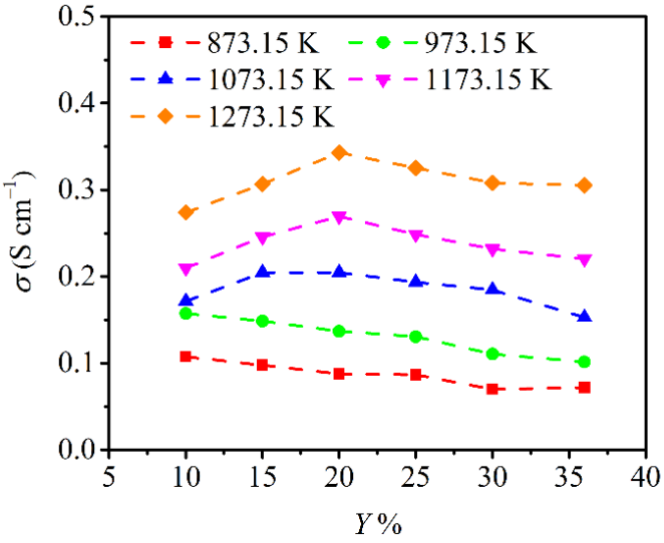

Figure 42 Y^{3+} concentration Y% dependence of O^{2-} conductivity σ_0 for Bulk BZY

5.6 Oxygen transport mechanism

Considering the influence range of dislocation core (50~55 Å in **Section 4.3.2**), the atomic trajectories around dislocation cores are traced in the ranges of x [0, x_{max}], y [$\frac{6}{25}y_{max}$, $\frac{17}{25}y_{max}$], z [$\frac{1}{8}z_{max}$, $\frac{3}{8}z_{max}$] and x [0, x_{max}], y [$\frac{7}{25}y_{max}$, $\frac{18}{25}y_{max}$], z [$\frac{5}{8}z_{max}$, $\frac{7}{8}z_{max}$], respectively. As shown in Figure 43, the two inverted bottle type channels around the dislocation cores in Disl Y30 are depicted in the local enlarged drawings. It should be noted that the frameworks of the two bottles connected by the position of Ba atoms are not symmetric but staggered along y axis, and thus the double-channel diffusion of O^{2-} will be achieved. From the partial enlargements, all of the atomic positions around the dislocation cores are greatly changed to fill original cracks, the internal stresses are relaxed and lattice strain is reduced. Besides, the animation of micro-local structures of Disl Y30 surrounding bottom dislocation core varied with simulation time (100 configures from 100,000 steps) is shown in the SI. It can be clearly seen that each atom moves with time to search an equilibrium and stable position, and the continuous generation and breaking of Zr-O and Y-O bonds and the rotation of oxygen polyhedrons result in the O^{2-} transport.

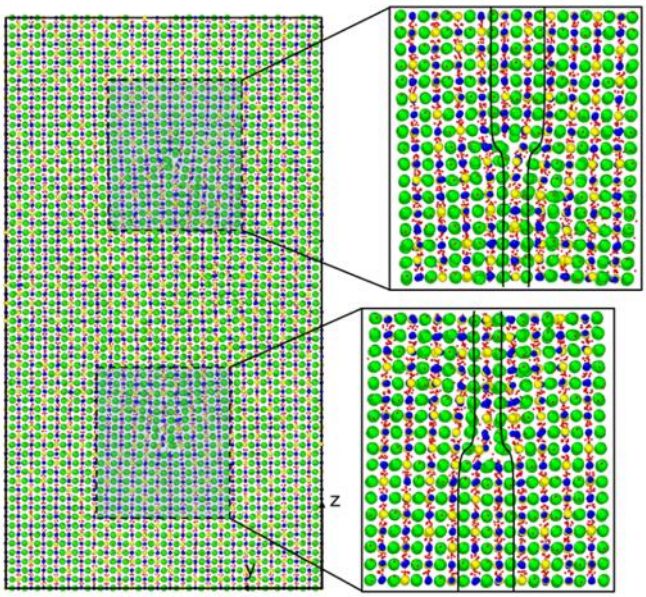

Figure 43 Profile of double-bottle diffusion channel in Disl Y30

Furthermore, the snapshots of the rotations of oxygen polyhedron are pictured in Figure 44, and the cutoff distances of Zr-O and Y-O are set as the values of 2.4 and 2.6 Å (refer to the RDFs from **Fig. S3** and **Table S3**). In snapshot 1, the oxygen ion (O1) initially connects with Zr2 forming a stable tetrahedron, while the polyhedron centered with Y1 hides in the second layer behind the Zr2-centered tetrahedron. As the simulation time increases, the Y1-centered polyhedron gradually deviates from the original position because of the big enough space introduced by the dislocation, and links with the Zr1-centered tetrahedron by a shared oxygen atom (snapshot 2). In snapshot 3, the O1 is successfully taken away by Y1-centered polyhedron that rotates to the rear of the Zr2-centered polyhedron fulfilling the oxygen migration. In the selected diffusion path, the total energy of snapshot 2 is the lowest, which is thought as the ground state energy. The relative energy of snapshot 1 and 3 are 18.65 and 15.61 eV, respectively, and the lower energy of snapshot 3 indicating a more stable configuration. Regrettably, it is hard to

extract the energy change of local ion movement from the total energy and get the migration barrier of a certain O^{2-}, although this kind of O^{2-} diffusion along the slender bottleneck is very easy to capture. Overall, the rotational movements of oxygen polyhedrons are significantly promoted with the help of the effective space introduced by dislocations, and the long distance O^{2-} transport is fulfilled by such reorientation of oxygen acceptors. However, it is hard to track the long-range diffusion path of O^{2-} for such a big simulation model due to the limitation of simulation time and expensive computational costs.

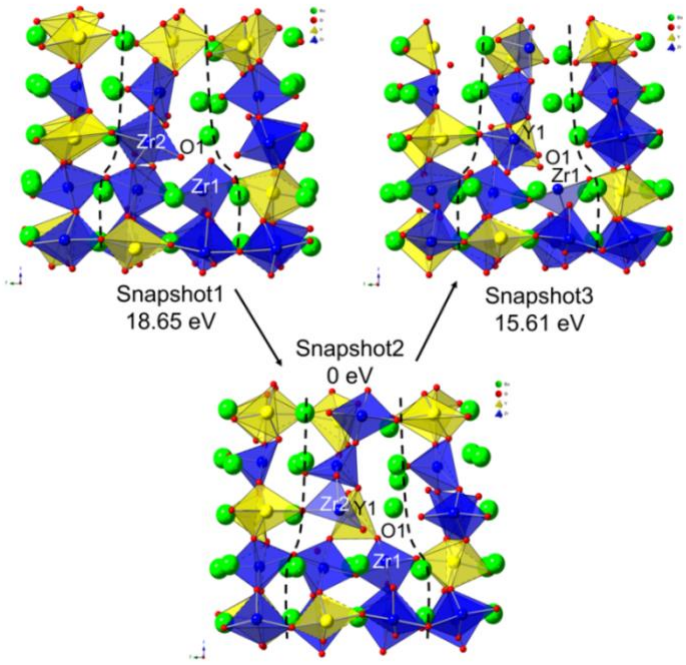

Figure 44 Identification of O^{2-} diffusion mechanism in Disl Y30 around the dislocation core

5.7 Conclusion

The RMD simulations are applied to study the structural characteristics, ion transport properties and migration mechanism of Y-doped $BaZrO_3$ systems with/without edge dislocations, including the radial distribution function, expansion coefficient, ionic self-diffusion coefficient (D_O) and conductivity as a function of dopant concentration and temperature. Studies have shown that ReaxFF precisely captures the structural details, i.e., the nearest neighbor distances and coordination numbers of ionic pairs agree well with experimental results. Besides, the evaluated D_O are also consistent with the literature values at analogous conditions, and Bulk Y20 and Disl Y30 system have the highest D_O at 1073.15 K, respectively. From the relationships of T and Y% on conductivity, the 10 mol% and 20 mol% Y-doped Bulk BZY are more favorable for the oxygen conduction below and above the critical temperature of 1073.15 K, which is explained by the embedded-trapping mechanism. In addition, dislocation will accelerate O^{2-} diffusion at temperatures less than 1173.15 K via structure-driven double-bottle diffusion channel of O^{2-} around dislocation core. Eventually, the O^{2-} transport mechanism via the reorientation of oxygen polyhedrons is elaborated within the local structure near dislocation core. The simulation results are heuristic in dislocation-modified ion transport behavior, which sheds insight for further development of efficient O^{2-} conducting electrolyte through microstructure engineering.

5.8 Supplementary information

S1. Expansion characteristics

The poor chemical and thermal stability as a consequence of mismatch between material components are detrimental to the overall performance and durability of the

material[156, 157]. In the perovskite materials, the lattice parameter associated with chemical component and temperature is defined as chemical expansion and thermal expansion, respectively[158]. The chemical expansion coefficient (CEC) can be evaluated as,

$$CEC = \frac{1}{\delta_i}\frac{\alpha_i - \alpha_0}{\alpha_0}$$

where δ_i is the defect concentration usually represented by $V_O^{\cdot\cdot}$ concentration or non-stoichiometry in $BaZr_{1-2\delta}Y_{2\delta}O_{3-\delta}$, α_0 and α_i the lattice parameters for perfect and defected crystal. In this work, the δ_i is unified as the Y^{3+} concentration (Y %), and Fig. S1a shows the lattice parameter (a) of Bulk 8x8x8 BZY as a function of Y % at room temperature. Therefore, the CEC can be evaluated from the slope of fitted linear curve.

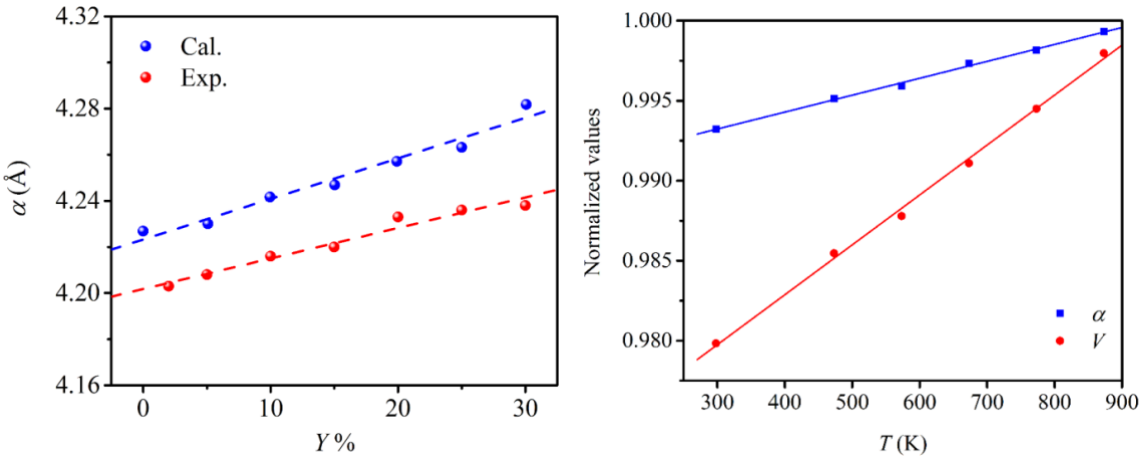

(a) (b)

Fig. S1. (a) lattice parameter a as a function of dopant concentration Y % for Bulk 8x8x8 BZY, and (b) normalized a and cell volume V as a function of temperature T for Bulk 8x8x8 BZO.

Besides, the RMD simulations of Bulk 8x8x8 BZO under six temperatures (298.15, 473.15, 573.15, 673.15, 773.15 and 873.15 K) are also conducted to obtain the thermal expansion properties. For cubic BZO system, the linear/volumetric thermal expansion coefficients (*L*TEC/VTEC) can be expressed as the partial derivative of a or lattice volume (V) versus temperature at constant pressure shown below:

$$LTEC = \frac{1}{\alpha_0}\left(\frac{\partial \alpha_i}{\partial T}\right)_P$$

$$VTEC = \frac{1}{V_0}\left(\frac{\partial V_i}{\partial T}\right)_P$$

where V_i represent the equilibrium volume at different temperatures and V_0 the perfect cell volume of 77.074 Å. The normalized a and V as a function of temperature are drawn in Fig. S1b.

S2. Modeling of Bulk and Disl BZY

The crystal structure of BZO is extremely similar to that of $SrTiO_3$ whose slip plane $\langle 100 \rangle \{011\}$ can be used as a reference for constructing the BZY with edge dislocations[159]. First, the cubic unit cell of BZO (α=4.256 Å) with space group Pm3m is rotated to [011] [100] [011] crystallographic directions corresponding to the dislocation line vector, Burgers vector, and slip plane normal[160]. Second, the oriented BZO is magnified by 5, 25, and 32 times along x, y, and z axis to construct supercell (Bulk BZO) with 8000 Ba, 8000 Zr and 24000 O. Third, and the middle two columns (a BaO and a ZrO_2 plane) in the y-z plane of Bulk BZO are partially removed along x axis remaining 39175 atoms (7835 Ba, 7835 Zr and 23505 O). Besides, the BZY systems with

different Y % are formed by randomly substituting Zr^{4+} with Y^{3+} and deleting O^{2-} to generate $V^{\cdot\cdot}$. Finally, the cracks of above initial configurations are healed after the classical MD relaxations, and the dislocation systems (Disl BZO and BZY) will be built.

S3. MC simulations

Table S1. The number of Y^{3+} around two dislocation cores (denoted as C1 and C2) as a function of sphere shell radius (r, unit: Å) of the last MC configurations.

r	$Y10_{C1}$	$Y10_{C2}$	$Y15_{C1}$	$Y15_{C2}$	$Y20_{C1}$	$Y20_{C2}$	$Y25_{C1}$	$Y25_{C2}$	$Y30_{C1}$	$Y30_{C2}$	$Y36_{C1}$	$Y36_{C2}$
5	0	0	0	0	1	0	1	1	1	1	3	1
10	5	2	4	3	6	8	11	13	15	7	18	17
15	14	15	24	22	32	42	42	46	54	51	70	64
20	34	39	50	57	73	81	95	90	116	107	146	140
25	60	65	101	95	137	145	163	160	207	194	245	241
30	92	95	152	144	214	212	249	248	314	298	364	368
35	138	133	225	210	307	281	367	357	430	415	517	516
40	188	183	291	263	399	370	494	460	578	536	681	678
45	242	253	374	344	498	470	618	597	751	692	879	856
50	296	315	470	440	634	594	773	755	942	872	1100	1080
55	362	377	562	532	746	708	923	895	1113	1057	1305	1295
60	410	437	633	619	852	810	1055	1032	1275	1230	1488	1502
65	460	491	710	700	945	914	1182	1154	1418	1380	1660	1683
70	499	538	776	770	1034	1021	1305	1289	1565	1533	1848	1866
75	559	586	845	844	1136	1118	1417	1400	1701	1676	2013	2015
80	602	619	917	912	1210	1203	1523	1512	1836	1817	2185	2158
85	658	655	990	978	1310	1307	1639	1629	1960	1948	2359	2332
90	693	703	1050	1045	1395	1396	1748	1740	2095	2075	2505	2506
95	735	736	1116	1098	1489	1474	1854	1839	2226	2193	2659	2658
100	768	768	1153	1150	1528	1534	1918	1919	2300	2293	2769	2766
105	782	781	1172	1173	1564	1565	1950	1954	2345	2344	2810	2811
110	784	784	1176	1176	1568	1568	1958	1958	2350	2350	2820	2820

S4. Mean square displacements and diffusion coefficients

Fig. S2a is an example of 10 Mean square displacements (MSDs) for Bulk Y30, that shows good linear relationships with time after 10 ps. In addition, the average O^{2-}

diffusion coefficients (D_O) simulated from 10 configurations and their corresponding error bars are depicted in Fig S2b and summarized in Table S2.

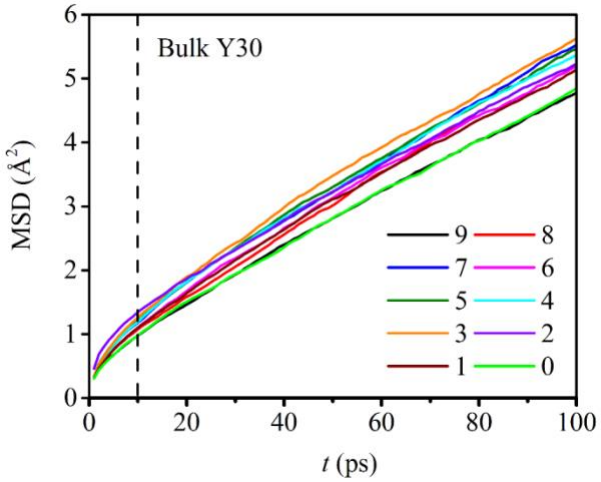

(a)

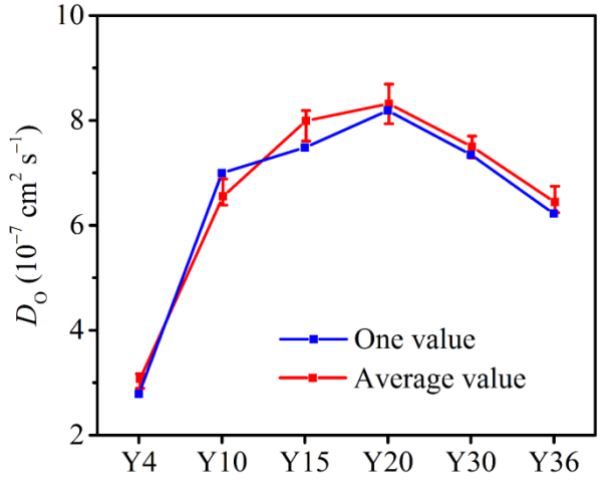

(b)

Fig. S2 (a) Mean square displacements MSDs of Bulk Y30 with 10 initial configurations, and (b) O^{2-} diffusion coefficient D_O of Bulk BZY by RMD simulations

Table S2. D_0 (10^{-7} cm^2s^{-1}) of Bulk BZY simulated from 10 configurations

System	Bulk Y4	Bulk Y10	Bulk Y15	Bulk Y20	Bulk Y30	Bulk Y36
1	3.06	6.36	7.95	7.94	9.63	6.95
2	2.76	6.43	8.20	8.17	7.44	8.09
3	2.91	6.51	7.70	8.58	8.33	7.85
4	3.21	6.30	7.79	8.56	6.81	7.43
5	3.04	6.06	7.51	8.07	9.17	7.65
6	3.10	6.95	8.24	7.41	7.47	7.58
7	3.18	6.20	8.08	8.97	8.26	7.86
8	3.37	6.57	7.89	9.43	7.63	7.15
9	2.79	6.71	7.92	8.62	8.41	7.34
10	3.20	7.33	8.54	7.35	7.82	6.99
Aver.	3.06	6.54	7.98	8.31	8.10	7.49
U_C	0.19	0.38	0.29	0.65	0.85	0.39

S5. Radial distribution functions (RDFs) of Bulk and Disl BZY

The RDFs g(r) and their integral curves n(r) of Bulk and Disl BZY at 1073.15 K are drawn in Fig. S3 to investigate the effect of dopant concentration on local structure. For convenience, the peak positions of RDFs and coordination number (CNs) of four ion pairs for Bulk and Disl BZY systems are summarized in Table S3. In addition, the average potential energy (PE) of single atom for Bulk and Disl BZY are also calculated. It is shown that the PE of Disl BZY are lower than corresponding Bulk systems, which means the structure with edge dislocations are more stable and the oxygen vacancy formation energies are lower. Furthermore, the PE value decreases as the Y % increases from 10 mol% to 30 mol% verifying that the interactions of Y^{3+} and other ions are higher than that of Zr^{4+}.

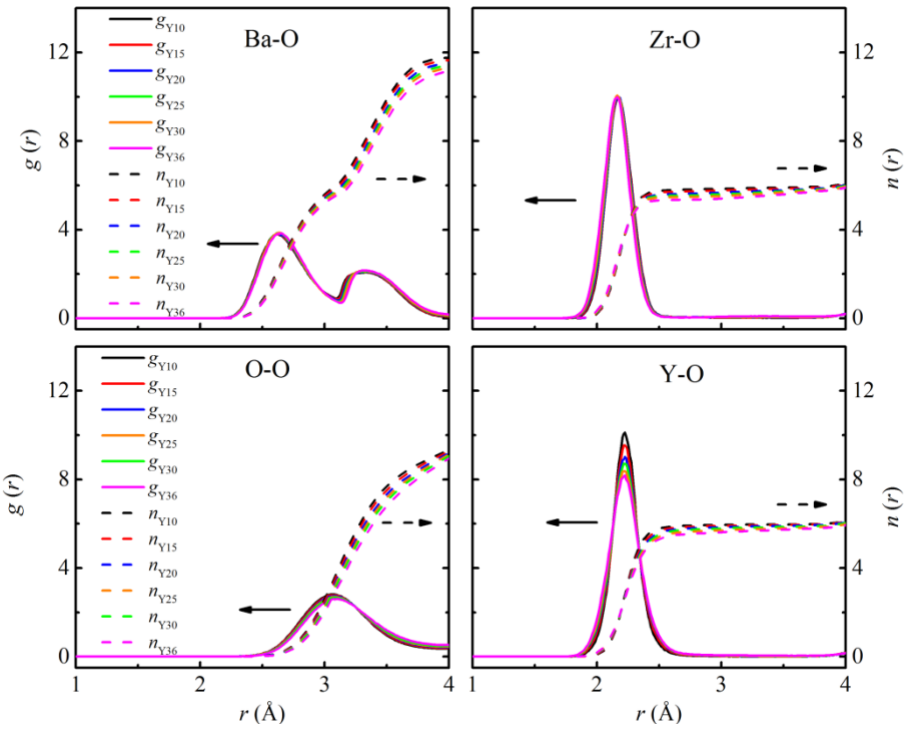
Ba-O
Zr-O
O-O
Y-O
g (r)
n (r)
r (Å)
g_{Y10}
g_{Y15}
g_{Y20}
g_{Y25}
g_{Y30}
g_{Y36}
n_{Y10}
n_{Y15}
n_{Y20}
n_{Y25}
n_{Y30}
n_{Y36}

(a)

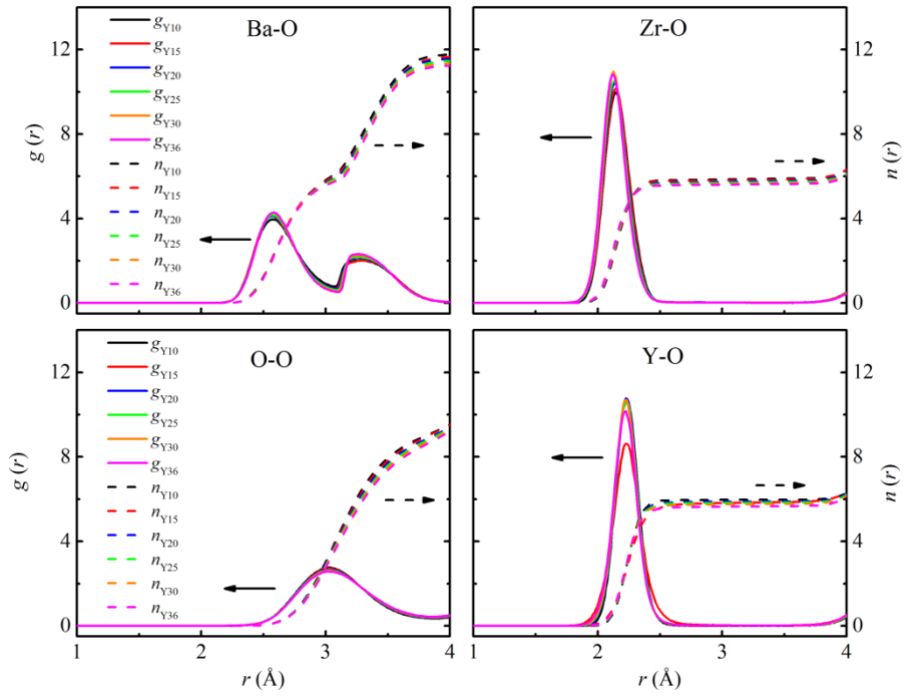
Ba-O
Zr-O
O-O
Y-O
g (r)
n (r)
r (Å)
g_{Y10}
g_{Y15}
g_{Y20}
g_{Y25}
g_{Y30}
g_{Y36}
n_{Y10}
n_{Y15}
n_{Y20}
n_{Y25}
n_{Y30}
n_{Y36}

(b)

Fig. S3 Radial distribution functions g(r) and their integral functions n(r) of Ba-O, Zr-O, O-O and Y-O for (a) Bulk BZY and (b) Disl BZY systems at 1073.15 K

Table S3. The peak positions (Å) of RDFs, CNs and PEs (eV/atom) for Bulk and Disl BZY

System	$R1_{Ba-O}$	$R2_{Ba-O}$	R_{Zr-O}	R_{O-O}	R_{Y-O}	$CN1_{Ba-O}$	$CN2_{Ba-O}$	CN_{Zr-O}	CN_{O-O}	CN_{Y-O}	PE
Bulk Y10	2.625	3.325	2.175	3.065	2.225	6.01	11.84	5.89	9.13	5.94	-7.229
Bulk Y15	2.625	3.335	2.175	3.075	2.225	5.96	11.79	5.86	9.12	5.91	-7.258
Bulk Y20	2.625	3.345	2.165	3.085	2.225	5.85	11.73	5.81	9.03	5.9	-7.282
Bulk Y25	2.635	3.345	2.165	3.075	2.215	5.81	11.66	5.55	8.99	5.87	-7.309
Bulk Y30	2.635	3.335	2.165	3.075	2.225	5.76	11.58	5.48	8.84	5.8	-7.332
Bulk Y36	2.645	3.345	2.165	3.095	2.225	5.67	11.53	5.35	8.68	5.76	-7.355
Disl Y10	2.585	3.305	2.145	3.045	2.235	6.11	11.81	5.86	9.25	5.96	-7.244
Disl Y15	2.565	3.315	2.145	3.025	2.225	6.04	11.71	5.82	9.14	5.93	-7.262
Disl Y20	2.575	3.285	2.135	3.035	2.225	5.96	11.61	5.75	9.01	5.87	-7.321
Disl Y25	2.575	3.275	2.135	3.035	2.225	5.92	11.51	5.69	8.93	5.81	-7.358
Disl Y30	2.575	3.275	2.125	3.035	2.235	5.84	11.41	5.62	8.82	5.73	-7.395
Disl Y36	2.585	3.275	2.115	3.025	2.225	5.8	11.29	5.58	8.79	5.62	-7.433

5.9 Acknowledgements

This work is supported by the “Transformational Technologies for Clean Energy and Demonstration”, Strategic Priority Research Program of the Chinese Academy of Sciences (grant No. XDA21000000), the National Key Research and Development Program of China (grant No. 2018YFB1501002), the Major Project of Qinghai Science and Technology (grant No. 2017-GX-A3), and the China Scholarship Council (grant No. 201706890039). The authors also acknowledge the partnership for an advanced computing environment (PACE) of Georgia institute of technology for computing service. This research used resources of the National Energy Research Scientific Computing Center (NERSC), a U.S. Department of Energy Office of Science User Facility operated under Contract No. DE-AC02-05CH11231.

CHAPTER 6 STRAIN MODULATED IONIC DEFECT CONFIGURATIONS ON CeO_2 (111)

This chapter is a reproduction of published paper with permission from all parties: Zhongkang Han§, Lei Zhang§, Meilin Liu, Maria Verónica Ganduglia-Pirovano*, Yi Gao*, The Structure of Oxygen Vacancies in the Near-Surface of Reduced CeO_2(111) under Strain, ***Frontiers in Chemistry***, 2019. For this chapter, I formulated the original idea and hypothesis, generated and analyzed data, wrote the first version of manuscript, and participated revisions afterwards.

6.1 Abstract

Strain has been widely recognized as important for tuning the behavior of defects in metal oxides since properties such as defect configuration, electronic structure, excess charge localization and local atomic distortions may be affected by surface strain. In CeO_2, the most widely used promoter in three-way catalysts and solid state electrolyte in fuel cells, the behaviors of oxygen vacancies and associated Ce^{3+} polarons are crucial in applications. Recent STM and AFM investigations as well as Density Functional Theory (DFT) calculations have indicated that in the near-surface of CeO_2 (111), at low temperatures and vacancy concentrations, subsurface oxygen vacancies are more stable than surface ones, and the Ce^{3+} ions are next-nearest neighbors (NNN) to both types of vacancies, which can be explained by the better ability of the system to relax the lattice strain induced by vacancy formation as well as by the excess charge localization. The results also revealed that the interaction between first-neighbor vacancies is repulsive. In

this work, the relative stability of surface and subsurface oxygen vacancies at the $CeO_2(111)$ surface under in-plane strain is investigated by means of DFT+U calculations. The tensile strain favors isolated surface vacancies with next nearest neighbor (NNN) polaron configuration, whereas isolated subsurface vacancies with NN polaron configuration are energetically favored under compressive strain. In addition, the formation of both surface and subsurface dimers are favored over having corresponding isolated species under compressive strain, which implies the possibility of controlling the formation of vacancy clusters using strain. In many applications ceria is employed as a supported thin film or within a heterostructure in which ceria can be strained, and this study shows that strain can be a useful handle to tune properties of such materials.

6.2 Introduction

Ceria is widely used as solid oxide fuel cell electrolyte[161] and in catalytic applications[162-165] largely due to its facile oxygen vacancy formation and diffusion, either within the bulk or at its surfaces. It has been previously reported,[166] and later supported by subsequent research,[60, 167-171] that the formation of an intrinsic neutral oxygen vacancy in ceria is accompanied by the formation of two nearby polarons (Ce^{3+} or Ce'_{Ce} in the Kröger-Vink notation), which results from the transfer of two electrons originally residing in $2p$ states of the missing oxygen ion to Ce $4f$ states of two cations. For oxygen vacancies in the near-surface of $CeO_2(111)$, it has been predicted from DFT calculations that the two Ce^{3+} polarons are not necessarily NN (Nearest-Neighbor) to the oxygen vacancies, but rather prefer to locate at NNN (Next-Nearest-Neighbor) cationic sites,[60, 170] which has been later validated in Scanning Tunneling Microscope (STM)

experiments.[171] The preference for the NNN positions upon localization of the excess charge has been explained by the better ability of the system to relax the lattice strain induced by the presence of the vacancies as well as by the excess charge localization; a Ce^{3+} ion is more spacious than its Ce^{4+} counterpart and at NN sites Ce^{3+}–O bonds would be compressed.[60] Moreover, the preferred sites for oxygen vacancies in the near-surface of CeO_2(111),[60, 170-176] as well as the type of interactions between them,[172, 174, 175, 177-181] have also been assessed. Under zero applied stress, isolated subsurface vacancies are more stable than surface ones, and the interaction between nearest neighbor vacancies at the surface or in the subsurface is repulsive.

As for isolated oxygen vacancies in bulk ceria, most theoretical studies reported that the NNN Ce^{3+} locations are also preferred under zero applied stress,[182-187] i.e., at the calculated equilibrium volume of CeO_2. Moreover, it has been demonstrated that the ground-state configuration varies whether tensile or compressive stress is applied,[188] namely, at large volumes, both Ce^{3+} ions are in the second coordination sphere of the vacancy, and at small volumes, they are in the first. Additionally, it has been experimentally found that the lattice parameter of reduced ceria in the fluorite-type cubic structure is expanded,[189] which has been consistently reproduced in DFT calculations[188]; the averaged lattice parameter over different configurations for the pair of Ce^{3+}'s is slightly larger than the equilibrium lattice parameter of perfect ceria.

Furthermore, for doped ceria with 3-valent dopants,[187, 190, 191] the dependence of the location of the dopants on the dopant's ionic radius has been reported, in which larger ions such as La prefer NNN sites to vacancies, and smaller ions such as Gd prefer

NN sites. It has been argued that it is the balance between repulsive elastic and attractive electronic contributions to the interaction between dopants and vacancies which determines the NN or NNN site preference,[191] and, as in the case of undoped ceria mentioned above, applied tensile or compressive stress can change the site preferences.[190] In addition, changes in the lattice parameter upon ceria doping have been reported, as, for example, the one of Gd-doped ceria[192, 193] that shows a maximum as a function of Gd content.

Strain in ceria has received considerable attention because oxygen vacancy migration can be modified through strain, which is most relevant for tuning ion conduction in ceria-based applications.[194, 195] It is fair to say that it is practically inevitable to avoid that ceria surfaces will experience strain effects, either induced by the lattice mismatch when created as a thin film on a substrate,[196, 197] or when reduced,[187] due to the higher stability of oxygen vacancies in the near-surface as compared to deeper layers[172, 173, 197, 198] that is accompanied by the formation of Ce^{3+} ions which induces a near-surface lattice expansion. For reduced ceria nanoparticles, mainly expansions of the lattice have been observed that are associated to the presence of Ce^{3+} cations,[58, 185, 189, 190] but also lattice contractions have been reported[190] that are attributed to the additional pressure caused by the surface tension between the crystallite and the ambient atmosphere as the nanoparticle size decreases. Despite these efforts, the effect on the defect structure of the reduced ceria (111) surface of applying a tensile or compressive stress has not yet been comprehensively studied.

In this article, using density functional theory (DFT)-based methods, we systematically investigate the effect of applied stress on the reduced CeO_2(111) surface and

address how strain affects the relative stability of isolated surface and subsurface oxygen vacancies, the formation of vacancy pairs, and the localization of the excess charge. It turns out that, depending on strain, surface vacancies can be more stable than subsurface ones, the interaction between first nearest neighbor vacancies in the near-surface can be attractive, and different localized charge distributions can be attained.

6.3 Methodology

First-principles spin-polarized density functional theory (DFT)-based calculations were carried out employing the VASP (Vienna *Ab-initio* Simulation Package) code. The DFT+*U* methodology[192] was used with the generalized gradient approximation (GGA) of Perdew-Burke-Ernzerhof (PBE)[199] and an effective *U* value of 5.0 eV. The value of the *U* parameter –necessary to describe localized electrons associated to Ce^{3+} ions– lies within the range of suitable values to describe reduced ceria-based systems.[200] We used projector augmented wave (PAW) potentials[201] with Ce (4*f*, 5*s*, 5*p*, 5*d*, 6*s*) and O (2*s*, 2*p*) electrons as valence states, and a plane-wave cutoff of 400 eV. The CeO_2 (111) surface was modeled using three O-Ce-O trilayers separated by 15 Å vacuum space (i.e., a nine atomic layer slab) with both 5×5 and 2×2 periodicities. A $1 \times 1 \times 1$ ($3 \times 3 \times 1$) Gamma-centered Monkhorst-Pack grid was used for the *k*-point sampling of the Brillouin zone of the 5×5 (2×2) slab. Stress ranging from –5% (compressive) to +5% (tensile) has been applied to the ceria (111) surface, i.e., to the two vectors which define the surface unit cell. It should be mentioned that for compressive stress, experiments show that CeO_2 transforms from a cubic fluorite-type structure to an orthorhombic cotunnite-type ($PbCl_2$) structure at a pressure of 31 GPa.[202] However, in this study, the underlying fluorite

lattice is prevented from undergoing a phase transition. In all geometry optimizations, all atoms in the bottom trilayer were kept fixed, whereas the rest of the atoms were allowed to fully relax. For all strained surfaces, the interlayer spacings within the bottom trilayer correspond to those of a bulk-truncated $CeO_2(111)$ under zero stress, and the in-plane atom positions correspond to those in the corresponding strained CeO_2 bulk.

To systematically investigate how strain affects the relative stability of isolated surface and subsurface oxygen vacancies in the near-surface of $CeO_2(111)$ as well as the formation of vacancy pairs, and the localization of the excess charge, reduced strained slabs were created. Isolated surface and subsurface vacancies with different configurations for the Ce^{3+}'s were considered with both 5×5 and 2×2 periodicities. Vacancies were placed near the surface, i.e., within the outermost trilayer, and the Ce^{3+}'s within the (two) outermost cationic plane(s) for the 5×5 (2×2) periodicity. Moreover, using the larger 5×5 surface unit cell, nearest and next-nearest neighbor surface and subsurface vacancy pairs with various configurations for the Ce^{3+}'s were considered. In order to obtain distinct configurations of the reduced Ce^{3+} sites, a two-step relaxation procedure was applied. In the first step, we replaced the selected Ce^{4+} by Ce^{3+} ions, i.e., for the latter we used PAW potentials for which the $4f^1$ state was moved to the core, and performed non-spin polarized calculations. The so-obtained relaxed structure was further optimized using the regular Ce^{4+} PAW potentials and spin-DFT. We limit the discussion to high-spin states because the difference between these states and any other spin state is less than 0.01 eV.[203]

6.4 Results and discussion

We have modeled the reduced $CeO_2(111)$ surface by removing one surface (SSV) or subsurface (SSSV) vacancy from a supercell with 5×5 and 2×2 periodicities, as shown in Figure 45 and Figure 46, respectively. Nearest (NN) and next-nearest neighbor (NNN) Ce ions to vacancies are labelled with uppercase letters (A, B, C, D, …) and numerals (1, 2, 3, 4, …), respectively. Employing the larger supercell, first-neighbor surface and subsurface vacancy pairs (SurDimer and SubDimer), as well as corresponding pairs with a vacancy separation corresponding to that of third-nearest neighbors in the oxygen plane (SurDimer-d and SubDimer-d), have also been considered (cf. Figure 46). Stress ranging from −5% (compressive) to +5% (tensile) has been applied to both supercells as mentioned in Sec. 5.3. It is known that under zero applied stress, NNN sites in the outermost cerium layer are the energetically preferred locations of the Ce^{3+} ions, but they would rather be in NNN sites of a deeper layer than next to a vacancy in the outermost one. Since under applied stress, preferences may change, for the strained surfaces with 5×5 (Table S1-S7) or 2×2 (Table S8) periodicity, vacancy structures corresponding to the most relevant combinations of the possible locations of the Ce^{3+} ions have been considered.

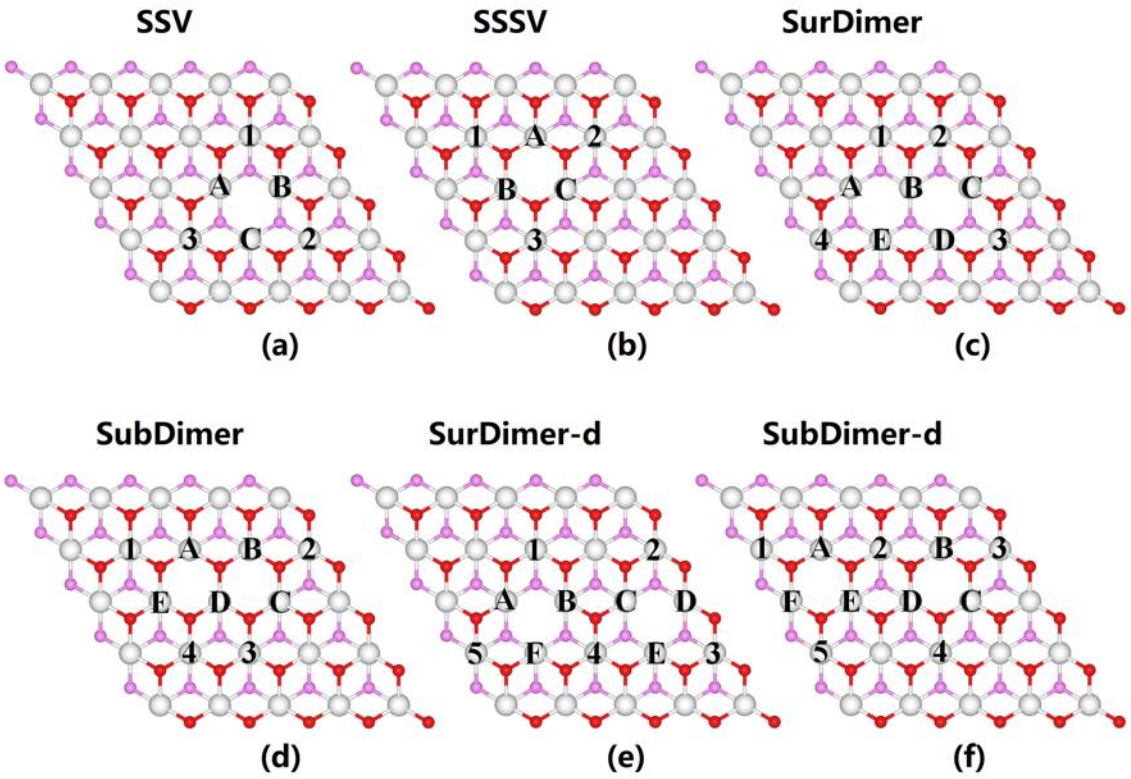

Figure 45 Structural model of the $CeO_2(111)$ unit cell with 5 × 5 periodicity. (a) single surface vacancy, SSV, (b) single subsurface vacancy, SSSV, (c) nearest neighbor surface oxygen vacancy dimer, SurDimer, (d) nearest neighbor subsurface oxygen vacancy dimer, SubDimer, and (e) third-nearest neighbor surface oxygen vacancy pair, SurDimer-d. (f) third-nearest neighbor surface oxygen vacancy pair, SubDimer-d. Ce cations in the outermost trilayer are shown as white balls. Surface and subsurface oxygen atoms are shown as red and pink balls, respectively. The labelled cerium atoms denote possible Ce^{3+} locations on nearest-neighbor (A, B, C, D….) or next-nearest-neighbor (1, 2, 3, 4….) sites to the vacancies. Only the three outermost atomic layers are shown for simplicity.

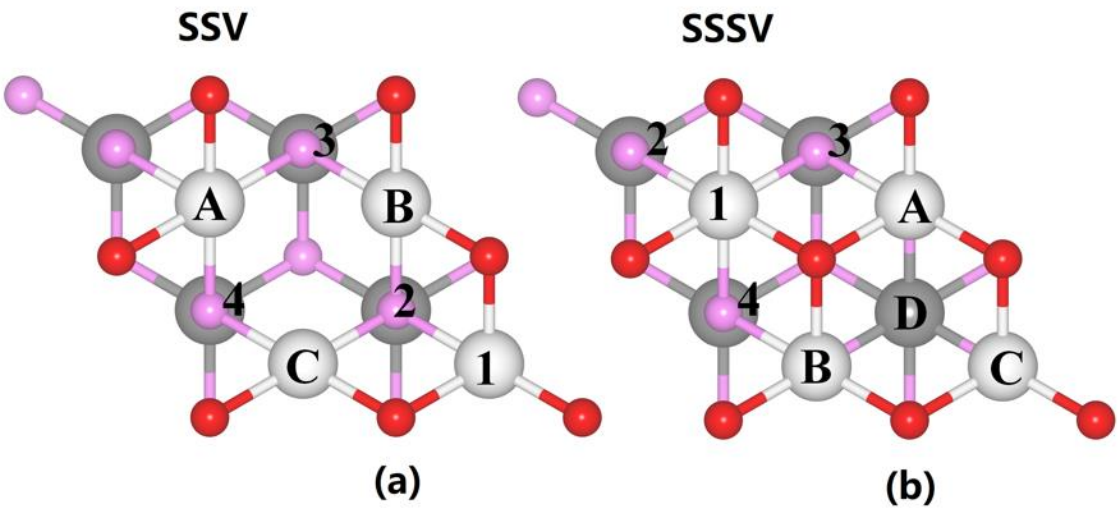

Figure 46 Structural model of the $CeO_2(111)$ unit cell with $\mathbf{2 \times 2}$ periodicity. (a) single surface vacancy, SSV, and (b) single subsurface vacancy, SSSV. The color scheme for atoms and vacancies corresponds to that used in Figure 45. The labelling scheme for the cations also corresponds to that in Figure 45. Only the five outermost atomic layers are shown for simplicity.

The averaged vacancy formation energy (E_f) was calculated as:

$$E_f = \frac{1}{n}[E_{defect} + \frac{n}{2}E_{O_2} - E_{perfect}]$$

where E_{defect} and $E_{perfect}$ are the total energies of the (relaxed) defective (reduced) and perfect (clean) slabs, respectively, *n* is the number of oxygen vacancies, and E_{O_2} is the total energy of the isolated O_2 molecule in its triplet ground state.

6.4.1 Low vacancy concentration

Figure 47 and Figure 48 summarize the calculated vacancy formation energy for all 5×5 structures with a SSV and a SSSV vacancy, respectively. For the surface vacancy, configurations with both Ce^{3+} ions in the outermost cationic plane and either in the first coordination shell (AB), in the second (12), or one in each shell (1C) were considered (cf.

Figure 45). In addition, a configuration with both Ce^{3+} ions in the second coordination shell, but one in the outermost cationic plane and the other one in the plane beneath, was considered (1S) (cf. Fig. S1). Under 0% tension, the 12 configuration is by 0.23 eV more stable than the AB one, in line with previous works (Figure 47).[60, 170, 172] As the tensile strain is increased from 0% to +5%, the 12 >1C >1S >AB stability trend does not change although the difference between the most stable configuration (12) and the least stable one (AB) becomes larger (0.33 eV under +5% strain, Table S1). In contrast, if we look at the surface under large compressive strain (≥ –5%), the trend is reversed, i.e. AB >1C>12; (the 1S configuration is not stable); under –5% strain, the configuration with both Ce^{3+} ions in the first coordination shell (AB) is by 0.12 eV more stable than that with the Ce^{3+} ions in the second coordination shell (12).

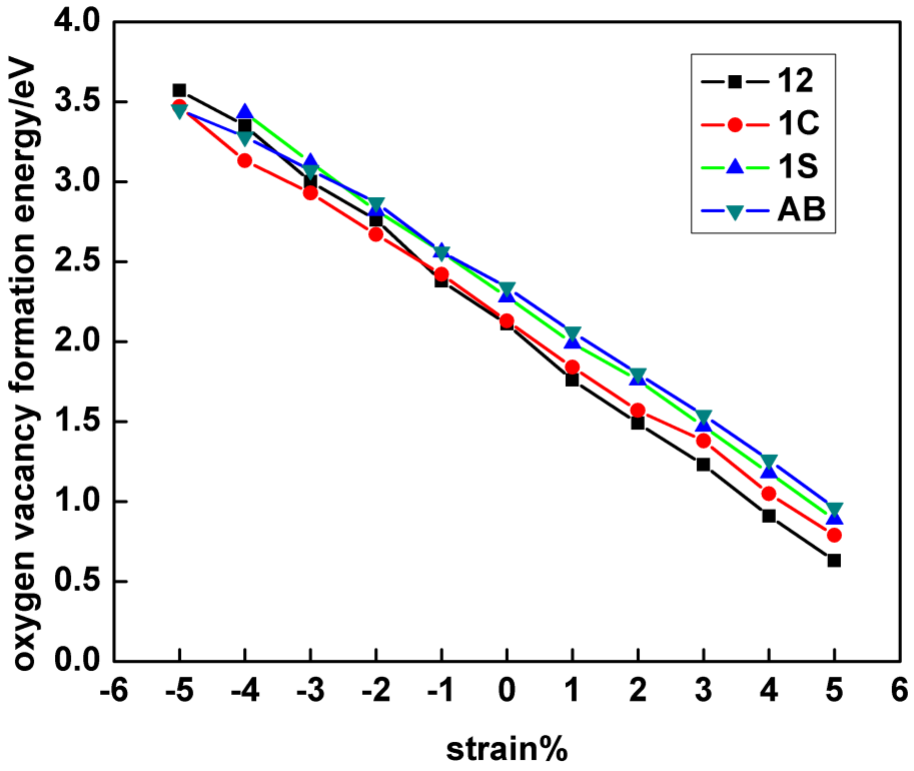

Figure 47 Single surface oxygen vacancy (SSV) formation energy at the 5×5 $CeO_2(111)$ surface as a function of strain and for distinct polaronic structures, which are labeled according to the location of the two Ce^{3+} as shown in Figure 45.

For the subsurface vacancy, configurations with both Ce^{3+} ions in the outermost cationic plane and either in the first coordination shell (AB) or in the second (12), or one in each shell (1C) were considered (cf. Figure 45). In addition, a configuration with both Ce^{3+} ions in the first coordination shell, but one in the outermost cationic plane and the other one in the plane beneath, was considered (1S) (cf. Fig. S1). The behavior of the SSSV is comparable to that of the SSV, although the slope of the energy-strain curve for SSSV is somewhat smaller than that of the SSV (cf. Figure 47 and Figure 48). Under 0% tension, the 12 configuration is by 0.32 eV more stable than the AB one, in line with previous works

(Figure 48).[60, 170, 172] The 12 >1C >1S >AB stability trend obtained under 0% tension, does not change upon increasing the tensile strain from 0% to +4% (the AB configuration is not stable under +5% strain), but the difference between the 12 and AB configurations becomes larger by (0.42 eV under +4% strain, Table S2). If the surface is compressed, for example, by –5%, the most stable configuration has both Ce^{3+} ions in the first coordination shell (AB) and that with the Ce^{3+} ions in the second coordination shell (12) is by 0.07 eV less stable.

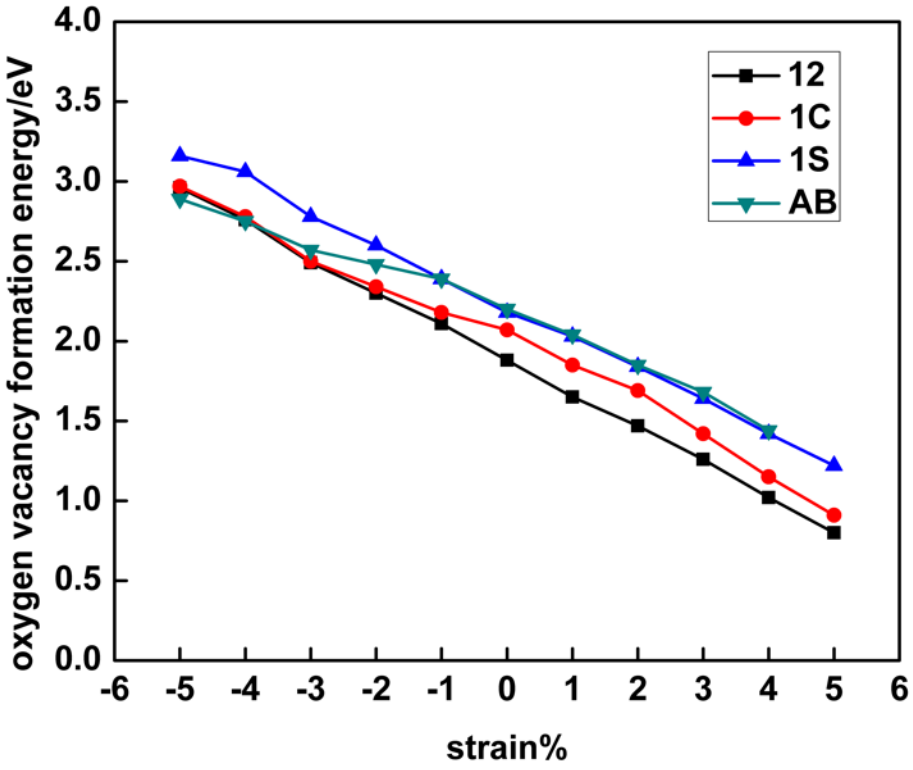

Figure 48 Single subsurface oxygen vacancy (SSSV) formation energy at the 5×5 $CeO_2(111)$ surface as a function of strain and for distinct polaronic structures, which are labeled according to the location of the two Ce^{3+} as shown in Figure 45.

Before analyzing the origin of the observed transitions between NNN-NNN (12) and NN-NN (AB) Ce^{3+} configurations of both SSV and SSSV vacancy types under large compressive strain, we first discuss how the relative stability between the SSV and SSSV is influenced by strain. Figure 49 collects the results of the most stable SSV and SSSV configurations for each value of the applied stress (cf. Figure 47 and Figure 48, and Tables S1, S2 and S7). In agreement with the literature,[60, 170, 172] we find that under 0% tension, the subsurface vacancy position is by 0.23 eV more stable than the surface one. Under compressive strain, from 0% to –5%, the SSSV remains more stable than the SSV, but the difference becomes larger as the compression increases, for example, under –5% compression the SSSV is by 0.56 eV more stable than the SSV. However, as the tensile tension increases from +3%, the relative stability reverses and the SSV becomes more stable.

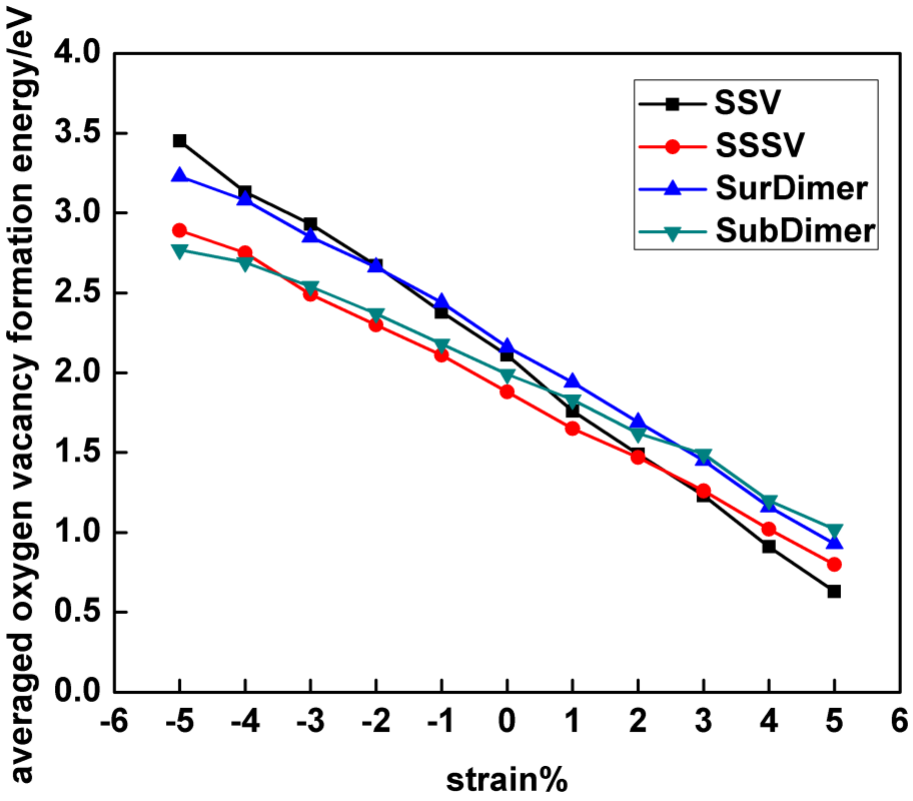

Figure 49 The averaged oxygen vacancy formation energy of the most stable SSV, SSSV, SurDimer, and SubDimer structures with 5 × 5 periodicity as a function of strain.

As vacancy-induced lattice relaxations are known to play an important role in the stabilization of both a particular Ce^{3+} configuration and the subsurface vacancy position in the near-surface of CeO_2(111),[60, 170] we analyze their effects on the strained surfaces. To this end, we define two contributions to the vacancy formation energy, $E_f = E_b + E_r$, namely, the bond breaking energy, E_b, as the energy cost to create the vacancy without allowing for lattice relaxations, i.e., $E_b = E_{defect}^{unrelax} + \frac{1}{2}E_{O_2} - E_{perfect}$, and the gain in relaxation energy, E_r, i.e., $E_r = E_{defect}^{relax} - E_{defect}^{unrelax}$. In Figure 50 and Table S9, we show how these different contributions depend on strain. For both SSV and SSSV, E_b is largest

for the highest compression and smallest for the largest tensile stress, i.e., the correlation between E_b and strain is negative. To create unrelaxed surface and subsurface oxygen vacancies, three Ce–O_s and four Ce–O_{ss} bonds, respectively, have to be cut. For the SSV, the Ce_1–O_s bond lengths (Ce_1 and O_s are in the outermost cationic and anionic layers, respectively) vary from 2.30 Å to 2.43 Å as the stress changes from –5% to +5% (Table 1), thus, the observed E_b vs. strain trend is in line with the weakening of the bonds upon increasing tensile strain. For the SSSV, the corresponding variations in the three Ce_1–O_{ss} bonds are practically identical to those of the SSV, but that of the Ce_2–O_{ss} bond (Ce_2 and O_{ss} are in the second cationic and anionic layers, respectively) is contracted from 2.52 (–5%) to 2.26 (+5%). In any case, the observed E_b vs. strain trend for the SSSV vacancy is in line with the weakening of the average Ce–O_{ss} bond length upon increasing tensile strain, which varies from 2.35 (–5%) to 2.40 (+5%). Moreover, we observe that the E_b vs. strain curves for both the SSV and the SSSV resemble straight lines but with a different slope, i.e. the curves cross; the difference between the E_b values is largest for the largest tensile stress and becomes smaller as the surface is compressed. Under the largest tensile strain (+5%), three Ce_1–O_s bonds of 2.43 Å for the SSV have to be cut (Table 2), whereas for the SSSV there are three Ce_1–O_{ss} bonds of 2.45 Å and one particularly strong Ce_2–O_{ss} bond of 2.26 Å; hence, creating an unrelaxed SSV is preferred. As already mentioned, upon compression the Ce_2–O_{ss} bond expands in such a way that for the largest compressive strain (–5%), three Ce–O_s bonds with an average distance of 2.30 Å and four Ce–O_{ss} ones of 2.35 Å have to be cut to create an unrelaxed SSV and SSSV, respectively (Table 2); the latter seems to be energetically preferable.

Table 2 O–Ce bond lengths (in Å) between a surface oxygen atom at the strained $CeO_2(111)$ surface (5×5 periodicity), O_s, and its three nearest neighbor cerium atoms in the outermost cerium layer, Ce_1, as well as between a subsurface oxygen atom, O_{ss}, and its three (one) nearest neighbor cerium atoms in the first (second) cerium layer, Ce_1 (Ce_2).

Strain %	–5	–4	–3	–2	–1	0	+1	+2	+3	+4	+5
O_s–Ce_1	2.30	2.31	2.32	2.33	2.35	2.36	2.37	2.39	2.40	2.41	2.43
O_{ss}–Ce_1	2.29	2.30	2.32	2.33	2.35	2.36	2.38	2.40	2.41	2.43	2.45
O_{ss}–Ce_2	2.52	2.48	2.45	2.42	2.40	2.37	2.35	2.33	2.31	2.29	2.26

In Figure 50 we also compare the relaxation energy gain, E_r (< 0), to the vacancies formation energy as a function of surface strain; the E_r vs. strain curves also resemble straight lines with a different slope for the SSV and SSSV, but the curves do not cross within the interval of –5% to +5% strain values. The lattice relaxations are the result of both the presence of the oxygen vacancy to which, for example, the O ions of the first oxygen coordination shell tend to move towards the vacancy, whereas the Ce ions of the first cationic coordination shell move away from the vacancy, and the localization of the excess charge driving the $Ce^{4+} \rightarrow Ce^{3+}$ reduction of two cations. For isolated oxygen vacancies in bulk ceria under strain,[195] it has been shown that the energy gained due to the displacements of the atoms upon relaxation increases almost linearly with increasing the tensile stress, independent of the sites on which the excess charge is localized, but the

gain is more pronounced when the localization occurs at NNN cationic sites to the vacancy. Similarly, for both SSV and SSSV vacancies in the near-surface of CeO_2 (111), the relaxation energy gain is smallest for the biggest compressive strain and largest for the highest tensile stress, i.e., the correlation between the absolute value of E_r and strain is positive; the energy gain is always largest for the SSSV within the –5% to +5% strain interval. We can try to rationalize the larger gain in relaxation energy of the SSSV by noticing first that the number of neighboring O and Ce ions that will be displaced upon the creation of a SSSV are larger than the corresponding ones for a SSV. Moreover, for the SSSV and SSV unrelaxed structures, the two excess electrons are equally shared by four and three NN Ce ions, respectively; i.e., the excess electrons are ‘‘delocalized’’ over all NN cations, and the relaxation energy gain due to the $4\times Ce^{0.5+} \rightarrow 2\times Ce^{3+}$ charge localization for the SSSV is larger than the $3\times Ce^{0.\widehat{6}+} \rightarrow 2\times Ce^{3+}$ one for the SSV. Furthermore, with respect to the above-mentioned smaller gain in the relaxation energy under compressive strain, we recall here –and address below– that the Ce^{3+} ions in the first coordination sphere are preferred when the surface is substantially compressed and then, it is expected that the contribution associated with the relocation of electrons will be lower when it occurs between first neighbors.

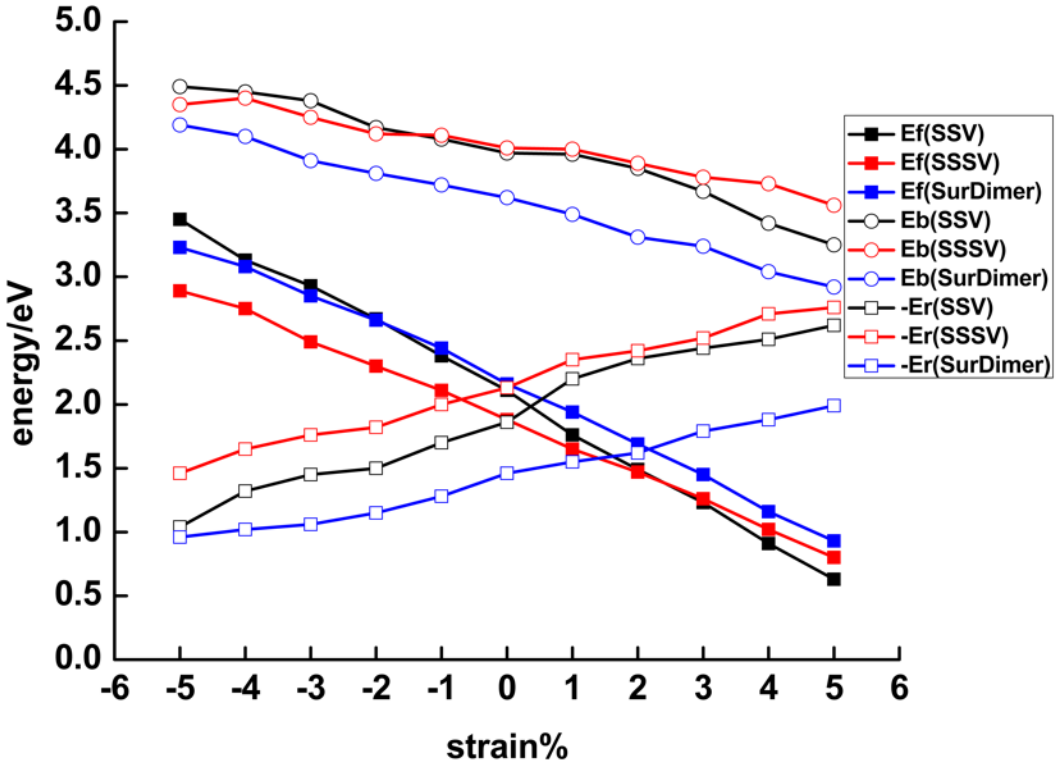

Figure 50 The near-surface oxygen vacancy formation energy, $E_f = E_b + E_r$, as a function of strain (5 × 5 periodicity). E_b is the energy cost to create a near-surface oxygen vacancy without allowing for lattice relaxations, i.e., the bond breaking energy, and E_r, the gain in relaxation energy.

Summarizing, there is an almost linear correlation between both contributions to the oxygen vacancy formation and the surface strain. The correlation between the bond breaking energy, E_b, and strain is negative and that between the absolute gain in relaxation energy, $-E_r$, and strain is positive. The slopes of the almost linear E_b vs. strain and E_r vs. strain relationships are not the same for the SSV than for the SSSV. The preference for the SSSV under compressive strain and for the SSV under tensile strain (> 3%) is the result of the different behaviors of the contributions to create the corresponding vacancies with

strain. For example, for the –5% compressed surface, both E_b and E_r favor the SSSV by 0.14 eV and 0.42 eV, respectively, and thus, the SSSV is by 0.56 eV more stable than the SSV. However, for the +5% strained surface, E_b favors the SSV by 0.31 eV and E_r the SSSV by 0.14 eV, and, as a result, the SSV is by 0.17 eV more stable than the SSSV.

The effects of strain on the distribution of the excess charge are also reflected in the calculated densities of states (DOS). The formation of a pair of Ce^{3+} ions upon the creation of an oxygen vacancy results in the appearance of new (defect or polaron) states belonging to the Ce 4*f* states in the O_{2p}–Ce_{5d} gap below the Fermi level[61]; the vacant 4*f* states lie in this gap. The knowledge of the precise positions of the defect states is important because the properties exhibited by the vacancies, such as the possibility to transfer electrons to adsorbed molecules, depend on them. The densities of states (DOS) for the example of a SSV with the Ce^{3+}'s in either the 12, 1C or AB configuration under –5%, 0% or+5% strain (Figure 51) is discussed in the following. If the two Ce^{3+} ions occupy different cationic shells around the vacancy, the resulting variation in the chemical environment leads to a splitting of the filled Ce^{3+} *f* levels, which could be detected with STM spectroscopy.[61] In the 12 configuration, the two next-nearest neighbor Ce^{3+} ions have equal coordination number (CN=7) and filled *f* orbitals with the same energy as they experience the same chemical environment, and hence no splitting of the *f* orbitals is expected; this is certainly observed for the 12 configurations within the –5% to +5% strain range (Figure 51, Table S10). Similarly, for the AB configuration with the two Ce^{3+} ions in nearest neighbor sites, and experiencing the same chemical environment (CN=6), no splitting of the *f* orbitals is expected. However, two peaks are observed in the DOS for –5%

compression with a splitting of the order of 0.16 eV. The reason for the splitting is not that the Ce^{3+} are located in different environments but a hybridization of the polaronic states, which causes a spread of charges across both adjacent sites. That is, the polarons are no longer fully localized in one specific Ce site, rather, the polaronic charge is shared between the two sites in a sort of bonding/anti-bonding configuration (cf. isosurfaces in Fig. S2). Finally, as it is expected, for the 1C configuration with one nearest and one next-nearest Ce^{3+} (CN=6 and 7, respectively), we find a splitting of the *f* orbitals due to the different distances from the vacancy of the order of 0.1 eV for –5% and 0% strain, but increases to about 0.2 eV for +5% tensile strain (Table S10).

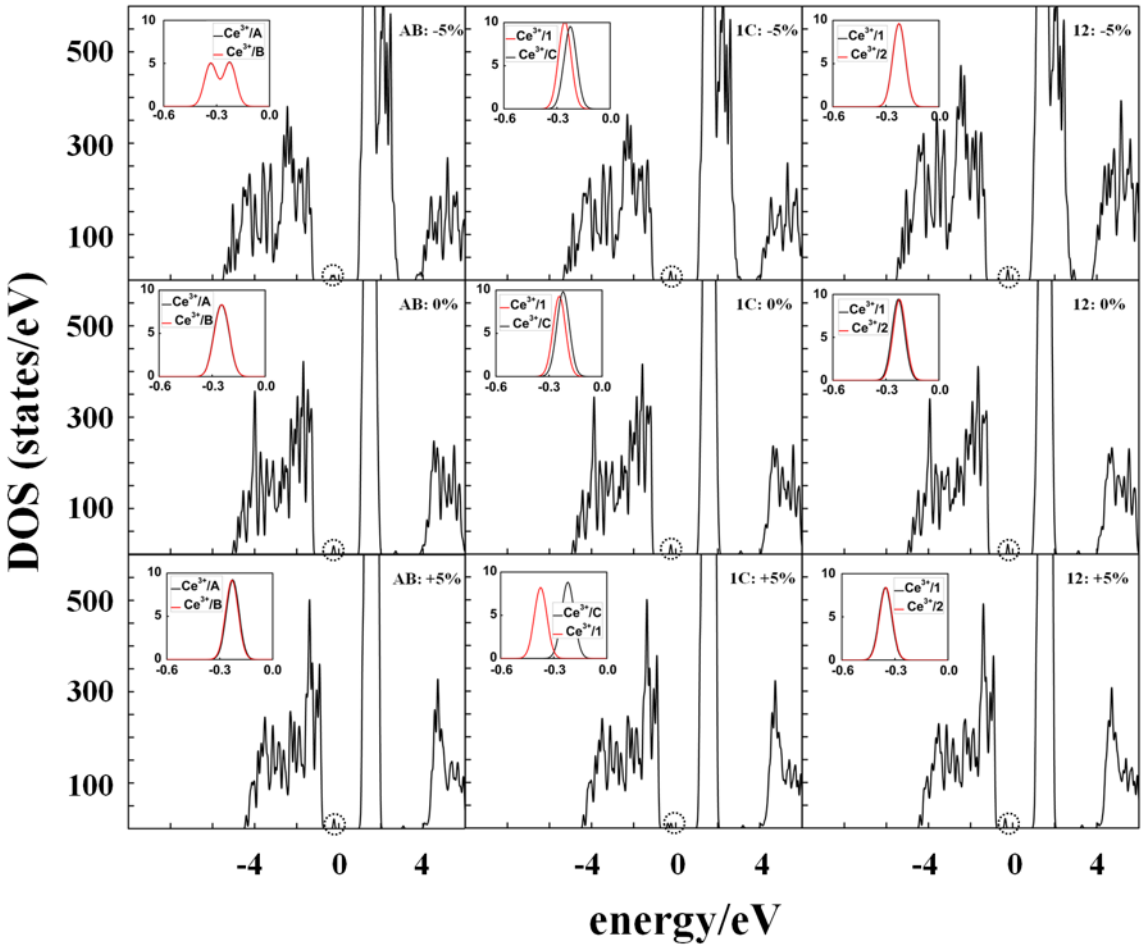

Figure 51 Densities of states (DOS) summed over spin projections and all atoms for a SSV under −5%, 0% and +5% strain with different Ce^{3+} configurations, namely, AB, 1C and 12 and 5×5 periodicity. The Fermi level is set as the zero energy value, below which the states are occupied. The occupied Ce 4*f* states are marked with black dashed circles, which are shown magnified in insets.

Before discussing the position of the occupied *f* states in the O_{2p}–Ce_{5d} gap below the Fermi level, we observe that the calculated O_{2p}–Ce_{5d} gap value of 5.11 eV for 0% strain is close to the previously reported PBE+*U* bulk value (5.3 eV[204]); the calculations underestimate the bulk value of 6.0 eV obtained from electron-energy loss and optical spectroscopy.[205] The top of the valence band and the bottom of the conduction band, which are formed predominantly by O 2*p* and Ce 5*d* states, respectively (empty *f* states lie in between), do change their positions when strain is applied, but both compressive and tensile strain decrease the O_{2p}–Ce_{5d} gap (Table S10). Moreover, we notice (Figure 51) that the width of the valence band widens (shrinks) as the lattice is compressed (expanded). The position of the occupied *f* states, reported as O_{2p}–Ce_{4f} (the difference between the eigenvalue of the lowest occupied *f* state and the top of the valence band, which is formed predominantly by O 2*p* states), varies with applied strain; as the strain varies from −5% to +5%, the occupied *f* states are shifted toward the valence band, in turn reducing the values of O_{2p}–Ce_{4f}, and therefore they are shifted away from the conduction band.

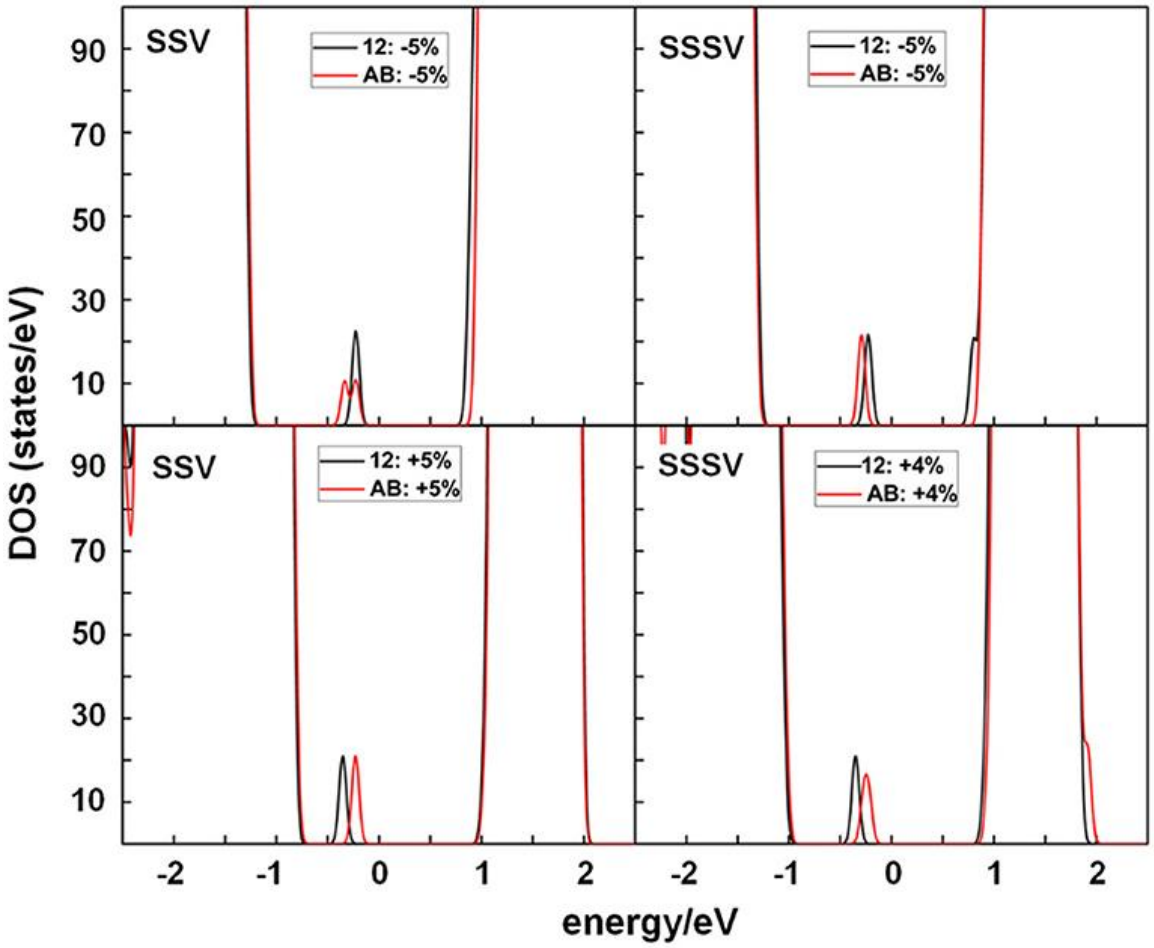

Figure 52 Densities of states (DOS) summed over spin projections and all atoms for a SSV and SSSV under −5%, and +5%, or +4% strain with AB and 12 Ce^{3+} configurations and 5×5 periodicity. The Fermi level is set as the zero energy value, below which the states are occupied.

The polarons states lie at different energies in the O_{2p}–Ce_{5d} gap region which depend on the type of configuration (AB, 1C or 12) and on the type of applied strain (compressive or tensile). Therefore, the above observed changes in the relative stability of the NN-NN (AB) and NNN-NNN (12) Ce^{3+} configurations for both SSV and SSSV vacancy types (cf. Figure 47 and Figure 48) under varying strain, i.e., AB configurations are stable under large compressive strain whereas 12 ones are stable otherwise, should be correlated with the specific locations of the corresponding polaron states in the gap. Figure

52 directly compares the total DOS of the AB and 12 configurations for the example of the SSV under ±5% strain and shows that under surface compression (–5%), the characteristic polaron peaks of the AB configuration lie lower in energy than those of the 12 one, whereas under surface expansion (+5%), the situation is reversed. The driving force for the Ce^{3+} preference in favor of the first (second) coordination shell of the vacancies under compressive (tensile) strain is the better ability of the system to relax the lattice strain in the preferred configuration.

6.4.2 High vacancy concentration

In this section we analyze the results for a SSV and a SSSV in the near-surface of CeO_2(111) under strain with 2×2 periodicity (Figure 53, Table S8), and compare to those obtained with the 5×5 unit cell. In the 2×2 unit cell under zero applied stress, the most stable SSV and SSSV configurations have both Ce^{3+} ions in NNN sites, one in the outermost cationic layer, and the other in the layer beneath, i.e., both configurations are labeled as 14 (cf. Figure 46), in line with previous calculations.[79] These SSV (14) and the SSSV (14) configurations are by 0.22 eV and 0.54 eV more stable, respectively, than the corresponding ones with the Ce^{3+} ions in NN sites (AB). We note that at the lower vacancy concentration (5×5 unit cell) and zero applied stress, the SSV and the SSSV configurations with both Ce^{3+} ions in the second coordination shell (12) are by 0.23 and 0.32 eV more stable, respectively, than the corresponding ones with Ce^{3+} ions in the first coordination shell (AB). For the SSV and SSSV oxygen vacancies with 2×2 periodicity under 0% strain, the 14 >1B >AB and 14 > 1A ≈ 1D > AD ≈ AB stability trends, respectively, are obtained (Table S8).[60, 79] As the tensile strain is increased from 0% to

+5%, the SSV- and SSSV-14 configurations remain more stable with respect to the corresponding AB ones. For example, for the +5% stretched surface, the SSV- and SSSV-14 configurations are by 0.23 eV and 0.53 eV more stable, respectively, than the corresponding SSV- and SSSV-AB ones (Figure 53, Table S8). However, in line with the results for the lower vacancy concentration (5×5 unit cell), for both vacancy types under compressive strain, an increasing preference for configurations with both Ce^{3+} ions in the first coordination shell (AB) is observed. For example, for –5% strain, the SSV-AB configuration is by 0.16 eV more stable than the SSV-14 (Figure 53, Table S8); for the SSSV, an even larger compressive strain would be needed to observe the crossing between the AB and 14 configurations (cf. Figure 53), but the tendency is clear. In summary, for both vacancy concentrations, the ground-state configuration of both vacancy types varies whether tensile or compressive stress is applied, namely, under tensile strain, both Ce^{3+} ions do *not* prefer the first coordination sphere of the vacancy, but under large compressive strain they do.

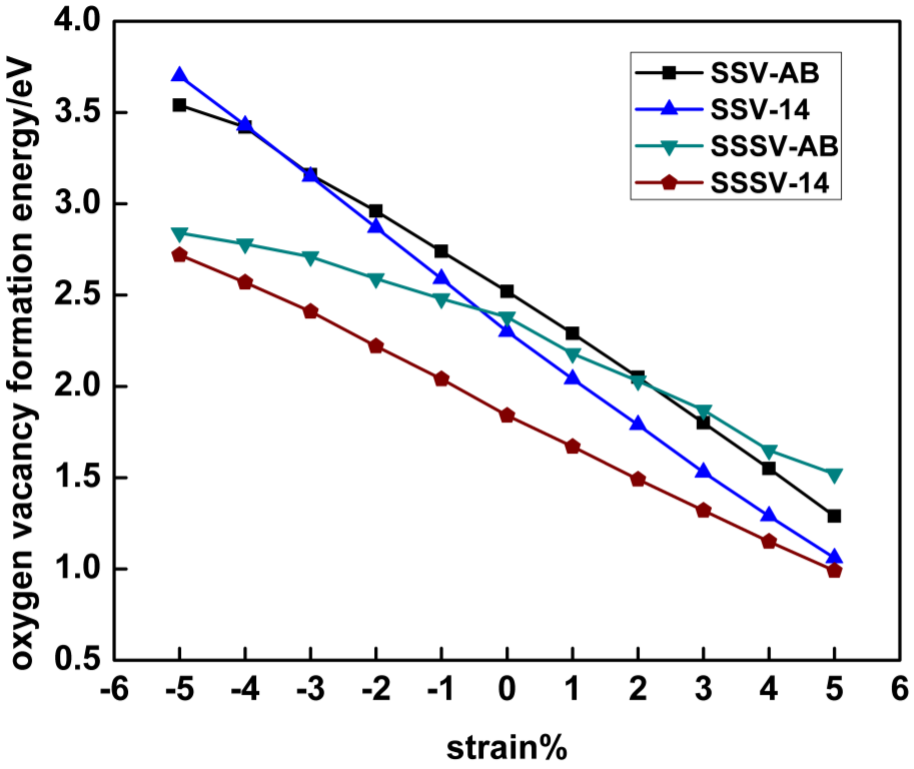

Figure 53 Oxygen vacancy formation energy for single surface (SSV) and subsurface (SSSV) vacancies at the 2 × 2 CeO_2(111) surface as a function of strain and for distinct polaronic structures, which are labeled according to the location of the two Ce^{3+} as shown in Figure 46.

With respect to the relative stability between the SSV and SSSV when stress is applied and the concentration of vacancies is larger (Figure 53), a behavior very similar to that already discussed for the case of low concentration is observed (cf., Fig. S3 and Figure 49). In agreement with the literature,[60, 170, 172] we find that under 0% tension, the subsurface vacancy position is by 0.46 eV more stable than the surface one; at the lower vacancy concentration the difference is by a factor of two smaller. Under compressive strain, from 0% to –5%, the SSSV remains more stable than the SSV, but the difference becomes larger as the compression increases, for example, under –5% compression, the SSSV is by 0.82 eV more stable than the SSV. However, under tensile strain, the larger

relative stability of the SSSV as compared to the SSV becomes smaller and smaller as the strain increases from 0% to +5%, but an even larger tensile strain would be needed to observe the crossing between the E_f vs. strain curves; at the lower vacancy concentration the crossover occurs at about +3% strain (cf. Figure 50). For the higher vacancy concentration, we have also evaluated the bond breaking, E_b, and the relaxation energy, E_r, contributions to the vacancies formation energies as a function of surface strain (Fig. S3 Table S11), which behave similarly to the case of the lower vacancy concentration discussed above. Both contributions resemble straight lines with a different slope for the SSV and SSSV, and the correlation between E_b and strain is negative, whereas that between $-E_r$ and strain is positive. For the −5% compressed surface, both E_b and E_r favor the SSSV by 0.11 eV and 0.71 eV, respectively, and thus, the SSSV is by 0.82 eV more stable than the SSV. However, for the +5% strained surface, E_b favors the SSV by 0.14 eV and E_r the SSSV by 0.21 eV, and, as a result, the SSSV is only by 0.07 eV more stable than the SSV.

6.4.3 Vacancy clustering

As mentioned above, under zero applied stress, isolated subsurface vacancies are more stable than surface ones, and the interaction between nearest neighbor vacancies at the surface or in the subsurface is repulsive. We here consider strained reduced surfaces with either first-neighbor surface (SurDimer), or subsurface vacancy pairs (SubDimer), or pairs with a vacancy separation corresponding to that of third-nearest neighbors in the surface oxygen plane (SurDimer-d), or in the subsurface one (SubDimer-d), cf. Figure 45. Due to the large number of possibly different configurations of the four Ce^{3+} created upon formation of a vacancy dimer, we have selected a set that mostly involve combinations of

nearest-neighbor (A, B, C, D….) or next-nearest-neighbor (1, 2, 3, 4….) sites to the vacancies (Tables S3-S6). Figure 49 shows the averaged vacancy formation energy of the most stable structures as a function of strain (Table S7). As expected,[172, 180] under zero applied stress, the interaction between first-neighbor surface and subsurface vacancies is repulsive; creating two well-separated surface and subsurface vacancies is energetically more favorable by about 0.1 [ΔE= 2 E_f (Surdimer)– 2 E_f (SSV), cf. Eq. 1] and 0.2 eV [ΔE= 2 E_f (Subdimer)– 2 E_f (SSSV)], respectively, than the corresponding pair formation. Tensile strain helps neither the formation of surface nor subsurface vacancy pairs, but makes the preference for corresponding isolated species even more pronounced, for example, for +5% tensile strain, by about 0.6 and 0.4 eV, respectively; as discussed above, as the tensile strain increases beyond +3%, the SSV is the most stable vacancy species. However, upon lattice compression, the SurDimer and the SubDimer become more stable than the corresponding isolated species, for example, for –5% compressive strain, by about 0.4 and 0.2 eV, respectively, with the SubDimer being by about 0.9 eV more stable than the SurDimer.

We finally note that as for the case of the isolated species discussed above, for which compressive (tensile) strain favors NN (NNN) Ce^{3+} configurations, for the dimeric species, a similar tendency is observed, for example, the stable SurDimer and SubDimer configurations under –5% compressive strain have all four Ce^{3+} ions in the first cationic coordination shell of the vacancies (Table S3 and S4).

6.5 Conclusion

This work shows the important effect of lattice strain on the relative stability of different types of near-surface oxygen vacancies at the $CeO_2(111)$ surface, such as single surface and subsurface oxygen vacancy (SSV and SSSV) as well as corresponding first-neighbor vacancy dimers (SurDimer and SubDimer), and on their ground-state energy configurations with respect to the localization of the excess charge. SSV and SSSV have been considered with 5×5 and 2×2 periodicities whereas the vacancy dimers only with the larger unit cell. We have found three situations of energy crossover: (*i*) surface vs. sub-surface oxygen vacancy (SSV vs. SSSV); (*ii*) Ce^{3+} within the first vs. second coordination shell of the vacancies (NN vs. NNN); (*iii*) isolated vs. first-neighbor vacancy dimers (SSV/SSSV vs. SurDimer/SubDimer). Under 0% strain, isolated subsurface oxygen vacancies (SSSV) with both Ce^{3+} ions within the second coordination shell of the vacancies (NNN-NNN) are favored, and the interaction between first-neighbor vacancies is repulsive. However, if a large tensile stress is applied, the SSV with both Ce^{3+} in the second coordination shell of the vacancies become more stable than the SSSV, with both Ce^{3+} in NNN sites too. Moreover, if a large compressive strain is applied, the SSSV is more stable than the SSV as in the case of 0% strain, but for both vacancy types a configuration with both Ce^{3+} in the first coordination shell of the vacancies (NN-NN) are favored over that with both Ce^{3+} in the second coordination shell. Finally, under large compressive strain, the formation of first-neighbor surface (SurDimer) and subsurface vacancy dimers (SubDimer), with the four Ce^{3+} in NN sites, is more stable than having corresponding two isolated species, with the SubDimer being more stable than the SurDimer.

We have further analyzed the effects of lattice strain on the energy cost to create a single vacancy without allowing for lattice relaxations, E_b, and on the relaxation energy gain, E_r, and found that the preference for the surface or subsurface sites are the result of the different dependences of the E_b and E_r contributions on the applied stress. Regarding the Ce^{3+} switched preference in favor of the first coordination shell of the vacancies under compressive strain, we have inspected the calculated densities of states (DOS) and found that the Ce^{3+} switched preference is related to the exchange in the relative positions of highest occupied Ce^{3+} *f* states in the O_{2p}–Ce_{5d} gap region; under compressive strain, the occupied *f* states localized onto cationic sites in the first coordination shell of the vacancies lie lower in energy than those localized onto sites in the second coordination shell, whereas under tensile strain, the situation is reversed. The driving force for the Ce^{3+} switched preference is the better ability to relax the lattice strain in the preferred structure.

Generally speaking, the vacancy structures at ceria surfaces is of importance for technological applications. Clearly, the finding that the relative stabilities of vacancy structures do depend on the applied in-plane strain, particularly in relation to the formation of vacancy aggregates, cannot be ignored when considering that in most applications ceria is employed within a heterostructure or as a supported thin film in which ceria can be strained.

6.6 Supplementary information

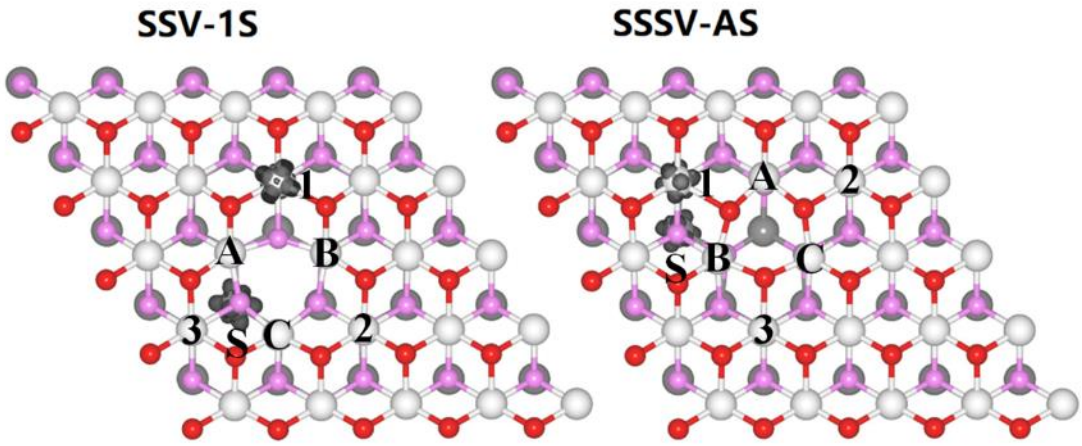

Figure S1. Isosurfaces of the spin density (high spin) for defective $CeO_2(111)$ surfaces with 5 × 5 periodicity. (a): single surface vacancy, SSV. (b): single subsurface vacancy, SSSV. Ce cations in the outermost tri-layer are shown as white balls. Surface and subsurface oxygen atoms are shown as red and pink balls, respectively. The labelled cerium atoms denote possible Ce^{3+} locations on nearest-neighbor (A, B, C, D….) or next-nearest-neighbor (1, 2, 3, 4….) sites to the vacancies in the outermost cationic layer; S denotes a Ce^{3+} in the layer beneath. Only the three outermost atomic layers are shown for simplicity.

Table S1. Oxygen vacancy formation energies (eV) of a SSV on the reduced $CeO_2(111)$ surface with 5 × 5 periodicity for different configurations of the Ce^{3+} ions. Nearest (NN) and next-nearest neighbor (NNN) Ce ions to vacancies in the outermost cationic layer are labelled with uppercase letters (A, B, C, D, …) and numerals (1, 2, 3, 4, …), respectively; S denotes a Ce^{3+} in the layer beneath.

Strain%	12	1C	1S	AB
+5	0.63	0.79	0.89	0.96
+4	0.91	1.05	1.18	1.26
+3	1.23	1.38	1.47	1.54

+2	1.49	1.57	1.76	1.80
+1	1.76	1.84	1.99	2.06
0	2.11	2.13	2.28	2.34
–1	2.38	2.42	2.56	2.56
–2	2.76	2.67	2.82	2.87
–3	3.00	2.93	3.12	3.07
–4	3.35	3.13	3.43	3.28
–5	3.57	3.47	*	3.45

*configuration changed during geometry optimization.

Table S2. Oxygen vacancy formation energies (eV) of a SSSV in the near-surface of reduced $CeO_2(111)$ with 5×5 periodicity for different configurations of the Ce^{3+} ions. The labelling is the same as in Table S1.

Strain%	12	1C	1S	AB
+5	0.80	0.91	1.22	*

+4	1.02	1.15	1.42	1.44
+3	1.26	1.42	1.64	1.68
+2	1.47	1.69	1.84	1.85
+1	1.65	1.85	2.03	2.04
0	1.88	2.07	2.18	2.20
–1	2.11	2.18	2.39	2.39
–2	2.30	2.34	2.60	2.48
–3	2.49	2.50	2.78	2.57
–4	2.76	2.78	3.06	2.75
–5	2.96	2.97	3.16	2.89

*configuration changed during geometry optimization.

Table S3. Averaged oxygen vacancy formation energies (eV) of a SurDimer on the reduced $CeO_2(111)$ with 5×5 periodicity surface for different configurations of the Ce^{3+} ions. The labelling is the same as in Table S1.

Strain %	Configuration										
	Energy/eV										
+5	24-BE	134-B	12-DE	14-BD	1-BDE	4-ACD	124-D	ABCE	1234	34-BE	24-BS
	0.93	0.93	0.94	0.95	0.99	1.02	1.05	1.07	1.13	1.15	*
+4	1234	134-B	124-E	24-BD	12-DE	14-CD	34-AB	234-S	1-BDE	4-ACD	ACDE
	1.16	1.18	1.19	1.21	1.22	1.23	1.25	1.27	1.32	1.32	1.36
+3	134-B	124-D	1234	34-BE	12-DE	24-BD	14-CD	134-S	4-ACD	1-BCE	ABCD
	1.45	1.46	1.47	1.48	1.49	1.50	1.51	1.54	1.58	1.62	1.65
+2	124-D	12-DE	134-B	1234	34-BE	24-BD	14-BD	124-S	4-BCD	1-BDE	ABCE
	1.69	1.70	1.71	1.71	1.72	1.73	1.74	1.76	1.79	1.81	1.85
+1	134-B	124-S	124-D	12-DE	24-BD	34-BE	14-BD	1234	4-BCD	1-BCE	ABCD
	1.94	1.94	1.96	1.96	1.97	1.97	1.99	1.99	2.01	2.06	2.13

0	24-BD	12-DE	14-BD	4-BCD	134-B	124-D	4-BCD	ABCE	1-BDE	1234	24-SS
	2.16	2.17	2.18	2.19	2.21	2.21	2.22	2.24	2.25	2.30	2.35
–1	134-B	4-BCD	12-DE	14-BD	134-S	24-BE	124-D	34-AB	1-BCE	ABCE	1234
	2.44	2.45	2.46	2.47	2.48	2.49	2.50	2.51	2.51	2.51	2.55
–2	24-BD	4-BCD	134-B	12-DE	14-BD	34-BE	124-D	ABCE	1-BDE	1234	24-SS
	2.66	2.67	2.68	2.68	2.69	2.69	2.70	2.71	2.73	2.77	2.83
–3	24-BD	4-BCE	34-BE	ABCE	12-DE	14-BD	124-D	134-B	1-BDE	1234	24-SS
	2.85	2.86	2.86	2.87	2.88	2.89	2.90	2.91	2.91	2.99	*
–4	ABCD	24-BD	34-BE	12-DE	1-BDE	4-BCE	124-D	134-B	14-BC	1234	ABSS
	3.08	3.09	3.11	3.13	3.13	3.15	3.16	3.16	3.17	3.30	3.32
–5	ABCE	34-BE	1-BDE	14-BD	134-B	12-DE	124-D	1234	ABSS	24-BD	4-BCE
	3.23	3.29	3.30	3.31	3.36	3.36	3.39	3.50	3.51	*	*

*configuration changed during geometry optimization.

Table S4. Averaged oxygen vacancy formation energies (eV) of a SubDimer in the near-surface of reduced $CeO_2(111)$ with 5×5 periodicity for different configurations of the Ce^{3+} ions. The labelling is the same as in Table S1.

Strain %	Configuration / Energy/eV										
+5	124-C	1234	34-CE	12-BD	234-A	124-S	ACDE	1-BCD	13-BD	14-AB	4-ABD
	1.02	1.04	1.08	1.09	1.09	1.11	1.54	*	*	*	*
+4	124-C	1234	234-S	34-CE	12-BD	BCDS	124-S	1-BCD	4-ABD	13-BD	14-AB
	1.20	1.24	1.27	1.27	1.31	1.45	1.33	1.46	1.48	*	*
+3	12-DS	12-CD	234-A	BDES	13-BD	1234	14-AB	1-BCD	124-S	4-ABS	34-AD
	1.49	1.51	1.51	1.52	1.52	1.53	1.54	1.54	1.55	1.58	1.65
+2	124-D	12-AD	234-A	1234	34-AB	13-BD	124-S	14-AB	1-BDS	4-BSS	BCDE
	1.62	1.65	1.68	1.69	1.70	1.71	1.73	1.73	1.79	1.80	1.93
+1	14-DS	14-BD	124-D	12-DS	234-A	13-BD	1234	34-AS	1-BDS	4-ABD	BDES

	1.83	1.85	1.86	1.88	1.89	1.92	1.92	1.92	1.99	2.05	2.07
	124-D	12-AD	13-BD	134-B	1234	34-AB	1-BDS	14-BD	4-ABC	BDES	124-S
0	1.99	2.01	2.01	2.02	2.04	2.06	2.08	2.08	2.09	2.10	2.11
	124-D	13-BD	234-A	34-AB	12-BD	1-BCD	1234	14-AB	124-S	3-ABD	BDSS
–1	2.18	2.20	2.28	2.29	2.30	2.30	2.32	2.33	2.33	2.35	2.46
	124-D	14-BD	13-BD	12-AD	1-BCD	34-AB	3-ABD	ABDS	1234	124-S	234-D
–2	2.37	2.39	2.39	2.42	2.43	2.47	2.48	2.53	2.53	2.53	2.55
	124-D	14-BD	BCDE	13-BD	1-BCD	12-CD	3-ABD	34-AD	234-D	124-S	1234
–3	2.54	2.56	2.57	2.57	2.57	2.59	2.64	2.66	2.69	2.71	2.73
	13-BD	1-ACD	12-AD	BCDE	124-D	14-BD	3-ABD	34-AB	13-BS	234-D	1234
–4	2.69	2.71	2.72	2.72	2.75	2.76	2.79	2.80	2.86	2.86	2.94
	ACDE	1-BCD	13-BD	ACDS	14-BD	3-ABD	12-DE	124-D	34-AB	234-D	1234

–5	2.77	2.81	2.83	2.84	2.84	2.86	2.86	2.87	2.96	3.00	3.07

*configuration changed during geometry optimization.

Table S5. Averaged oxygen vacancy formation energies (eV) of a SurDimer-d on the reduced $CeO_2(111)$ with 5×5 periodicity surface for different configurations of the Ce^{3+} ions. The labelling is the same as in Table S1.

Strain %	Configuration / Energy/eV									
+5	1234	234-B	134-E	124-F	123-F	24-AE	123-S	12-EF	23-BF	34-BC
	0.74	0.79	0.85	0.85	0.87	0.92	0.93	0.93	0.93	0.94
	4-ABD	13-CF	3-BCF	2-ACE	ABDE					
	0.95	0.96	0.97	1.07	1.12					
+4	1234	234-B	134-E	124-F	24-AE	123-F	13-CF	123-S	34-BC	23-BF
	1.03	1.08	1.13	1.15	1.16	1.17	1.18	1.19	1.20	1.22
	12-EF	4-ABD	3-BCF	2-ACE	ABDE					
	1.22	1.23	1.27	1.31	1.41					

	1234	234-B	34-BC	134-E	124-F	2-ACE	24-AE	13-CF	123-F	12-EF
	2.15	2.18	2.18	2.19	2.23	2.24	2.24	2.24	2.26	2.29
0										
	4-ABD	23-BF	3-BCF	123-S	ABDE					
	2.30	2.31	2.34	2.35	2.36					
	13-CF	3-BCF	234-B	4-ABD	23-BF	124-F	1234	2-ACE	ABDE	123-F
	3.26	3.27	3.28	3.29	3.31	3.32	3.35	3.35	3.36	3.36
–4										
	34-BC	12-EF	134-E	24-AE	13-FS					
	3.37	3.39	3.41	*	*					
	ABDE	1234	2-ACE	234-B	ABDS	124-F	12-EF	123-F	134-E	13-CF
	3.51	3.56	3.62	3.63	3.64	3.65	3.65	3.65	3.66	*
–5										
	23-BF	24-AE	34-BC	3-BCF	4-ABD					
	*	*	*	*	*					

*configuration changed during geometry optimization.

Table S6. Averaged oxygen vacancy formation energies (eV) of a SubDimer-d in the near-surface of reduced $CeO_2(111)$ with 5×5 periodicity for different configurations of the Ce^{3+} ions. The labelling is the same as in Table S1.

Strain %	Configuration									
	Energy/eV									
+5	1245	245-B	14-BE	125-D	145-B	25-AC	124-A	45-AB	125-S	12-DE
	0.83	0.90	0.91	0.91	0.94	0.95	0.99	1.00	1.04	1.11
	15-BD	1-BDE	2-CDF	5-ACE	ACDF					
	*	*	*	*	*					
+4	1245	125-C	245-S	124-S	25-AC	145-B	14-BE	45-BS	12-SS	125-S
	1.02	1.09	1.09	1.12	1.16	1.17	1.21	1.22	1.23	1.24
	15-SS	1-BDE	2-CDF	5-ACE	ACDF					
	1.26	1.36	*	*	*					
0	1245	245-B	14-BE	125-D	124-A	12-DE	2-CDF	125-S	145-B	25-AC

	1.85	1.86	1.88	1.88	1.89	1.91	1.93	1.94	1.94	1.96
	15-BD	5-ACE	1-DES	45-AS	ACDF					
	1.99	2.03	2.08	2.10	2.11					
	25-AC	125-D	245-B	45-AB	25-CS	1-BDE	15-BD	12-DE	145-B	ACDF
	2.69	2.71	2.72	2.72	2.73	2.74	2.76	2.76	2.76	2.78
–4										
	124-A	5-ACE	2-CDF	14-BE	1245					
	2.78	2.78	2.79	2.79	2.80					
	25-AC	14-BE	25-CS	125-D	12-DE	5-ACE	1245	ACDF	1-BDE	245-B
	2.84	2.85	2.88	2.89	2.89	2.89	2.90	2.91	2.91	2.92
–5										
	15-BD	45-AB	145-B	2-CDF	124-A					
	2.93	2.94	2.94	2.94	2.95					

*configuration changed during geometry optimization.

Table S7. Averaged oxygen vacancy formation energies (eV) of the most stable SSV, SSSV, SurDimer, SubDimer and SubDimer-d in the near-surface of reduced $CeO_2(111)$ with 5×5 periodicity.

Strain%	SSV	SSSV	SurDimer	Subdimer	SubDimer-d	SurDimer-d
+5	0.63	0.80	0.93	1.02	0.83	0.74
+4	0.91	1.02	1.16	1.20	1.02	1.03
+3	1.23	1.26	1.45	1.49		
+2	1.49	1.47	1.69	1.62		
+1	1.76	1.65	1.94	1.83		
0	2.11	1.88	2.16	1.99	1.86	2.15
–1	2.38	2.11	2.44	2.18		
–2	2.67	2.30	2.66	2.37		
–3	2.93	2.49	2.85	2.54		
–4	3.13	2.75	3.08	2.69	2.69	3.26
–5	3.45	2.89	3.23	2.77	2.84	3.51

Table S8. Oxygen vacancy formation energies (eV) of a SSV and a SSSV at the reduced $CeO_2(111)$ surface with 2 × 2 periodicity for different configurations of the Ce^{3+} ions. Nearest (NN) and next-nearest neighbor (NNN) Ce ions to vacancies in the outermost cationic layer are labelled with uppercase letters (A, B, C, D, …) and numerals (1, 2, 3, 4, …), respectively.

Strain%	SSV-AB	SSV-1B	SSV-14	SSSV-AB	SSSV-AD	SSSV-1A	SSSV-1D	SSSV-14
+5	1.29	1.07	1.06	1.52	1.06	1.02	0.96	0.99
+4	1.55		1.29	1.65				1.15
+3	1.80		1.53	1.87				1.32
+2	2.05		1.79	2.03				1.49
+1	2.29		2.04	2.18				1.67
0	2.52	2.35	2.30	2.38	2.41	2.00	2.11	1.84
–1	2.74		2.59	2.48				2.04
–2	2.96		2.87	2.59				2.22
–3	3.16		3.15	2.71				2.41

–4	3.42		3.43	2.78				2.57
–5	3.54	3.54	3.70	2.84	3.23	2.85	3.12	2.72

Table S9. Averaged oxygen vacancy formation energies (E_f), bond breaking energy (E_b), and relaxation energy gain ($-E_r$) of the most stable SSV, SSSV, and SurDimer in the near-surface of reduced $CeO_2(111)$ with 5×5 periodicity.

	E_f			E_b			$-E_r$		
Strain%	SSV	SSSV	SurDimer	SSV	SSSV	SurDimer	SSV	SSSV	SurDimer
+5	0.63	0.80	0.93	3.25	3.56	2.92	2.62	2.76	1.99
+4	0.91	1.02	1.16	3.42	3.73	3.04	2.51	2.71	1.88
+3	1.23	1.26	1.45	3.67	3.78	3.24	2.44	2.52	1.79
+2	1.49	1.47	1.69	3.85	3.89	3.31	2.36	2.42	1.62
+1	1.76	1.65	1.94	3.96	4.00	3.49	2.2	2.35	1.55
0	2.11	1.88	2.16	3.97	4.01	3.62	1.86	2.13	1.46

–1	2.38	2.11	2.44	4.08	4.11	3.72	1.70	2.00	1.28
–2	2.67	2.30	2.66	4.17	4.12	3.81	1.50	1.82	1.15
–3	2.93	2.49	2.85	4.38	4.25	3.91	1.45	1.76	1.06
–4	3.13	2.75	3.08	4.45	4.40	4.10	1.32	1.65	1.02
–5	3.45	2.89	3.23	4.49	4.35	4.19	1.04	1.46	0.96

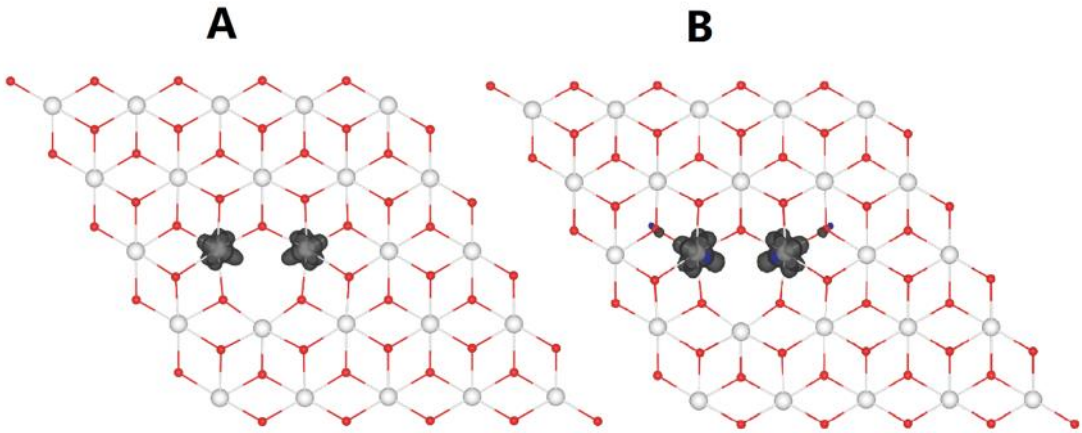

Figure S2. Isosurfaces of charge that fall into the (A) –0.5 eV to –0.28 eV energy range and (B) –0.28 eV to 0 eV for a SSV under –5% with AB Ce^{3+} configuration.

Table S10. O_{2p}-Ce_{5d}, the energy difference between the highest occupied 2*p*-states of O and the bottom of the empty 5*d*-states of Ce; O_{2p}-Ce_{4f}, the energy difference between the highest occupied 2*p*-states of O and the lowest occupied 4*f*-states of Ce; and *f*-splitting, the energy splitting between the two occupied 4*f* states of Ce for a SSV under –5%, 0% and +5% strain with different Ce^{3+} configurations, namely, AB, 12, and 1C

with 5×5 periodicity.

SSV	O_{2p}-Ce_{5d}	O_{2p}-Ce_{4f}	*f* splitting
AB: –5%	4.85	0.78	0.00*
AB: 0%	4.97	0.81	0.00
AB: +5%	4.71	0.41	0.00
1C: –5%	4.91	0.74	0.06
1C: 0%	5.11	0.75	0.04
1C: +5%	4.68	0.30	0.16
12: –5%	4.99	0.89	0.00
12: 0%	5.11	0.80	0.00
12: +5%	4.73	0.31	0.00

* polarons are no longer fully localized in one specific Ce site, rather, the polaronic charge is shared between the two sites in a sort of bonding/anti-bonding configuration (cf. isosurfaces in Fig. S2).

Table S11. Oxygen vacancy formation energies (E_f), bond breaking energy (E_b), and relaxation energy gain ($-E_r$) of the most stable SSV, SSSV in the near-surface of reduced $CeO_2(111)$ with 2×2 periodicity.

Strain%	E_f		E_b		$-E_r$	
	SSV	SSSV	SSV	SSSV	SSV	SSSV
+5	1.06	0.99	3.13	3.27	2.07	2.28
+4	1.29	1.15	3.26	3.41	1.97	2.26
+3	1.53	1.32	3.36	3.54	1.83	2.22
+2	1.79	1.49	3.50	3.68	1.71	2.19
+1	2.04	1.67	3.65	3.78	1.61	2.11
0	2.30	1.84	3.76	3.86	1.46	2.02
–1	2.59	2.04	3.88	3.98	1.29	1.94
–2	2.87	2.22	4.00	4.05	1.13	1.83
–3	3.15	2.41	4.11	4.14	0.96	1.73

–4	3.42	2.57	4.22	4.17	0.80	1.60
–5	3.54	2.72	4.32	4.21	0.78	1.49

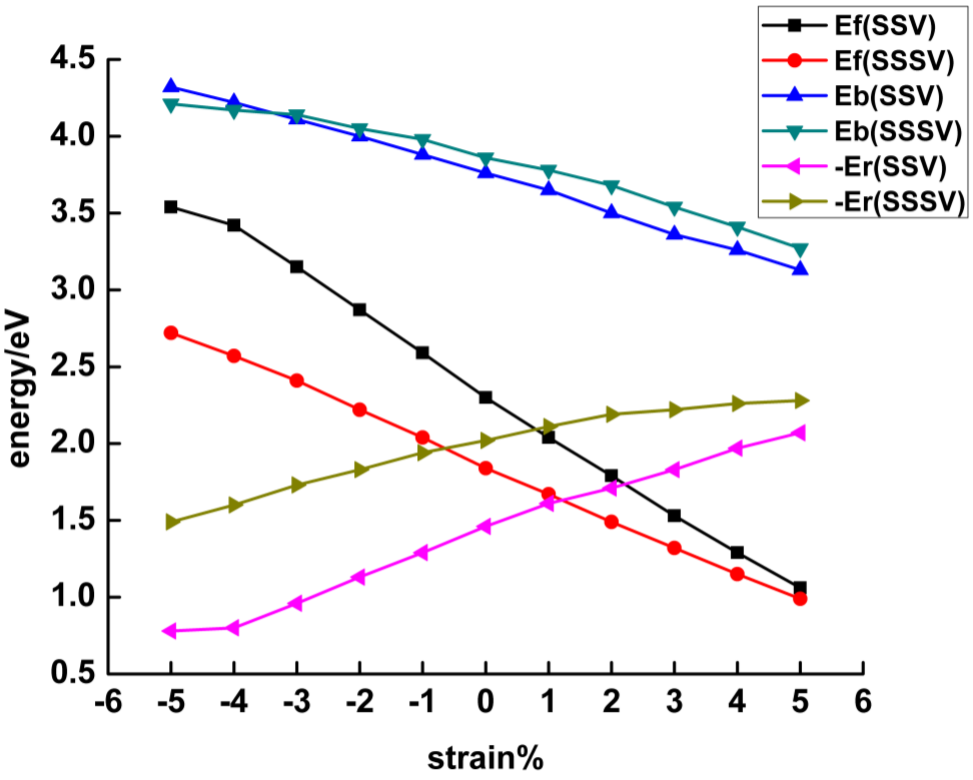

Figure S3. The near-surface oxygen vacancy formation energy, $E_f = E_b + E_r$, as a function of strain for the most stable SSV and SSSV with 2 × 2 periodicity. E_b is the energy cost to create a near-surface oxygen vacancy without allowing for lattice relaxations, i.e., the bond breaking energy, and E_r, the gain in relaxation energy.

6.7 Acknowledgements

This work has been funded by the National Natural Science Foundation of China (11574340, 21773287) as well as by the US Department of Energy SECA Core Technology

Program (DE-NT0006557) and DOE ARPA-E REBELS Program (DE-AR0000502). M.V.G.-P. acknowledges support by the MINECO-Spain (CTQ2015-71823-R). The computational resources utilized in this research have been provided by the National Supercomputing Center in Tianjin, the Shanghai Supercomputer Center and the Guangzhou Supercomputer Center, as well as by the National Energy Research Scientific Computing Center, a DOE Office of Science User Facility supported by the Office of Science of the U.S. Department of Energy under Contract No. DE-AC02-05CH11231. This work used the Extreme Science and Engineering Discovery Environment (XSEDE), which is supported by National Science Foundation grant number TG-DMR170045. We thank Gustavo E. Murgida from the CAC-CNEA and CONICET-Argentina for fruitful discussions.

CHAPTER 7 CONCLUSIONS AND RECOMMENDATIONS

7.1 Conclusions

The thermodynamic, kinetic, and electronic properties of three important solid-state ionic systems are investigated quantitatively using the combination of several atomic-level computational techniques. The main conclusions are summarized as follows.

Experimentally, dopant selection and doping-level optimization are daunting tasks. In CHAPTER 4, I demonstrated that these tasks can be performed efficiently through the use of computational methods to evaluate dopant solubility, proton conductivity, and material stability. The *ab-initio* thermodynamic workflow proved to be effective in predicting finite-temperature defect thermodynamic and kinetic properties. Out of 13 dopant candidates studied, A-site alkali elements, e.g., K, Rb, and Cs, as well as B-site Sc, Lu, and Gd, were recommended (but yet to be validated by experiments). The properties of the doped materials were quantitatively correlated with the intrinsic properties of the dopants, i.e., ionic radius and electronegativity. This computational workflow is transferable to the study of other solid-state ionic materials.

Whether or not dislocation serves as the diffusion pipeline in solid-state ionic materials is a controversial topic. CHAPTER 5 discusses the real edge dislocation line simulated in Y:$BaZrO_3$. The local structure of oxygen cages around the dislocation core was found to be distinct from the octahedron. This lowers the overall activation energy and enables facile oxygen ion transport. The optimal Y doping level was found to shift to a

higher value with regard to temperature. Dislocation, in this case, can facilitate ion transport, but not necessarily through the “pipe-diffusion” mechanism.

Various defect species on ceria (111) surface were reported, including single-surface and sub-surface vacancies, dimers, linear and triangular trimers, etc. In CHAPTER 6, I proposed that strain could easily modulate defect patterns in prepared ceria samples. Strain could be an important factor driving the emergence of variously observed vacancy patterns. The significance of strain on defect properties is an interesting topic for future study because it may critically affect the properties of nanostructured or thin film ceria, where remnant or misfit strain exists.

7.2 Recommendations for future work

For CHAPTER 4, statistical sampling of dopant-vacancy configurations is recommended. This will elucidate the role of microstructure-level defect patterns on proton transport. The dynamic correlation factor of proton motion is worthy of further study as well, which could shed light on proton-proton interactions within the lattice phonon.

For CHAPTER 5, a more robust hybrid Monte-Carlo/molecular dynamics simulation protocol needs to be developed, so that defect clustering can be simulated through this “global-minimization” protocol. For regions near dislocation, tension and compression could disturb the homogeneous/random defect distribution. It is significant if dopant-vacancy “co-segregation” or “co-depletion” near dislocation can be captured by this simulation protocol.

For CHAPTER 6, it would be interesting to build a realistic ceria nanoparticle model *in silico*. Since ceria catalysts usually appear in the form of nanoparticles/thin films, it is interesting to see how size and morphology affect their overall strain and defect distributions. Cluster expansion and the Monte-Carlo method might be needed to handle this challenge.

7.3 Major assumptions and approximations

Although the current computational result as well as the conclusion reached in this dissertation are reasonable and self-consistent, it is necessary here to summarize the major assumptions and approximations used within the computational approaches both for accountability reasons and for the benefit of further investigations.

In CHAPTER 4, I assumed the dilute and homogeneous dissolution process. The dilute defect assumption was used overall in the law of mass action and dilute defect diffusion theory. Defect-defect interactions, e.g., geometric defect configurations, vacancy-proton interactions, and proton-proton interactions, were neglected. When calculating the hydration property, only the most stable defect configuration before and after hydration was considered. Charged defect energy compensation was neglected when calculating reaction energies and subtracting energies of equally-charged defect species. The dynamic correlation factor of protons was assumed to be 1 (i.e., no correlation). The harmonic approximation was adopted for vibrational free energy calculation. Imaginary phonon modes observed in the defective cubic supercell might indicate a non-cubic symmetry; this was, however, omitted during vibrational free energy calculation.

In CHAPTER 5, dopants were randomly distributed in the supercell and considered immobile during the oxygen ion diffusion. An isolated dislocation line without any dislocation density information was assumed. The dislocation was treated as immobile and non-propagative under the simulation temperature and procedure.

In CHAPTER 6, it was assumed that with an applied strain of up to 5%, there was no significant surface reconstruction on ceria (111).

APPENDIX A. COMPUTATIONAL DETAILS

This appendix covers computation details: crystal structure, and thermodynamic reference state and charged-defect model.

A.1 Crystal structure

Crystal structure	$\boldsymbol{a, b, c}$ $(\boldsymbol{exp}.$Å$)$	$\boldsymbol{a, b, c}$ $(\boldsymbol{calc}.$Å$)$	$\boldsymbol{\alpha, \beta, \gamma}$ $(\boldsymbol{exp}.)$	$\boldsymbol{\alpha, \beta, \gamma}$ $(\boldsymbol{calc}.)$
$Ba(OH)_2$	a=6.861 b=7.981 c=11.070	a=6.849 b=7.975 c=11.177	$\alpha=\beta=90$ $\gamma=122$	$\alpha=\beta=90$ $\gamma=122$
$BaCO_3$	a=5.378 b=6.596 c=9.014	a=5.378 b=6.596 c=9.014	$\alpha=\beta=\gamma=90$	$\alpha=\beta=\gamma=90$
Molecule structure	$\boldsymbol{bond\ length}$ $(\boldsymbol{exp}.$Å$)$	$\boldsymbol{bond\ length}$ $(\boldsymbol{calc}.$Å$)$	$\boldsymbol{bond\ angle}$ $(\boldsymbol{exp}.)$	$\boldsymbol{bond\ angle}$ $(\boldsymbol{calc}.)$
O_2	1.208	1.233	N/A	N/A
CO_2	1.16	1.177	180	180

H_2O	0.96	0.972	104.5	104.47

Crystal structure	$\boldsymbol{a, b, c}$ $(\boldsymbol{exp}.$Å)	$\boldsymbol{a, b, c}$ $(\boldsymbol{calc}.$Å)	$\boldsymbol{\alpha, \beta, \gamma}$ $(\boldsymbol{exp}.)$	$\boldsymbol{\alpha, \beta, \gamma}$ $(\boldsymbol{calc}.)$
BaO	a=b=c=5.615	a=b=c=5.615	$\alpha=\beta=\gamma=90$	$\alpha=\beta=\gamma=90$
HfO_2	a=5.142 b=5.195 c=5.326	a=5.139 b=5.192 c=5.323	$\alpha=\gamma=90$ $\beta=99.67$	$\alpha=\gamma=90$ $\beta=99.68$
Li_2O	a=b=c=4.659	a=b=c=4.625	$\alpha=\beta=\gamma=90$	$\alpha=\beta=\gamma=90$
Na_2O	a=b=c=5.595	a=b=c=5.193	$\alpha=\beta=\gamma=90$	$\alpha=\beta=\gamma=90$
K_2O	a=b=c=6.488	a=b=c=6.486	$\alpha=\beta=\gamma=90$	$\alpha=\beta=\gamma=90$
Rb_2O	a=b=4.325 c=17.817	a=b=4.311 c=18.344	$\alpha=\beta=90$ $\gamma=120$	$\alpha=\beta=90$ $\gamma=120$
Cs_2O	a=b=4.262 c=22.051	a=b=4.274 c=22.035	$\alpha=\beta=90$ $\gamma=120$	$\alpha=\beta=90$ $\gamma=120$

Sc_2O_3	a=b=c=9.914	a=b=c=9.914	$\alpha=\beta=\gamma=90$	$\alpha=\beta=\gamma=90$
Y_2O_3	a=b=c=10.704	a=b=c=10.654	$\alpha=\beta=\gamma=90$	$\alpha=\beta=\gamma=90$
La_2O_3	a=b=c=11.402	a=b=c=11.402	$\alpha=\beta=\gamma=90$	$\alpha=\beta=\gamma=90$
Al_2O_3	a=b=4.805 c=13.116	a=b=4.808 c=13.119	$\alpha=\beta=90$ $\gamma=120$	$\alpha=\beta=90$ $\gamma=120$
Ga_2O_3	a=12.452 b=3.083 c=5.876	a=12.470 b=3.087 c=5.883	$\alpha=90$ $\beta=103.68$ $\gamma=90$	$\alpha=90$ $\beta=103.68$ $\gamma=90$
In_2O_3	a=b=c=10.301	a=b=c=10.297	$\alpha=\beta=\gamma=90$	$\alpha=\beta=\gamma=90$
Gd_2O_3	a=b=c=10.862	a=b=c=10.863	$\alpha=\beta=\gamma=90$	$\alpha=\beta=\gamma=90$
Lu_2O_3	a=b=c=10.365	a=b=c=10.470	$\alpha=\beta=\gamma=90$	$\alpha=\beta=\gamma=90$

A.2 Thermodynamic reference state

$$G(T) = G_{ele} + G_{vib}(T) = G_{ele,0K} + H_{vib}(T) - S_{vib}(T) * T,$$

$$G(T) - H_{298.15K} = \left(G_{ele,0K} - H_{ele,298.15K}\right) + \left(G_{vib}(T) - H_{vib,298.15K}\right)$$

$$= 0 + G_{vib}(T) - H_{vib,298.15K} = \left(H_{vib}(T) - H_{vib,298.15K}\right) - S_{vib}(T) * T,$$

$$\Delta G_{reac} = \Delta G_{ele,0K} + \Delta G_{vib}(T)|_{H_{vib,0K}=ZPE,\ S_{vib,0K}=0}$$

$$= \Delta H_{ele,0K} + \Delta\left(G_{vib}(T) - H_{vib,298.15K}\right)\Big|_{H_{vib,298.15K}=0, S_{vib,0K}=0}$$

$$= \Delta H_{ele,0K}$$

$$+ \Delta\left[\left(H_{vib}(T) - H_{vib,298.15K}\right) - S_{vib}(T) * T\right]\Big|_{H_{vib,298.15K}=0, S_{vib,0K}=0}$$

$$= \Delta H_{ele,0K}\Big|_{DFT} + \Delta(G_{vib}(T) - H_{vib,298.15K})\Big|_{DFT+exp.}$$

A.3 Thermodynamics of gas molecule

$$G(T) = H_{elec,0K} + G_{vib,rot,tran}(T)$$

$$= H_{elec,0K} + H_{vib}(T) + H_{rot}(T) + H_{tran}(T) - T * S_{vib,rot,tran}(T)$$

$$= H_{elec,0K} + H_{vib}(T) - T * S_{vib,rot,tran}(T) + E_{rot}(T) + E_{tran}(T) + k_B T$$

$E_{rot}(T) = 1.5k_BT\ for\ nonlinear\ molecule,\ and\ k_BT\ for\ linear\ molecule;$

$E_{tran}(T) = 1.5k_BT$

A.4 Correlation functions of BHCO SQS cells

Ce concentration = 8/9

2	4.200000	0.604938	0.604938	-0.000000
2	5.939697	0.604938	0.604938	-0.000000

2 7.274613 0.555556 0.604938 -0.049383

Objective_function= -1.682668

Ce concentration = 7/9

2 4.200000 0.308642 0.308642 -0.000000

2 5.939697 0.308642 0.308642 -0.000000

2 7.274613 0.222222 0.308642 -0.086420

Objective_function= -1.645631

Ce concentration = 6/9

2 4.200000 0.111111 0.111111 -0.000000

2 5.939697 0.111111 0.111111 -0.000000

2 7.274613 0.000000 0.111111 -0.111111

Objective_function= -1.620940

Ce concentration = 5/9

2 4.200000 0.012346 0.012346 -0.000000

2 5.939697 0.012346 0.012346 -0.000000

2 7.274613 -0.111111 0.012346 -0.123457

Objective_function= -1.608594

Ce concentration = 4/9

2	4.200000	0.012346	0.012346	-0.000000
2	5.939697	0.012346	0.012346	-0.000000
2	7.274613	-0.111111	0.012346	-0.123457

Objective_function= -1.608594

Ce concentration = 3/9

2	4.200000	0.111111	0.111111	-0.000000
2	5.939697	0.111111	0.111111	-0.000000
2	7.274613	0.000000	0.111111	-0.111111

Objective_function= -1.620940

Ce concentration = 2/9

2	4.200000	0.308642	0.308642	-0.000000
2	5.939697	0.308642	0.308642	-0.000000
2	7.274613	0.222222	0.308642	-0.086420

Objective_function= -1.645631

Ce concentration = 1/9

2	4.200000	0.604938	0.604938	-0.000000
2	5.939697	0.604938	0.604938	-0.000000
2	7.274613	0.555556	0.604938	-0.049383

Objective_function= -1.682668

A.5 Correlation functions of doped-BHCO SQS cells (Gd as an example)

::::::::::::::

Gd/H/bestcorr.out

::::::::::::::

2	1.484924	0.938272	0.927298	0.010974
2	1.484924	0.925926	0.927298	-0.001372
2	2.100000	0.925926	0.927298	-0.001372
2	2.100000	0.925926	0.927298	-0.001372
2	2.347871	0.152778	0.160494	-0.007716
2	2.347871	-0.269965	-0.277984	0.008019
2	2.571964	0.929012	0.927298	0.001715

2	2.969848	0.932099	0.927298	0.004801
2	3.320392	0.925926	0.927298	-0.001372
2	3.320392	0.925926	0.927298	-0.001372
2	3.637307	0.932099	0.927298	0.004801
2	3.637307	0.925926	0.927298	-0.001372
2	3.785829	0.157407	0.160494	-0.003086
2	3.785829	-0.283329	-0.277984	-0.005346
2	3.928740	0.925926	0.927298	-0.001372
2	3.928740	0.925926	0.927298	-0.001372
2	4.200000	0.925926	0.927298	-0.001372
2	4.200000	0.925926	0.927298	-0.001372
2	4.200000	0.925926	0.927298	-0.001372
2	4.200000	0.000000	0.027778	-0.027778
2	4.200000	-0.032075	-0.048113	0.016038
2	4.200000	0.037037	0.083333	-0.046296
2	4.454773	0.925926	0.927298	-0.001372

2	4.454773	0.925926	0.927298	-0.001372
2	4.454773	0.925926	0.927298	-0.001372
2	4.454773	0.925926	0.927298	-0.001372
2	4.695743	0.925926	0.927298	-0.001372
2	4.695743	0.925926	0.927298	-0.001372
2	4.695743	0.925926	0.927298	-0.001372
2	4.695743	0.925926	0.927298	-0.001372
2	4.811704	0.159722	0.160494	-0.000772
2	4.811704	-0.281993	-0.277984	-0.004009
2	4.924937	0.925926	0.927298	-0.001372
2	5.143928	0.925926	0.927298	-0.001372
2	5.353970	0.929012	0.927298	0.001715
2	5.353970	0.925926	0.927298	-0.001372
2	5.353970	0.925926	0.927298	-0.001372
2	5.353970	0.925926	0.927298	-0.001372
2	5.654423	0.168981	0.160494	0.008488

2	5.654423	-0.281993	-0.277984	-0.004009
2	5.654423	0.171296	0.160494	0.010802
2	5.654423	-0.280656	-0.277984	-0.002673
2	5.751087	0.925926	0.927298	-0.001372
2	5.751087	0.925926	0.927298	-0.001372
2	5.939697	0.925926	0.927298	-0.001372
2	5.939697	0.925926	0.927298	-0.001372
2	5.939697	0.932099	0.927298	0.004801
2	5.939697	0.027778	0.027778	-0.000000
2	5.939697	-0.040094	-0.048113	0.008019
2	5.939697	0.074074	0.083333	-0.009259
2	6.122499	0.925926	0.927298	-0.001372
2	6.122499	0.925926	0.927298	-0.001372
2	6.122499	0.932099	0.927298	0.004801
2	6.122499	0.925926	0.927298	-0.001372
2	6.300000	0.925926	0.927298	-0.001372

2	6.300000	0.932099	0.927298	0.004801
2	6.300000	0.925926	0.927298	-0.001372
2	6.300000	0.925926	0.927298	-0.001372
2	6.386901	0.166667	0.160494	0.006173
2	6.386901	-0.277983	-0.277984	0.000000
2	6.472635	0.925926	0.927298	-0.001372
2	6.472635	0.925926	0.927298	-0.001372
2	6.472635	0.932099	0.927298	0.004801
2	6.640783	0.925926	0.927298	-0.001372
2	6.804778	0.925926	0.927298	-0.001372
2	6.804778	0.929012	0.927298	0.001715
2	6.964912	0.925926	0.927298	-0.001372
2	6.964912	0.925926	0.927298	-0.001372
2	6.964912	0.925926	0.927298	-0.001372
2	6.964912	0.925926	0.927298	-0.001372
2	7.043614	0.159722	0.160494	-0.000772

2	7.043614	-0.273974	-0.277984	0.004009
2	7.043614	0.175926	0.160494	0.015432
2	7.043614	-0.283329	-0.277984	-0.005346
2	7.121446	0.925926	0.927298	-0.001372
2	7.121446	0.925926	0.927298	-0.001372
2	7.274613	0.925926	0.927298	-0.001372
2	7.274613	-0.000000	0.027778	-0.027778
2	7.274613	-0.060141	-0.048113	-0.012028
2	7.274613	0.069444	0.083333	-0.013889
2	7.424621	0.932099	0.927298	0.004801
2	7.424621	0.929012	0.927298	0.001715
2	7.424621	0.925926	0.927298	-0.001372
2	7.424621	0.925926	0.927298	-0.001372
2	7.424621	0.925926	0.927298	-0.001372
2	7.424621	0.925926	0.927298	-0.001372
2	7.571658	0.925926	0.927298	-0.001372

2	7.571658	0.925926	0.927298	-0.001372
2	7.571658	0.925926	0.927298	-0.001372
2	7.571658	0.925926	0.927298	-0.001372
2	7.644115	0.148148	0.160494	-0.012346
2	7.644115	-0.283329	-0.277984	-0.005346
2	7.644115	0.171296	0.160494	0.010802
2	7.644115	-0.280656	-0.277984	-0.002673
2	7.715893	0.925926	0.927298	-0.001372
2	7.715893	0.925926	0.927298	-0.001372
2	7.715893	0.925926	0.927298	-0.001372
2	7.715893	0.925926	0.927298	-0.001372
2	7.857481	0.925926	0.927298	-0.001372
2	7.857481	0.925926	0.927298	-0.001372
2	7.996562	0.925926	0.927298	-0.001372
2	7.996562	0.932099	0.927298	0.004801

Objective_function= -0.995907

::::::::::::::

Gd/Va/bestcorr.out

::::::::::::::

2	2.100000	-0.148148	-0.154321	0.006173
2	2.100000	0.277983	0.267292	0.010692
2	2.969848	0.851852	0.857339	-0.005487
2	4.200000	0.851852	0.857339	-0.005487
2	4.200000	0.851852	0.857339	-0.005487
2	4.200000	0.027778	0.027778	-0.000000
2	4.200000	-0.048113	-0.048113	0.000000
2	4.200000	0.046296	0.083333	-0.037037
2	4.695743	-0.152778	-0.154321	0.001543
2	4.695743	0.269965	0.267292	0.002673
2	5.143928	0.858025	0.857339	0.000686
2	5.939697	0.851852	0.857339	-0.005487
2	5.939697	0.851852	0.857339	-0.005487

2	5.939697	-0.000000	0.027778	-0.027778
2	5.939697	-0.032075	-0.048113	0.016038
2	5.939697	0.074074	0.083333	-0.009259
2	6.300000	-0.166667	-0.154321	-0.012346
2	6.300000	0.245908	0.267292	-0.021383
2	6.300000	-0.166667	-0.154321	-0.012346
2	6.300000	0.267292	0.267292	-0.000000
2	6.640783	0.851852	0.857339	-0.005487
2	7.274613	0.864198	0.857339	0.006859
2	7.274613	0.020833	0.027778	-0.006944
2	7.274613	-0.060141	-0.048113	-0.012028
2	7.274613	0.062500	0.083333	-0.020833
2	7.571658	-0.148148	-0.154321	0.006173
2	7.571658	0.277983	0.267292	0.010692
2	7.857481	0.858025	0.857339	0.000686

Objective_function= -0.990890

REFERENCES

1. Wachsman, E., T. Ishihara, and J. Kilner, *Low-temperature solid-oxide fuel cells.* Mrs Bulletin, 2014. **39**(9): p. 773-782.

2. Duan, C.C., et al., *Readily processed protonic ceramic fuel cells with high performance at low temperatures.* Science, 2015. **349**(6254): p. 1321-1326.

3. Duan, C.C., et al., *Highly durable, coking and sulfur tolerant, fuel-flexible protonic ceramic fuel cells.* Nature, 2018. **557**(7704): p. 217-+.

4. Yang, L., et al., *Enhanced Sulfur and Coking Tolerance of a Mixed Ion Conductor for SOFCs: BaZr0.1Ce0.7Y0.2-xYbxO3-delta.* Science, 2009. **326**(5949): p. 126-129.

5. Choi, S., et al., *Exceptional power density and stability at intermediate temperatures in protonic ceramic fuel cells.* Nature Energy, 2018. **3**(3): p. 202-210.

6. Ding, J., et al., *Influence of Nonstoichiometry on Proton Conductivity in Thin-Film Yttrium-Doped Barium Zirconate.* ACS Appl Mater Interfaces, 2018. **10**(5): p. 4816-4823.

7. Borges, K.C.M., et al., *A Comparative Study of Conventional and Microwave Sintering of $BaCe1-xGdxO3-\delta$ Ceramic.* Journal of Inorganic and Organometallic Polymers and Materials, 2017. **28**(1): p. 130-136.

8. Yamazaki, Y., R. Hernandez-Sanchez, and S.M. Haile, *Cation non-stoichiometry in yttrium-doped barium zirconate: phase behavior, microstructure, and proton conductivity.* Journal of Materials Chemistry, 2010. **20**(37).

9. Yamazaki, Y., R. Hernandez-Sanchez, and S.M. Haile, *High Total Proton Conductivity in Large-Grained Yttrium-Doped Barium Zirconate.* Chemistry of Materials, 2009. **21**(13): p. 2755-2762.

10. Balachandran, J., et al., *Defect Genome of Cubic Perovskites for Fuel Cell Applications.* The Journal of Physical Chemistry C, 2017. **121**(48): p. 26637-26647.

11. Bilić, A. and J.D. Gale, *Ground state structure of BaZrO3: A comparative first-principles study.* Physical Review B, 2009. **79**(17).

12. Bjorheim, T.S., et al., *Thermodynamic properties of neutral and charged oxygen vacancies in BaZrO3 based on first principles phonon calculations.* Phys Chem Chem Phys, 2015. **17**(32): p. 20765-74.

13. Bjørheim, T.S., et al., *Surface Segregation Entropy of Protons and Oxygen Vacancies in BaZrO3.* Chemistry of Materials, 2016. **28**(5): p. 1363-1368.

14. Bjørheim, T.S., E.A. Kotomin, and J. Maier, *Hydration entropy of BaZrO3 from first principles phonon calculations.* Journal of Materials Chemistry A, 2015. **3**(14): p. 7639-7648.

15. Björketun, M.E., P.G. Sundell, and G. Wahnström, *Effect of acceptor dopants on the proton mobility in BaZrO3: A density functional investigation.* Physical Review B, 2007. **76**(5).

16. Björketun, M.E., P.G. Sundell, and G. Wahnström, *Structure and thermodynamic stability of hydrogen interstitials in BaZrO3 perovskite oxide from density functional calculations.* Faraday Discuss., 2007. **134**: p. 247-265.

17. Blanc, F., et al., *Dynamic Nuclear Polarization NMR of Low-gamma Nuclei: Structural Insights into Hydrated Yttrium-Doped BaZrO3.* J Phys Chem Lett, 2014. **5**(14): p. 2431-6.

18. Dawson, J.A., J.A. Miller, and I. Tanaka, *First-Principles Insight into the Hydration Ability and Proton Conduction of the Solid State Proton Conductor, Y and Sn Co-Doped BaZrO3.* Chemistry of Materials, 2015. **27**(3): p. 901-908.

19. Dawson, J.A. and I. Tanaka, *Proton trapping in Y and Sn Co-doped BaZrO3.* Journal of Materials Chemistry A, 2015. **3**(18): p. 10045-10051.

20. Fluri, A., et al., *Enhanced Proton Conductivity in Y-Doped BaZrO3 via Strain Engineering.* Adv Sci (Weinh), 2017. **4**(12): p. 1700467.

21. Fronzi, M., et al., *First-principles molecular dynamics simulations of proton diffusion in cubic BaZrO3 perovskite under strain conditions.* Materials for Renewable and Sustainable Energy, 2016. **5**(4).

22. Giannici, F., et al., *Long-Range and Short-Range Structure of Proton-Conducting Y:BaZrO3.* Chemistry of Materials, 2011. **23**(11): p. 2994-3002.

23. Gomez, M.A., et al., *The effect of yttrium dopant on the proton conduction pathways of BaZrO3, a cubic perovskite.* J Chem Phys, 2010. **132**(21): p. 214709.

24. Gonçalves, M.D., et al., *Enthalpy of formation and thermodynamic insights into yttrium doped BaZrO3.* J. Mater. Chem. A, 2014. **2**(42): p. 17840-17847.

25. Han, D., et al., *Substantial appearance of origin of conductivity decrease in Y-doped BaZrO3due to Ba-deficiency.* RSC Advances, 2014. **4**(60).

26. Han, D., et al., *A comprehensive understanding of structure and site occupancy of Y in Y-doped BaZrO3.* Journal of Materials Chemistry A, 2013. **1**(9).

27. Han, D., et al., *Origins of structural and electrochemical influence on Y-doped BaZrO3heat-treated with NiO additive.* Journal of Materials Chemistry A, 2014. **2**(31).

28. Kitamura, N., et al., *Proton Distribution and Dynamics in Y- and Zn-Doped BaZrO3.* The Journal of Physical Chemistry C, 2014. **118**(33): p. 18846-18852.

29. Krueger, R.A., et al., *Centrality measures highlight proton traps and access points to proton highways in kinetic Monte Carlo trajectories*. J Chem Phys, 2015. **142**(15): p. 154110.

30. Lindman, A., P. Erhart, and G. Wahnström, *Polaronic contributions to oxidation and hole conductivity in acceptor-doped BaZrO3.* Physical Review B, 2016. **94**(7).

31. Løken, A., et al., *Alkali metals as efficient A-site acceptor dopants in proton conducting BaZrO3.* Journal of Materials Chemistry A, 2016. **4**(23): p. 9229-9235.

32. Mazzei, L., et al., *Structure and Conductivity of Epitaxial Thin Films of In-Doped BaZrO3-Based Proton Conductors.* The Journal of Physical Chemistry C, 2016. **120**(50): p. 28415-28422.

33. Merinov, B. and W. Goddard, 3rd, *Proton diffusion pathways and rates in Y-doped BaZrO3 solid oxide electrolyte from quantum mechanics.* J Chem Phys, 2009. **130**(19): p. 194707.

34. Muhammad Alay, E.A.S., S. Nazir, and A. Shaukat, *Formation energies and electronic structure of intrinsic vacancy defects and oxygen vacancy clustering in BaZrO3.* Phys Chem Chem Phys, 2016. **18**(34): p. 23737-45.

35. Oikawa, I. and H. Takamura, *Correlation among Oxygen Vacancies, Protonic Defects, and the Acceptor Dopant in Sc-Doped BaZrO3 Studied by 45Sc Nuclear Magnetic Resonance.* Chemistry of Materials, 2015. **27**(19): p. 6660-6667.

36. Ottochian, A., et al., *Influence of isotropic and biaxial strain on proton conduction in Y-doped BaZrO3: a reactive molecular dynamics study.* Journal of Materials Chemistry A, 2014. **2**(9).

37. Polfus, J.M., et al., *Surface defect chemistry of Y-substituted and hydrated BaZrO3 with subsurface space-charge regions.* Journal of Materials Chemistry A, 2016. **4**(19): p. 7437-7444.

38. Raiteri, P., J.D. Gale, and G. Bussi, *Reactive force field simulation of proton diffusion in BaZrO3 using an empirical valence bond approach.* J Phys Condens Matter, 2011. **23**(33): p. 334213.

39. Shirpour, M., et al., *Dopant Segregation and Space Charge Effects in Proton-Conducting BaZrO3 Perovskites.* The Journal of Physical Chemistry C, 2012. **116**(3): p. 2453-2461.

40. Sundell, P.G., M.E. Björketun, and G. Wahnström, *Density-functional calculations of prefactors and activation energies for H diffusion in BaZrO3.* Physical Review B, 2007. **76**(9).

41. Sundell, P.G., M.E. Björketun, and G. Wahnström, *Thermodynamics of doping and vacancy formation in BaZrO3 perovskite oxide from density functional calculations.* Physical Review B, 2006. **73**(10).

42. Takahashi, H., et al., *First-Principles Calculations for the Energetics of the Hydration Reaction of Acceptor-Doped BaZrO3.* Chemistry of Materials, 2017. **29**(4): p. 1518-1526.

43. Bévillon, É., et al., *Theoretical and experimental study of the structural, dynamical and dielectric properties of perovskite BaSnO3.* Journal of Physics: Condensed Matter, 2008. **20**(14).

44. Geneste, G., et al., *DFT+U study of self-trapping, trapping, and mobility of oxygen-type hole polarons in barium stannate.* Physical Review B, 2017. **96**(13).

45. Geneste, G. and G. Dezanneau, *Competition between elastic and chemical effects in the doping, defect association, and hydration of barium stannate.* Solid State Ionics, 2017. **308**: p. 121-132.

46. Geneste, G., J. Hermet, and G. Dezanneau, *Reply to the 'Comment on "Proton transport in barium stannate: classical, semi-classical and quantum regime"'.* Phys Chem Chem Phys, 2017. **19**(31): p. 21191-21209.

47. Geneste, G., et al., *Proton transport in barium stannate: classical, semi-classical and quantum regimes.* Phys Chem Chem Phys, 2015. **17**(29): p. 19104-18.

48. Samgin, A.L. and A.N. Ezin, *Comment on "Proton transport in barium stannate: classical, semi-classical and quantum regimes" by G. Geneste, A. Ottochian, J. Hermet and G. Dezanneau, Phys. Chem. Chem. Phys., 2015, 17, 19104.* Phys Chem Chem Phys, 2017. **19**(31): p. 21185-21190.

49. Wang, Y., et al., *Properties of Y-doped BaSnO3 proton conductors.* Solid State Ionics, 2012. **214**: p. 45-55.

50. Cordero, F., et al., *Effect of doping and oxygen vacancies on the octahedral tilt transitions in the BaCeO3 perovskite.* Physical Review B, 2010. **82**(10).

51. Hermet, J., et al., *Kinetic Monte Carlo study of protonic diffusion and conduction in Gd-doped BaCeO3.* Solid State Ionics, 2013. **252**: p. 48-55.

52. Loken, A., R. Haugsrud, and T.S. Bjorheim, *Unravelling the fundamentals of thermal and chemical expansion of BaCeO3 from first principles phonon calculations.* Phys Chem Chem Phys, 2016. **18**(45): p. 31296-31303.

53. Helgee, E., *Atomistic simulation of interfaces Proton transport across BaZrO3 grain boundaries.* 2013.

54. Marrocchelli, D., L. Sun, and B. Yildiz, *Dislocations in SrTiO3: easy to reduce but not so fast for oxygen transport.* J Am Chem Soc, 2015. **137**(14): p. 4735-48.

55. Sun, L., D. Marrocchelli, and B. Yildiz, *Edge dislocation slows down oxide ion diffusion in doped CeO2 by segregation of charged defects.* Nature Communications, 2015. **6**(1).

56. Li, X., et al., *Fast Oxygen Transport in Bottlelike Channels for Y-Doped BaZrO3: A Reactive Molecular Dynamics Investigation.* The Journal of Physical Chemistry C, 2019. **123**(42): p. 25611-25617.

57. van Duin, A.C.T., et al., *ReaxFF Reactive Force Field for the Y-Doped BaZrO3 Proton Conductor with Applications to Diffusion Rates for Multigranular Systems.* Journal of Physical Chemistry A, 2008. **112**(45): p. 11414-11422.

58. Arapan, S., S.I. Simak, and N.V. Skorodumova, *Volume-dependent electron localization in ceria.* Physical Review B, 2015. **91**(12).

59. Han, Z.K., et al., *The Structure of Oxygen Vacancies in the Near-Surface of Reduced CeO2 (111) Under Strain.* Front Chem, 2019. **7**: p. 436.

60. Ganduglia-Pirovano, M.V., J.L. Da Silva, and J. Sauer, *Density-functional calculations of the structure of near-surface oxygen vacancies and electron localization on CeO 2 (111).* Physical review letters, 2009. **102**(2): p. 026101.

61. Jerratsch, J.F., et al., *Electron localization in defective ceria films: a study with scanning-tunneling microscopy and density-functional theory.* Phys Rev Lett, 2011. **106**(24): p. 246801.

62. Gomez, M.A., et al., *Comparison of proton conduction in KTaO3 and SrZrO3.* J Chem Phys, 2007. **126**(19): p. 194701.

63. Kang, S.G. and D.S. Sholl, *First principles studies of proton conduction in KTaO3.* J Chem Phys, 2014. **141**(2): p. 024707.

64. Spahr, E.J., et al., *Proton tunneling: a decay channel of the O-H stretch mode in KTaO3.* Phys Rev Lett, 2009. **102**(7): p. 075506.

65. Shannon, R.D., *Revised Effective Ionic-Radii and Systematic Studies of Interatomic Distances in Halides and Chalcogenides.* Acta Crystallographica Section A, 1976. **32**(Sep1): p. 751-767.

66. Allred, A.L., *Electronegativity Values from Thermochemical Data.* Journal of Inorganic & Nuclear Chemistry, 1961. **17**(3-4): p. 215-221.

67. Lindman, A., P. Erhart, and G. Wahnström, *Implications of the band gap problem on oxidation and hydration in acceptor-doped barium zirconate.* Physical Review B, 2015. **91**(24).

68. Leslie, M. and M.J. Gillan, *The Energy and Elastic Dipole Tensor of Defects in Ionic-Crystals Calculated by the Supercell Method*. Journal of Physics C-Solid State Physics, 1985. **18**(5): p. 973-982.

69. Makov, G. and M.C. Payne, *Periodic Boundary-Conditions in Ab-Initio Calculations.* Physical Review B, 1995. **51**(7): p. 4014-4022.

70. Freysoldt, C., J. Neugebauer, and C.G. Van de Walle, *Electrostatic interactions between charged defects in supercells.* physica status solidi (b), 2011. **248**(5): p. 1067-1076.

71. Youssef, M. and B. Yildiz, *Predicting self-diffusion in metal oxides from first principles: The case of oxygen in tetragonal ZrO2.* Physical Review B, 2014. **89**(2).

72. Vanhove, L., *Correlations in Space and Time and Born Approximation Scattering in Systems of Interacting Particles.* Physical Review, 1954. **95**(1): p. 249-262.

73. Compaan, K. and Y. Haven, *Correlation Factors for Diffusion in Solids.* Transactions of the Faraday Society, 1956. **52**(6): p. 786-801.

74. Shirpour, M., et al., *Nonlinear electrical grain boundary properties in proton conducting Y-BaZrO3 supporting the space charge depletion model.* Physical Chemistry Chemical Physics, 2012. **14**(2): p. 730-740.

75. Shirpour, M., R. Merkle, and J. Maier, *Space charge depletion in grain boundaries of BaZrO3 proton conductors.* Solid State Ionics, 2012. **225**: p. 304-307.

76. Lindman, A., E.E. Helgee, and G. Wahnström, *Comparison of Space-Charge Formation at Grain Boundaries in Proton-Conducting BaZrO3 and BaCeO3.* Chemistry of Materials, 2017. **29**(18): p. 7931-7941.

77. Skorodumova, N.V., et al., *Quantum origin of the oxygen storage capability of ceria.* Phys Rev Lett, 2002. **89**(16): p. 166601.

78. Nakayama, M., et al., *A concerted migration mechanism of mixed oxide ion and electron conduction in reduced ceria studied by first-principles density functional theory.* Phys Chem Chem Phys, 2012. **14**(17): p. 6079-84.

79. Murgida, G.E. and M.V. Ganduglia-Pirovano, *Evidence for subsurface ordering of oxygen vacancies on the reduced CeO2(111) surface using density-functional and statistical calculations.* Phys Rev Lett, 2013. **110**(24): p. 246101.

80. Dudarev, S.L., et al., *Electron-energy-loss spectra and the structural stability of nickel oxide: An LSDA+U study.* Physical Review B, 1998. **57**(3): p. 1505-1509.

81. Hohenberg, P. and W. Kohn, *Inhomogeneous Electron Gas.* Physical Review B, 1964. **136**(3b): p. B864-+.

82. Kohn, W. and L.J. Sham, *Self-Consistent Equations Including Exchange and Correlation Effects.* Physical Review, 1965. **140**(4a): p. 1133-&.

83. Perdew, J.P., *Accurate Density Functional for the Energy - Real-Space Cutoff of the Gradient Expansion for the Exchange Hole.* Physical Review Letters, 1985. **55**(16): p. 1665-1668.

84. Perdew, J.P., et al., *Atoms, Molecules, Solids, and Surfaces - Applications of the Generalized Gradient Approximation for Exchange and Correlation.* Physical Review B, 1992. **46**(11): p. 6671-6687.

85. Perdew, J.P., K. Burke, and M. Ernzerhof, *Generalized gradient approximation made simple.* Physical Review Letters, 1996. **77**(18): p. 3865-3868.

86. Hammer, B., L.B. Hansen, and J.K. Norskov, *Improved adsorption energetics within density-functional theory using revised Perdew-Burke-Ernzerhof functionals.* Physical Review B, 1999. **59**(11): p. 7413-7421.

87. Csonka, G.I., et al., *Assessing the performance of recent density functionals for bulk solids.* Physical Review B, 2009. **79**(15).

88. Armiento, R. and A.E. Mattsson, *Functional designed to include surface effects in self-consistent density functional theory.* Physical Review B, 2005. **72**(8).

89. Perdew, J.P., M. Emzerhof, and K. Burke, *Rationale for mixing exact exchange with density functional approximations.* Journal of Chemical Physics, 1996. **105**(22): p. 9982-9985.

90. Kresse, G., *Ab-Initio Molecular-Dynamics for Liquid-Metals.* Journal of Non-Crystalline Solids, 1995. **193**: p. 222-229.

91. Kresse, G. and J. Hafner, *Ab-Initio Molecular-Dynamics Simulation of the Liquid-Metal Amorphous-Semiconductor Transition in Germanium.* Physical Review B, 1994. **49**(20): p. 14251-14269.

92. Pick, R.M., M.H. Cohen, and R.M. Martin, *Microscopic Theory of Force Constants in Adiabatic Approximation.* Physical Review B-Solid State, 1970. **1**(2): p. 910-+.

93. Baroni, S., et al., *Phonons and related crystal properties from density-functional perturbation theory.* Reviews of Modern Physics, 2001. **73**(2): p. 515-562.

94. Togo, A. and I. Tanaka, *First principles phonon calculations in materials science.* Scripta Materialia, 2015. **108**: p. 1-5.

95. Henkelman, G. and H. Jonsson, *Improved tangent estimate in the nudged elastic band method for finding minimum energy paths and saddle points.* Journal of Chemical Physics, 2000. **113**(22): p. 9978-9985.

96. van de Walle, A., *Multicomponent multisublattice alloys, nonconfigurational entropy and other additions to the Alloy Theoretic Automated Toolkit.* Calphad-Computer Coupling of Phase Diagrams and Thermochemistry, 2009. **33**(2): p. 266-278.

97. van de Walle, A., M. Asta, and G. Ceder, *The Alloy Theoretic Automated Toolkit: A user guide.* Calphad-Computer Coupling of Phase Diagrams and Thermochemistry, 2002. **26**(4): p. 539-553.

98. Zunger, A., et al., *Special quasirandom structures.* Phys Rev Lett, 1990. **65**(3): p. 353-356.

99. Wang, Y., et al., *Phonon dispersions in random alloys: a method based on special quasi-random structure force constants.* J Phys Condens Matter, 2011. **23**(48): p. 485403.

100. Huang, S., F. Tian, and L. Vitos, *Elasticity of high-entropy alloys from ab initio theory.* Journal of Materials Research, 2018. **33**(19): p. 2938-2953.

101. Wei, S., et al., *Electronic properties of random alloys: Special quasirandom structures.* Phys Rev B Condens Matter, 1990. **42**(15): p. 9622-9649.

102. Plimpton, S., *Fast Parallel Algorithms for Short-Range Molecular-Dynamics.* Journal of Computational Physics, 1995. **117**(1): p. 1-19.

103. Kresse, G. and J. Furthmüller, *Efficiency of ab-initio total energy calculations for metals and semiconductors using a plane-wave basis set.* Computational Materials Science, 1996. **6**(1): p. 15-50.

104. Bjørheim, T.S., A. Løken, and R. Haugsrud, *On the relationship between chemical expansion and hydration thermodynamics of proton conducting perovskites.* Journal of Materials Chemistry A, 2016. **4**(16): p. 5917-5924.

105. Løken, A., T.S. Bjørheim, and R. Haugsrud, *The pivotal role of the dopant choice on the thermodynamics of hydration and associations in proton conducting BaCe0.9X0.1O3−δ (X = Sc, Ga, Y, In, Gd and Er).* Journal of Materials Chemistry A, 2015. **3**(46): p. 23289-23298.

106. Bévillon, É., et al., *How dopant size influences the protonic energy landscape in BaSn1−xMxO3−x/2(M = Ga, Sc, In, Y, Gd, La).* J. Mater. Chem. A, 2014. **2**(2): p. 460-471.

107. Bévillon, É. and G. Geneste, *Hydration properties of BaSn0.875M0.125O3−δ substituted by large dopants (M=In, Y, Gd, and Sm) from first principles.* Physical Review B, 2008. **77**(18).

108. Snijkers, F.M.M., et al., *Proton conductivity in perovskite type yttrium doped barium hafnate.* Scripta Materialia, 2004. **51**(12): p. 1129-1134.

109. Bork, N., et al., *Simple descriptors for proton-conducting perovskites from density functional theory.* Physical Review B, 2010. **82**(1).

110. Yamazaki, Y., et al., *Proton trapping in yttrium-doped barium zirconate.* Nat Mater, 2013. **12**(7): p. 647-51.

111. Andersson, D.A., et al., *Optimization of ionic conductivity in doped ceria.* Proceedings of the National Academy of Sciences of the United States of America, 2006. **103**(10): p. 3518-3521.

112. Gilardi, E., et al., *Effect of Dopant–Host Ionic Radii Mismatch on Acceptor-Doped Barium Zirconate Microstructure and Proton Conductivity.* The Journal of Physical Chemistry C, 2017. **121**(18): p. 9739-9747.

113. Kim, H.S., et al., *Vacancy-Induced Electronic Structure Variation of Acceptors and Correlation with Proton Conduction in Perovskite Oxides.* Angew Chem Int Ed Engl, 2016. **55**(43): p. 13499-13503.

114. Monkhorst, H.J. and J.D. Pack, *Special Points for Brillouin-Zone Integrations.* Physical Review B, 1976. **13**(12): p. 5188-5192.

115. Azpiroz, J.M., et al., *Defect migration in methylammonium lead iodide and its role in perovskite solar cell operation.* Energy & Environmental Science, 2015. **8**(7): p. 2118-2127.

116. Sunarso, J., et al., *Mixed ionic-electronic conducting (MIEC) ceramic-based membranes for oxygen separation.* Journal of Membrane Science, 2008. **320**(1): p. 13-41.

117. Kreuer, K.D., *Proton-Conducting Oxides.* Annual Review of Materials Research, 2003. **33**(1): p. 333-359.

118. Malavasi, L., C.A. Fisher, and M.S. Islam, *Oxide-ion and proton conducting electrolyte materials for clean energy applications: structural and mechanistic features.* Chemical Society Reviews, 2010. **39**(11): p. 4370-4387.

119. Callister, W.D. and D.G. Rethwisch, *Materials science and engineering*. 8 th ed. Vol. 22. 2011, USA: John Wiley & Sons. 90-148.

120. Fluri, A., et al., *Enhanced proton conductivity in Y-doped $BaZrO_3$ via strain engineering.* Advanced Science, 2017. **4**(12): p. 1700467.

121. Mburu, C.W., et al., *Influence of Yttrium Concentration on Local Structure in $BaZr_{1-x}Y_xO_{3-\delta}$ Based Proton Conductors.* Journal of Physical Chemistry C, 2017. **121**(30): p. 16174-16181.

122. Han, D. and T. Uda, *The best composition of Y-doped $BaZrO_3$ electrolyte: Selection criteria from transport properties, microstructure, and phase behavior.* Journal of Materials Chemistry A, 2018. **6**: p. 18571-18582.

123. Han, D. and T. Uda, *Correlation between phase behavior and electrical conductivity of 10 mol % Y-doped $BaZrO_3$: An anomalous dispersion effect-aided synchrotron radiation XRD study combined with TEM observation and electrochemical analysis.* ACS Applied Materials & Interfaces, 2019. **11**(4): p. 3990-4000.

124. Iguchi, F., et al., *Microstructures and grain boundary conductivity of $BaZr_{1-x}Y_xO_3$ (x = 0.05, 0.10, 0.15) ceramics.* Solid State Ionics, 2007. **178**(7): p. 691-695.

125. Islam, M.S., et al., *Doping and defect association in $AZrO_3$ (A= Ca, Ba) and $LaMO_3$ (M= Sc, Ga) perovskite-type ionic conductors.* Dalton Transactions, 2004. **1**(19): p. 3061-3066.

126. Kitamura, N., et al., *Proton distribution and dynamics in Y-and Zn-doped $BaZrO_3$.* Journal of Physical Chemistry C, 2014. **118**(33): p. 18846-18852.

127. Aruta, C., et al., *A-Site cation substitutions in strained Y-doped $BaZrO_3$ multilayer films leading to fast proton transport pathways.* The Journal of Physical Chemistry C, 2016. **120**(15): p. 8387-8391.

128. Lee, H.B., F.B. Prinz, and W. Cai, *Atomistic simulations of grain boundary segregation in nanocrystalline yttria-stabilized zirconia and gadolinia-doped ceria solid oxide electrolytes.* Acta Materialia, 2013. **61**(10): p. 3872-3887.

129. Legros, M., et al., *Observation of Giant Diffusivity Along Dislocation Cores.* Science, 2008. **319**(5870): p. 1646.

130. Sun, L., D. Marrocchelli, and B. Yildiz, *Edge dislocation slows down oxide ion diffusion in doped CeO_2 by segregation of charged defects.* Nature communications, 2015. **6**: p. 6294.

131. Marrocchelli, D., L. Sun, and B. Yildiz, *Dislocations in $SrTiO_3$: easy to reduce but not so fast for oxygen transport.* J. Am. Chem. Soc, 2015. **137**(14): p. 4735-4748.

132. Harrington, G.F., et al., *The effects of lattice strain, dislocations, and microstructure on the transport properties of YSZ films.* Physical Chemistry Chemical Physics, 2017. **19**(22): p. 14319-14336.

133. Navickas, E., et al., *Dislocations accelerate oxygen ion diffusion in $La_{0.8}Sr_{0.2}MnO_3$ epitaxial thin films.* ACS Nano, 2017. **11**(11): p. 11475-11487.

134. Schie, M., et al., *Molecular dynamics simulations of oxygen vacancy diffusion in $SrTiO_3$.* Journal of Physics: Condensed Matter, 2012. **24**(48): p. 485002.

135. Islam, M.S., *Ionic transport in ABO_3 perovskite oxides: a computer modelling tour.* Journal of Materials chemistry, 2000. **10**(4): p. 1027-1038.

136. Hirel, P., et al., *The electric charge and climb of edge dislocations in perovskite oxides: The case of high-pressure $MgSiO_3$ bridgmanite.* Acta Materialia, 2016. **106**: p. 313-321.

137. Waldow, S.P. and R.A. De Souza, *Computational study of oxygen diffusion along a [100] dislocations in the perovskite oxide $SrTiO_3$.* ACS applied materials & interfaces, 2016. **8**(19): p. 12246-12256.

138. Li, X., Z. Tang, and L. Zhang, *Molecular dynamics simulations of point/line defect structures and oxygen diffusion mechanism in yttrium-doped barium zirconate.* Sci. Sin. Chim., 2019. **60**(1-10).

139. Senftle, T.P., et al., *The ReaxFF reactive force-field: development, applications and future directions.* npj Computational Materials, 2016. **2**: p. 15011.

140. Nosé, S., *A unified formulation of the constant temperature molecular dynamics methods.* The Journal of Chemical Physics, 1984. **81**(1): p. 511-519.

141. Hoover, W.G., *Canonical dynamics: Equilibrium phase-space distributions.* Physical Review A, 1985. **31**(3): p. 1695-1697.

142. Verlet, L., *Computer "experiments" on classical fluids. I. Thermodynamical properties of Lennard-Jones molecules.* Physical Review, 1967. **159**(1): p. 98-103.

143. van Duin, A.C., et al., *ReaxFF reactive force field for the Y-doped $BaZrO_3$ proton conductor with applications to diffusion rates for multigranular systems.* The Journal of Physical Chemistry A, 2008. **112**(45): p. 11414-11422.

144. Stokes, S.J. and M.S. Islam, *Defect chemistry and proton-dopant association in BaZrO 3 and BaPrO 3.* Journal of Materials Chemistry, 2010. **20**(30): p. 6258-6264.

145. Hinatsu, Y., *Electron paramagnetic resonance spectra of Pr^{4+} in $BaCeO_3$, $BaZrO_3$, $BaSnO_3$, and their solid solutions.* Journal of Solid State Chemistry, 1996. **122**(2): p. 384-389.

146. Han, D., N. Hatada, and T. Uda, *Chemical expansion of yttrium-doped barium zirconate and correlation with proton concentration and conductivity.* Journal of the American Ceramic Society, 2016. **99**(11): p. 3745-3753.

147. Yamanaka, S., et al., *Thermophysical properties of $BaZrO_3$ and $BaCeO_3$.* Journal of Alloys and Compounds, 2003. **359**(1-2): p. 109-113.

148. Jia, C., A. Thust, and K. Urban, *Atomic-scale analysis of the oxygen configuration at a $SrTiO_3$ dislocation core.* Physical review letters, 2005. **95**(22): p. 225506.

149. Hirel, P., *Atomsk: a tool for manipulating and converting atomic data files.* Computer Physics Communications, 2015. **197**: p. 212-219.

150. Guo, J., A. Haji-Akbari, and J.C. Palmer, *Hybrid Monte Carlo with LAMMPS.* Journal of Theoretical and Computational Chemistry, 2018. **17**(03): p. 1840002.

151. Fabbri, E., et al., *Does the increase in Y-dopant concentration improve the proton conductivity of $BaZr_{1-x}Y_xO_{3-\delta}$ fuel cell electrolytes?* Solid State Ionics, 2010. **181**(21-22): p. 1043-1051.

152. Chintapalli, M., et al., *Relationship between conductivity, ion diffusion, and transference number in perfluoropolyether electrolytes.* Macromolecules, 2016. **49**(9): p. 3508-3515.

153. Han, D. and T. Uda, *The best composition of an Y-doped $BaZrO_3$ electrolyte: selection criteria from transport properties, microstructure, and phase behavior.* Journal of Materials Chemistry A, 2018. **6**(38): p. 18571-18582.

154. Patnaik, A.S. and A.V. Virkar, *Transport properties of potassium-doped $BaZrO_3$ in oxygen and water vapor containing atmospheres.* Journal of The Electrochemical Society, 2006. **153**(7): p. A1397-A1405.

155. Yamazaki, Y., et al., *Proton trapping in yttrium-doped barium zirconate.* Nature Materials, 2013. **12**: p. 647-651.

156. Akbarzadeh, A.R., et al., *Combined theoretical and experimental study of the low-temperature properties ofBaZrO3.* Physical Review B, 2005. **72**(20).

157. Tolchard, J.R. and T. Grande, *Chemical compatibility of candidate oxide cathodes for BaZrO3 electrolytes.* Solid State Ionics, 2007. **178**(7-10): p. 593-599.

158. Adler, S.B., *Chemical expansivity of electrochemical ceramics.* Journal of the American Ceramic Society, 2001. **84**(9): p. 2117-2119.

159. Jia, C.L., A. Thust, and K. Urban, *Atomic-scale analysis of the oxygen configuration at a SrTiO3 dislocation core.* Physical Review Letters, 2005. **95**(22).

160. Jain, A., et al., *Commentary: The Materials Project: A materials genome approach to accelerating materials innovation.* Apl Materials, 2013. **1**(1).

161. Inaba, H. and H. Tagawa, *Ceria-based solid electrolytes.* Solid state ionics, 1996. **83**(1-2): p. 1-16.

162. Vayssilov, G.N., et al., *Support nanostructure boosts oxygen transfer to catalytically active platinum nanoparticles.* Nature materials, 2011. **10**(4): p. 310.

163. Fu, Q., H. Saltsburg, and M. Flytzani-Stephanopoulos, *Active nonmetallic Au and Pt species on ceria-based water-gas shift catalysts.* Science, 2003. **301**(5635): p. 935-938.

164. Trovarelli, A., *Catalytic properties of ceria and CeO2-containing materials.* Catalysis Reviews, 1996. **38**(4): p. 439-520.

165. Montini, T., et al., *Fundamentals and catalytic applications of CeO2-based materials.* Chemical reviews, 2016. **116**(10): p. 5987-6041.

166. Skorodumova, N., et al., *Quantum origin of the oxygen storage capability of ceria.* Physical Review Letters, 2002. **89**(16): p. 166601.

167. Shoko, E., M. Smith, and R.H. McKenzie, *Charge distribution near bulk oxygen vacancies in cerium oxides.* Journal of Physics: Condensed Matter, 2010. **22**(22): p. 223201.

168. Ganduglia-Pirovano, M.V., A. Hofmann, and J. Sauer, *Oxygen vacancies in transition metal and rare earth oxides: Current state of understanding and remaining challenges.* Surface science reports, 2007. **62**(6): p. 219-270.

169. Paier, J., C. Penschke, and J. Sauer, *Oxygen defects and surface chemistry of ceria: quantum chemical studies compared to experiment.* Chemical reviews, 2013. **113**(6): p. 3949-3985.

170. Li, H.-Y., et al., *Multiple configurations of the two excess 4 f electrons on defective CeO 2 (111): Origin and implications.* Physical Review B, 2009. **79**(19): p. 193401.

171. Jerratsch, J.-F., et al., *Electron localization in defective ceria films: a study with scanning-tunneling microscopy and density-functional theory.* Physical review letters, 2011. **106**(24): p. 246801.

172. Murgida, G.E. and M.V. Ganduglia-Pirovano, *Evidence for subsurface ordering of oxygen vacancies on the reduced CeO 2 (111) surface using density-functional and statistical calculations.* Physical review letters, 2013. **110**(24): p. 246101.

173. Sutton, J.E., A. Beste, and S.H. Overbury, *Origins and implications of the ordering of oxygen vacancies and localized electrons on partially reduced CeO 2 (111).* Physical Review B, 2015. **92**(14): p. 144105.

174. Torbrügge, S., et al., *Evidence of subsurface oxygen vacancy ordering on reduced CeO 2 (111).* Physical review letters, 2007. **99**(5): p. 056101.

175. Esch, F., et al., *Electron localization determines defect formation on ceria substrates.* Science, 2005. **309**(5735): p. 752-755.

176. Castleton, C., J. Kullgren, and K. Hermansson, *Tuning LDA+ U for electron localization and structure at oxygen vacancies in ceria.* Journal of Chemical Physics, 2007. **127**(24): p. 244704-244704.

177. Kullgren, J., et al., *Oxygen Vacancies versus Fluorine at CeO 2 (111): A Case of Mistaken Identity?* Physical review letters, 2014. **112**(15): p. 156102.

178. Namai, Y., K.-i. Fukui, and Y. Iwasawa, *Atom-resolved noncontact atomic force microscopic observations of CeO2 (111) surfaces with different oxidation states: Surface structure and behavior of surface oxygen atoms.* The Journal of Physical Chemistry B, 2003. **107**(42): p. 11666-11673.

179. Conesa, J.C., *Surface anion vacancies on ceria: Quantum modelling of mutual interactions and oxygen adsorption.* Catalysis Today, 2009. **143**(3): p. 315-325.

180. Han, Z.-K., et al., *Unraveling the oxygen vacancy structures at the reduced Ce O 2 (111) surface.* Physical Review Materials, 2018. **2**(3): p. 035802.

181. Kullgren, J., et al., *DFT-Based Monte Carlo Simulations of Impurity Clustering at CeO2 (111).* The Journal of Physical Chemistry C, 2017.

182. Murgida, G.E., et al., *Ordering of oxygen vacancies and excess charge localization in bulk ceria: A DFT+ U study.* Physical Review B, 2014. **90**(11): p. 115120.

183. Wang, B., X. Xi, and A.N. Cormack, *Chemical Strain and Point Defect Configurations in Reduced Ceria.* Chemistry of Materials, 2014. **26**(12): p. 3687-3692.

184. Han, X., et al., *Reply to "Comment on 'Oxygen Vacancy Ordering and Electron Localization in CeO2: Hybrid Functional Study'".* The Journal of Physical Chemistry C, 2017. **121**(38): p. 21084-21086.

185. Allen, J.P. and G.W. Watson, *Occupation matrix control of d-and f-electron localisations using DFT+ U.* Physical Chemistry Chemical Physics, 2014. **16**(39): p. 21016-21031.

186. Kullgren, J., K. Hermansson, and C. Castleton, *Many competing ceria (110) oxygen vacancy structures: From small to large supercells.* The Journal of chemical physics, 2012. **137**(4): p. 044705.

187. Grieshammer, S., M. Nakayama, and M. Martin, *Association of defects in doped non-stoichiometric ceria from first principles.* Physical Chemistry Chemical Physics, 2016. **18**(5): p. 3804-3811.

188. Arapan, S., S.I. Simak, and N.V. Skorodumova, *Volume-dependent electron localization in ceria.* Physical Review B, 2015. **91**(12): p. 125108.

189. Rossignol, S., et al., *Structural changes of Ce–Pr–O oxides in hydrogen: a study by in situ X-ray diffraction and Raman spectroscopy.* Journal of Materials Chemistry, 2003. **13**(12): p. 3017-3020.

190. Wang, B. and A.N. Cormack, *Strain modulation of defect structure in gadolinia-doped ceria.* The Journal of Physical Chemistry C, 2012. **117**(1): p. 146-151.

191. Andersson, D.A., et al., *Optimization of ionic conductivity in doped ceria.* Proceedings of the National Academy of Sciences, 2006. **103**(10): p. 3518-3521.

192. Artini, C., et al., *High Temperature Structural Study of Gd-Doped Ceria by Synchrotron X-ray Diffraction (673 K⩽T⩽1073 K).* Inorganic chemistry, 2014. **53**(19): p. 10140-10149.

193. Žguns, P.A., A.V. Ruban, and N.V. Skorodumova, *Influence of composition and oxygen-vacancy ordering on lattice parameter and elastic moduli of Ce1-xGdxO2-x/2: A theoretical study.* Scripta Materialia, 2019. **158**: p. 126-130.

194. Hinterberg, J., T. Zacherle, and R. De Souza, *Activation volume tensor for oxygen-vacancy migration in strained CeO 2 electrolytes.* Physical review letters, 2013. **110**(20): p. 205901.

195. De Souza, R.A., A. Ramadan, and S. Hörner, *Modifying the barriers for oxygen-vacancy migration in fluorite-structured CeO 2 electrolytes through strain: a computer simulation study.* Energy & Environmental Science, 2012. **5**(1): p. 5445-5453.

196. Luches, P., F. Pagliuca, and S. Valeri, *Structural and morphological modifications of thermally reduced cerium oxide ultrathin epitaxial films on Pt (111).* Physical Chemistry Chemical Physics, 2014. **16**(35): p. 18848-18857.

197. Duchoň, T.s., et al., *Ordered phases of reduced ceria as epitaxial films on Cu (111).* The Journal of Physical Chemistry C, 2013. **118**(1): p. 357-365.

198. Olbrich, R., et al., *Surface stabilizes ceria in unexpected stoichiometry.* The Journal of Physical Chemistry C, 2017. **121**(12): p. 6844-6851.

199. Perdew, J.P., K. Burke, and M. Ernzerhof, *Generalized gradient approximation made simple.* Physical review letters, 1996. **77**(18): p. 3865.

200. Castleton, C., J. Kullgren, and K. Hermansson, *Tuning LDA+ U for electron localization and structure at oxygen vacancies in ceria.* The Journal of chemical physics, 2007. **127**(24): p. 244704.

201. Kresse, G. and D. Joubert, *From ultrasoft pseudopotentials to the projector augmented-wave method.* Physical Review B, 1999. **59**(3): p. 1758.

202. Duclos, S.J., et al., *High-pressure x-ray diffraction study of CeO 2 to 70 GPa and pressure-induced phase transformation from the fluorite structure.* Physical Review B, 1988. **38**(11): p. 7755.

203. Keating, P., D. Scanlon, and G. Watson, *Intrinsic ferromagnetism in CeO2: dispelling the myth of vacancy site localization mediated superexchange.* Journal of Physics: Condensed Matter, 2009. **21**(40): p. 405502.

204. Da Silva, J.L.F., et al., *Hybrid functionals applied to rare-earth oxides: The example of ceria.* Physical Review B, 2007. **75**(4).

205. Pfau, A. and K.D. Schierbaum, *The Electronic-Structure of Stoichiometric and Reduced Ceo2 Surfaces - an Xps, Ups and Hreels Study.* Surface Science, 1994. **321**(1-2): p. 71-80.

VITA

Lei Zhang was born in Hubei, China, in 1988. He received his B.S. and M.S. in Materials Science and Engineering from Shanghai Jiao Tong University and Penn State University (Advisor: Prof. Zi-Kui Liu) in 2010 and 2013. After getting trained on CALPHAD modeling and *ab-initio* thermodynamics framework, by working on the thermodynamic database construction of $(La, Sr)CoO_{3-\delta}$ sponsored by Air Products and Chemicals, Inc. He then joined Prof. Meilin Liu's SOFCs group here at Georgia Tech for Ph.D. degree. Bringing the computational expertise from previous training, Lei absorbed and developed customized computational models for Liu group, to help theoretically understand mechanism on surface electro-catalysis, catalysis, defect chemistry, ionic transport, and so on, using electronic structure methods such as DFT, coupled with a combination of statistical mechanics methods, including phonon vibrational partition function, cluster expansion, molecular dynamics (classical and *ab-initio*). Lei contributed to multiple projects including Samsung, SECA, ARPA-E, and Phillip66. During his Ph.D. program, Lei authored/co-authored ~30 journal papers, 2 US patents and presented research 3 times in ECS and APS conferences. Lei also actively joined summer school and workshop on computational techniques and frameworks held in UFL, Temple U, Georgia Tech, UIUC, and UMich. He also participated in a summer research internship at ORNL in 2019. Besides, Lei is an experienced CALPHAD modeler and has an interest in electrochemical modeling as well.